Title
Design and Deployment of the POLARBEAR Cosmic Microwave Background Polarization Experiment

Author
Arnold, Kam Stahly

Publication Date
2010

Peer reviewed|Thesis/dissertation

Design and Deployment of the POLARBEAR Cosmic Microwave Background Polarization Experiment

by

Kam Stahly Arnold

A dissertation submitted in partial satisfaction of the

requirements for the degree of

Doctor of Philosophy

in

Physics

in the

Graduate Division

of the

University of California, Berkeley

Committee in charge:

Professor Adrian T. Lee, Chair

Professor William L. Holzapfel

Professor William J. Welch

Fall 2010

Design and Deployment of the POLARBEAR Cosmic Microwave Background Polarization Experiment

Kam Stahly Arnold

Abstract

Design and Deployment of the POLARBEAR Cosmic Microwave Background Polarization Experiment

by

Kam Stahly Arnold

Doctor of Philosophy in Physics

University of California, Berkeley

Professor Adrian T. Lee, Chair

POLARBEAR is a Cosmic Microwave Background (CMB) polarization experiment that will measure the CMB polarization angular power spectrum with unprecedented precision, searching for evidence of inflationary gravitational waves and the gravitational lensing of the CMB polarization by large scale structure. This dissertation presents an overview of the design of the instrument, focusing on the design and fabrication of the focal plane, and presents the results of some tests of instrument performance, both in the laboratory and from the initial engineering deployment.

The structure of this thesis is as follows: Chapter 1 introduces the theoretical constructs used to describe the CMB polarization anisotropies, and the state of measurements in the field. Chapter 2 gives an overview of the choices made in the instrument design. Chapter 3 discusses the fundamental limits to the sensitivity of bolometric detectors, and chapter 4 explains the design choices involved in populating the focal plane with detectors. Chapter 5 describes the details of the detector architecture and fabrication, and chapter 6 the details of selecting the spectral band of the detectors. Finally, chapter 7 goes through some results obtained before and during the POLARBEAR engineering run in 2010, and comments on the work to be done before the Chilean deployment.

To my parents, Doug and Barb,
who kept me out of school until grade ten, only to watch me enroll for the next fourteen years.

And to my wife, Aurrora,
from whom I still have so much to learn.

Contents

List of Figures

List of Tables

Acknowledgments

The POLARBEAR experiment is building upon the amazing past work in CMB science, and harnessing the effort of many people across several institutions. Some acknowledgments are in order for the contributions others have made to the work described in this dissertation.

The introductory chapter closely follows some of the explanations given in Dodelson's 2003 book [1], to which I owe much of my understanding of cosmology. The POLARBEAR instrument's optical system and cryogenic receiver, which are described in chapter 2, could not have been designed or built without Huan Tran and Zigmund Kermish, who were respectively responsible for these parts of the experiment. The pixel design owes much to Mike Myers, who pioneered this general pixel architecture for CMB applications at UC Berkeley, and to Xiaofan Meng, whose experience in Niobium-based devices has been very important. For the thousands of hours I've spend fabricating detectors, both frustrating and rewarding, I have to acknowledge the UC Berkeley Microlab. Not only does it provide the infrastructure for this type of detector research and development, but also a community that has so much to teach about microfabrication. The data shown in chapter 7 from the deployment to Cedar Flat are the result of a huge effort by many people in the POLARBEAR collaboration, including Aubra Anthony, Dave Boettger, Josquin Errard, Daniel Flanigan, Nils Halverson, Jacob Howard, Peter Hyland, Marius Lungu, Nathan Miller, Haruki Nishino, Erin Quealy, Ian Schanning and Bryan Steinbach.

I will also take this opportunity to acknowledge Adrian Lee, Bill Holzapfel, and Paul Richards, for leading a world-class CMB research group in which the opportunities for graduate students are limitless.

Finally, some financial acknowledgments are in order. The POLARBEAR project is funded by the National Science Foundation under grant AST-0618398. Antenna-coupled bolometer development at Berkeley is also funded by NASA under grant NNG06GJ08G. Before my funding through the POLARBEAR project, I was funded in part by a National Defense Science and Engineering Graduate Fellowship.

Chapter 1

Polarization of the Cosmic Microwave Background

Figure 1.1 shows a timeline of the history of the universe. Along the horizontal axis, two variables representing the evolution of the universe are shown: at the bottom is time, t, and at the top is the average temperature of the radiation throughout the universe, T. These variables have a one-to-one relationship, because throughout the known history of the universe it has been expanding and cooling. Our world exists at the right-hand end of figure 1.1, where $T = 2.725$ Kelvin [2], and the last $t \sim 14$ billion years of the universe can be understood in the broadest terms using the physics known today.

All around the Earth we observe examples of complicated luminous structures: our sun, galaxy, cluster of galaxies, and so on. Looking back in time (to the left on figure 1.1), all of the stars and galaxies around us formed during the period of luminous structure formation, since the time referred to as reionization [3]. Before that was a period called the cosmic dark ages, where gravitational clumping of matter was leading to overdense and underdense regions, but where no region had yet become so dense as to initiate nuclear fusion and form a star. There is no light-emitting structure for us to observe from these cosmic dark ages, but we can observe photons that were simply free-streaming through that transparent universe from what came before it, the surface of last scattering.

The surface of last scattering occurred when the then much hotter universe had cooled to the point that electrons and protons could combine to form hydrogen. At that time, the photons, which had been strongly interacting with the free electrons through Thomson scattering, no longer had free electrons to interact with, and their mean free path quickly became larger than the Hubble radius. The Hubble radius is an important length to define in an expanding universe: it is the distance between two points such that they are expanding away from each other faster than the speed of light, and so cannot be causally connected. If the mean free path of the photon is larger than the Hubble radius, that means that most photons simply free-stream and

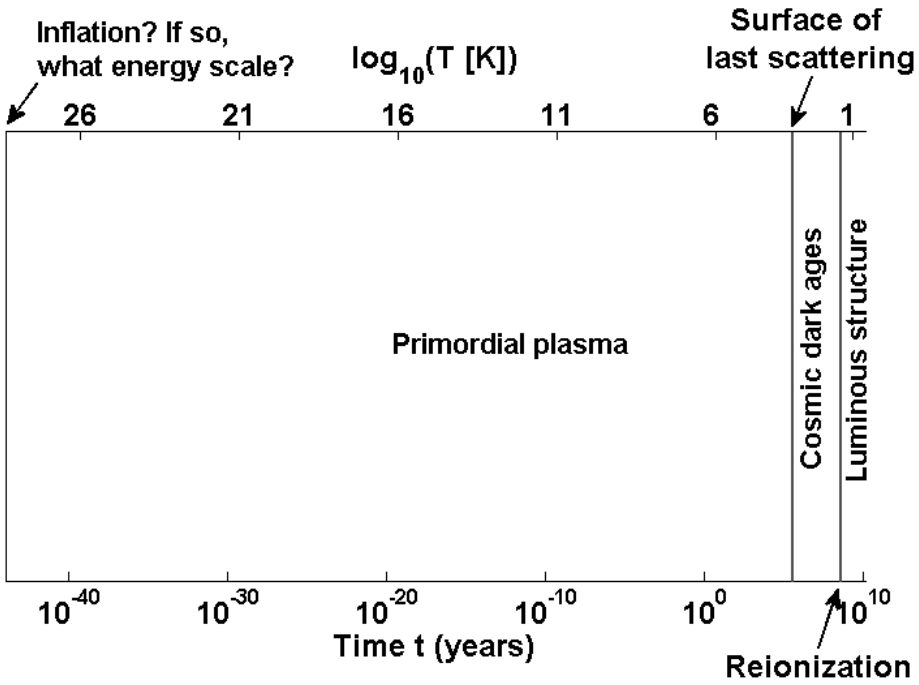

Figure 1.1: A timeline of the history of the universe, from inflation to today. Some times of importance are noted, both in time t (on the bottom axis), and temperature T of the radiation in the universe at that time (on the top axis).

do not scatter as they travel through the universe. We can measure those photons coming from the surface of last scattering all around us and map out their temperature as a function of position on the sky. Figure 1.2 shows the Wilkinson Microwave Anisotropy Probe (WMAP) measurement of the anisotropies in this temperature across the entire sky.

1.1 Temperature of the CMB

It is useful to think about Figure 1.2 in two ways. One is as a map of the photon temperature anisotropy function, $\Theta(\vec{x_0}, \hat{p}, t_0)$, at time and position now (t_0) and here (x_0), as a function of the photon direction ($\hat{p}$). It is also useful to think about this map as looking back in time: the photons have been free-streaming since the surface of last scattering, and so by looking in different directions we are effectively looking at different positions in the universe at the time of last scattering.

The first important thing to point out about Figure 1.2 is not the anisotropy, but the relative isotropy. This color scale represents ± 200 μK, while the mean temperature is 2.725 K; the entire sky appears to be the same temperature with a precision

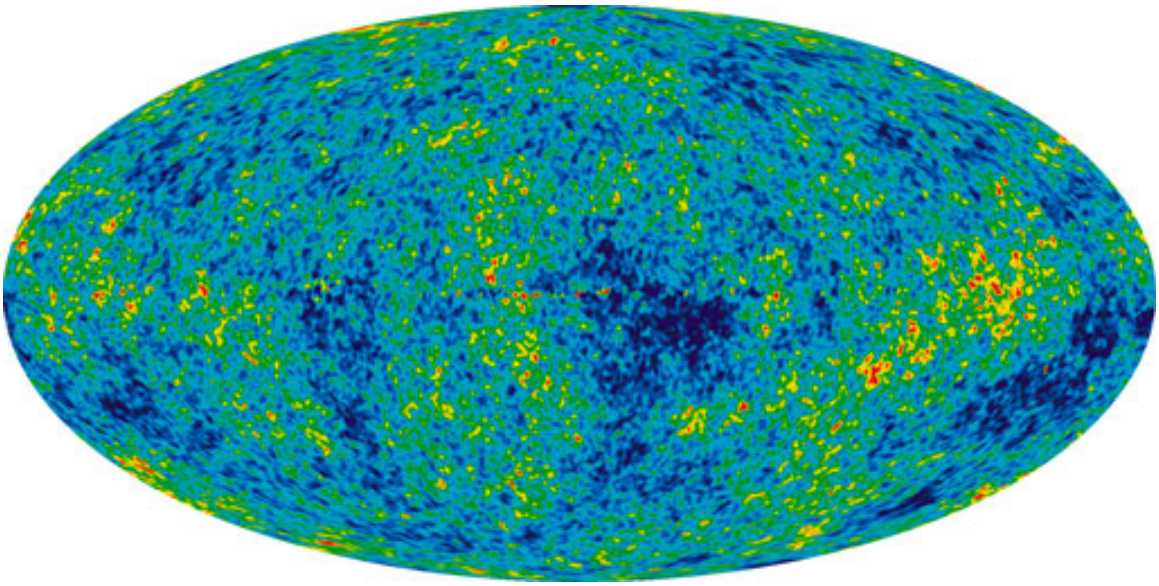

Figure 1.2: The Wilkinson Microwave Anisotropy Probe (WMAP) full-sky map of the anisotropies in the Cosmic Microwave Background (CMB) (NASA / WMAP Science Team). The color scale represents ± 200 μK from the mean 2.725 K. The contribution from the dipole anisotropy and the galaxy has been removed.

of one part in 10^4. Actually, this is very strange. Two points that appear 10 degrees away from each other in figure 1.2 are in positions on the surface of last scattering that are further away from each other than the Hubble radius at that time. If those points are further apart than the Hubble radius—out of causal interaction—how can they have equilibrated?

This seeming paradox is resolved by invoking a period of inflation in the early universe, marked on the far left side of the timeline in figure 1.1. This proposed inflationary period consists of an accelerating expansion of the universe (in most models it is approximately exponential) which takes nearby points that have equilibrated and quickly expands them far outside the Hubble radius [4], so that points well outside the Hubble radius have approximately the same temperature. Only approximately, because quantum fluctuations during inflation imprint perturbations on the gravitational metric. These perturbations are also expanded out beyond the Hubble radius during inflation, so that after the inflationary period ends, they exist across all size scales of interest. For the perturbations with size scale larger than the Hubble radius, their amplitude stays approximately constant because they cannot causally evolve. After inflation, the universe is still expanding, but more slowly than the speed of light, so the Hubble radius is growing with time. Significant changes to the primordial perturbations do not occur until the Hubble radius "catches up" with them well after inflation, and causal interaction can begin to occur. These evolving metric per-

turbations couple to the photon temperature, and are the key to understanding the anisotropies in figure 1.2.

1.2 Angular power spectrum of the CMB temperature anisotropies

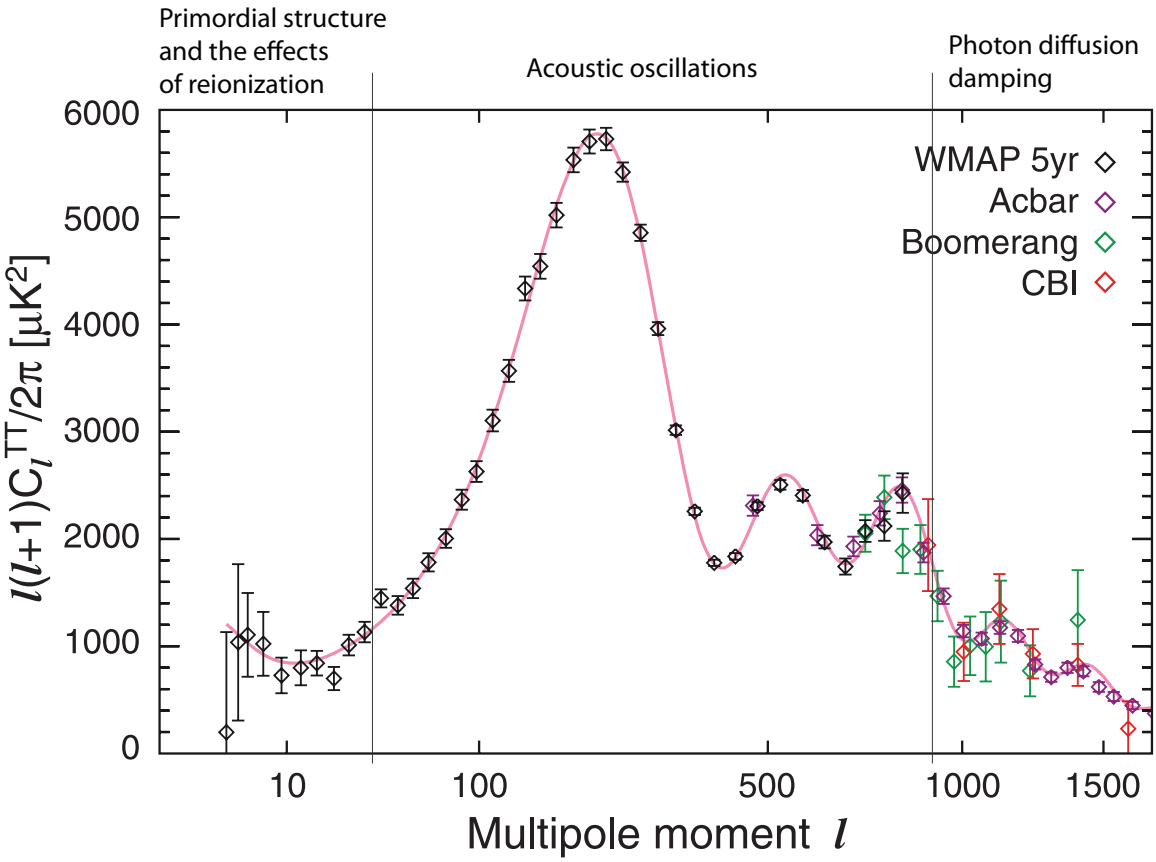

Figure 1.3: A compilation of the measurements made by several experiments of the angular power spectrum C_ℓ of the temperature anisotropies in the CMB, along with a best-fit standard cosmological model. The data were compiled and fit in [5] by the NASA / WMAP Science Team. The labels and demarcations of angular scale were added for this dissertation.

With different size scales of primordial perturbation beginning to causally evolve at different times, it is useful to look at the anisotropies $\Theta(\vec{x_0}, \hat{p}, t_0)$ in figure 1.2 in terms of their angular power spectrum, shown in figure 1.3. The vertical axis of figure 1.3 is proportional to C_ℓ, which for each ℓ is the variance of the coefficients of the spherical harmonic expansion of $\Theta(\vec{x_0}, \hat{p}, t_0)$. The coefficients $a_{\ell m}$ are defined by

$$\Theta(\vec{x_0}, \hat{p}, t_0) = \sum_{\ell=1}^{\infty} \sum_{m=-\ell}^{\ell} a_{\ell m} Y_{\ell m}(\hat{p}), \tag{1.1}$$

where $Y_{\ell m}(\hat{p})$ are the angular spherical harmonics.

In this angular Fourier space, smaller ℓ corresponds to larger angular scale, or greater distance apart at the time of last scattering. $\ell \lesssim 30$ represent scales that were still larger than the Hubble radius at the surface of last scattering, so here the anisotropies have not significantly changed from the primordial power spectrum set up by inflation. Smaller scales in figure 1.3 exhibit interesting structure. Here, photon temperature has evolved by being strongly coupled to electrons through Thomson scattering. The electrons, in turn, are strongly coupled to protons by the Coulomb interaction, so the entire photon-electron-proton system acts as a single compressible fluid. This fluid exists in a background of gravitational potential wells of all size scales, established by the effect of the gravitational metric perturbations on the underlying dark matter distribution. The photon-baryon fluid undergoes a series of oscillations driven by these gravitational potential wells and the pressure created by the relativistic photon collisions. This fluid has a uniform sound speed, so the period of an oscillation is proportional to its size scale. A peak in the power spectrum corresponds to a size scale on which the inhomogeneity oscillation was at a peak at the time of last scattering. Troughs in the power spectrum, which represent angular scales on which there is less anisotropy, correspond to scales for which the inhomogeneity oscillation was near equilibrium at the time of decoupling. These inhomogeneity oscillations are referred to as acoustic oscillations. The acoustic peaks and valleys in the angular power spectrum would continue out to smaller and smaller scales, but the anisotropies are damped on scales smaller than the mean free path of the photon, and the thickness (duration), of the "surface" of last scattering.

Many instruments have observed temperature—photon intensity—fluctuations consistent with this acoustic oscillation model of the early universe. Another property of the CMB photons is their polarization; the next section will discuss the polarization anisotropies in the CMB.

1.3 Polarization anisotropy power spectrum

Understanding the polarization anisotropy power spectrum requires a more detailed discussion of the metric perturbations underlying the photon anisotropies. There are two types of metric perturbations that will be important here, scalar and tensor. Scalar perturbations of the metric couple to matter density and photon temperature, and are responsible for the acoustic oscillations described above. Tensor perturbations do not couple to matter density, but as discussed below, do couple to the CMB polarization.

1.3.1 Scalar and tensor metric perturbations

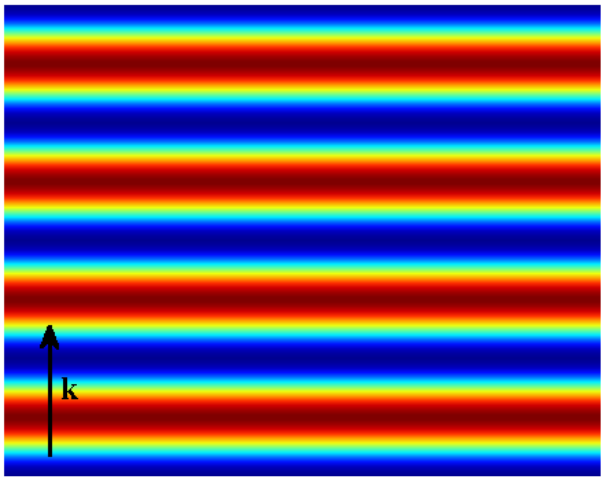

Figure 1.4: An illustration of a single Fourier mode of scalar perturbation, with the wave vector $\hat{k}$ always parallel to the gradient of the metric perturbation. This is a longitudinal wave, and it couples to matter and photons to cause the acoustic oscillations described in section 1.2.

Figure 1.4 shows a two-dimensional cut through a single Fourier mode of a scalar perturbation, with the shading representing regions of higher density and temperature. Consider the photon temperature anisotropy function $\Theta(\vec{x}, \hat{p}, t)$, for position $\vec{x}$ and time t in one of the regions of this single longitudinal Fourier mode where the temperature is maximum. Photons coming from directions perpendicular to the wave vector will have the same temperature, but photons coming from directions parallel to the wave vector will have lower temperature. For any point $\vec{x}$, the photon temperature anisotropy function at that point, $\Theta(\vec{k}, \hat{p}, t)$, depends not separately on $\hat{p}$ and $\vec{k}$, but rather on $\hat{p} \cdot \vec{k}$. The same is not true for the photon temperature anisotropy function associated with tensor perturbations. Tensor perturbations can produce photon temperature gradients in any direction in the plane perpendicular to the wave vector, so that the photon temperature anisotropy function depends on both $\vec{k}$ and $\hat{p}$.

In both cases, the anisotropy function Θ is small, so it is reasonable to expand it in terms of its multipole components and only retain the leading terms. For the discussion that follows, only the monopole, dipole, and quadrupole anisotropy are important. The quadrupole term must be included, because it has an effect on polarization through Thomson scattering, as is described in the next section.

1.3.2 Polarization induced by Thomson scattering

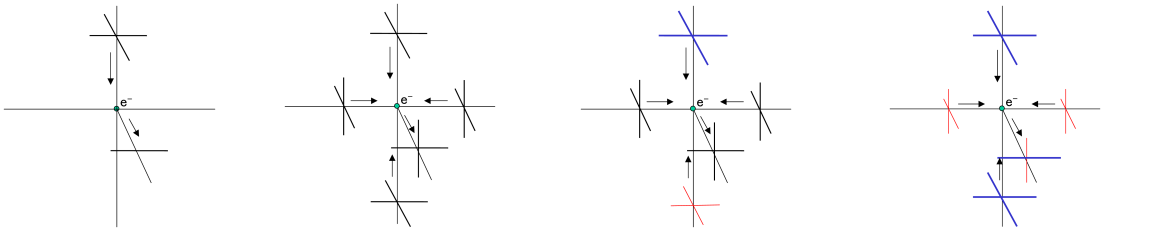

Single photon **(a)** | Monopole anisotropy **(b)** | Dipole anisotropy **(c)** | Quadrupole anisotropy **(d)**

Figure 1.5: An illustration of the Thomson scattering of photons (shown here as crosses with line length proportional to temperature and directed along the photons' polarization) off an electron, with **(a)** only a single photon scattering at 90 degrees, **(b)** a monopole, **(c)** a dipole, and **(d)** a quadrupole photon temperature anisotropy Θ.

Figure 1.5 schematically shows the scattering of photons off electrons for four cases. When a photon scatters off an electron at 90 degrees, the polarization of the scattered photon is perpendicular to the direction from which the photon came. This would appear to make Thomson scattering an efficient polarizer, but for the monopole distribution illustrated in figure 1.5**(b)**, since photons from all directions have the same temperature, there is no average scattered polarization.

There is also no average polarization from the dipole moment illustrated in figure 1.5**(c)**, since the hot and cold cancel out in the scattered beam. But for the quadrupole moment illustrated in figure 1.5**(d)**, the scattered beam is polarized proportional to the quadrupole moment.

1.3.3 Symmetry properties of the quadrupole photon anisotropy

For a scalar perturbation, as described in section 1.3.1, the induced quadrupole is rotationally symmetric about the wavevector direction $\hat{k}$. This means that the polarization direction is either aligned with or perpendicular to the projected wavevector direction on the sky. Since the magnitude of the quadrupole (and thus the magnitude of the polarization) varies only along that wavevector, the magnitude of the polarization varies only along the axis perpendicular or parallel to the polarization. This is the hallmark of an *E-mode*, so-called because it is the spin-2 analog of what is true about the electric field in free space—its magnitude varies only parallel to its direction.

Section 1.3.1 contrasts scalar perturbations to tensor perturbations: tensor perturbations create photon temperature anisotropy that varies azimuthally about $\hat{k}$. This

creates a local quadrupole anisotropy that is aligned with some azimuthal direction $\hat{\phi}$, which that takes on all directions over the spectrum of tensor perturbations. The induced polarization therefore also takes on all directions over the spectrum of $\vec{k}$. The magnitude of the polarization still varies as a function of the projected wavevector on the sky, but the direction of the polarization is not strictly aligned with or perpendicular to $\hat{k}$. This means that it contributes to both *E-modes* (as described above), and *B-modes*, the component of the polarization field with magnitude varying in a direction 45 degrees from the direction of the polarization. The term *B-modes* comes from the analogy to the spin-1 magnetic field in free space, where the magnitude of the field varies perpendicular to the direction of the field.

1.3.4 Predicted polarization power spectra

Figure 1.6 is a theoretical anisotropy power spectrum, just like figure 1.3, but showing polarization anisotropies. Note the vertical axis scale is different in the two figures; the relatively faint polarization signal has anisotropies with power well below that of the temperature signal. In figure 1.6, the anisotropy power has been separated into E-modes and B-modes.

The E-mode spectrum exhibits similar features to the temperature spectrum, since they are both sourced primarily by scalar perturbations. Polarization power is suppressed on large scales because photon diffusion suppresses the local quadrupole anisotropy on large scales during decoupling. The increase in polarization anisotropy power at the very largest scales ($\ell \lesssim 10$) is due to the much later reionization of the universe after which a small fraction of photons scatter off electrons that exist in a universe with a quadrupole photon anisotropy [9].

B-modes predicted by inflation

Tensor perturbations create B-mode polarization depending on the energy scale of inflation. This energy scale is characterized by the tensor-to-scalar ratio r. Figure 1.6 shows the expected B-mode signal from tensor perturbations for $r = 0.1$ and $r = 0.025$. These are suppressed at small scales because gravitational waves decay once they are smaller than the Hubble radius, so only modes larger than or about the size of the Hubble radius at decoupling (a few degrees) contribute. Measuring this signal would help characterize inflation, and shed light on energy scales much higher than those in our local universe. Several experiments are currently underway to try to achieve this exciting goal [10, 11, 12, 13, 14].

B-modes due to gravitational lensing

Another source of B-mode polarization signal is included on this plot. It is not from tensor waves, but from gravitational lensing of the CMB by structure between

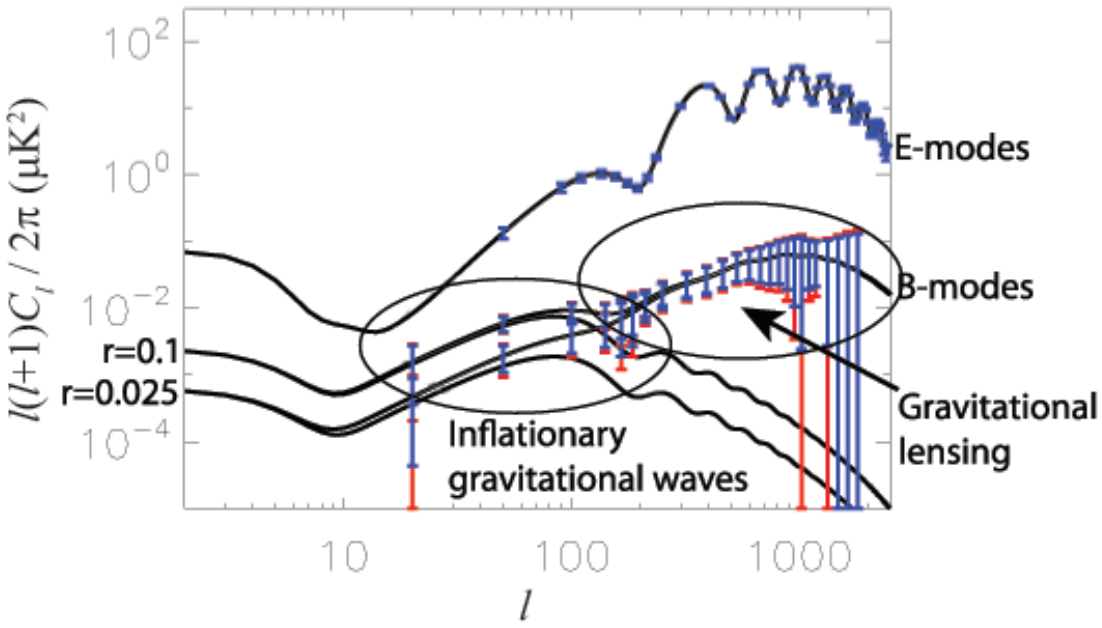

Figure 1.6: The solid lines show predicted polarization power spectra. The E-modes, at the top, are constrained by the same physics as the temperature anisotropies shown in figure 1.3. The B-modes are sourced by gravitational lensing of the E-modes (smaller scales), and by the tensor metric perturbations predicted by inflation, shown for $r = 0.1$ and $r = 0.025$. The error bars show the expected sensitivity of POLARBEAR to the CMB polarization anisotropies as a function of angular scale, with and without galactic foregrounds, the smaller for the case where there are no foregrounds and the larger assuming subtraction of nominal foregrounds. The total observation time assumed is 8 hours per day and 9 months per year for one year at 150 GHz and six months at 220 GHz. Foreground signals (not shown) are modeled using [6, 7, 8]. The error bars here were calculated by Nathan Miller, a POLARBEAR collaborator at the University of California, San Diego. The legend items were added for this dissertation.

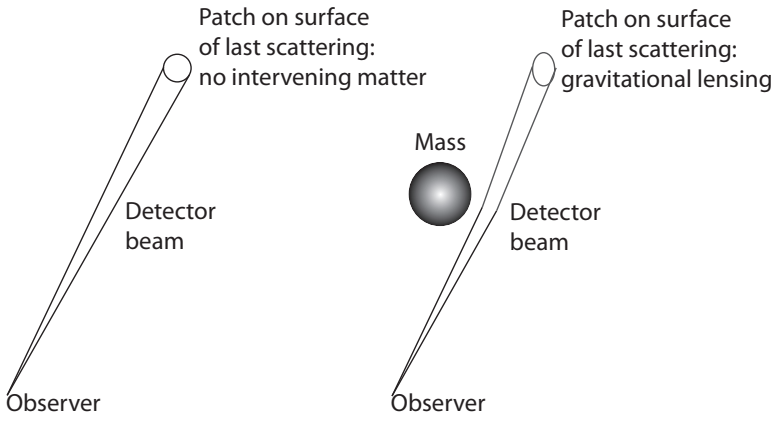

Figure 1.7: Cartoon illustrating the gravitational lensing effect of intervening matter on the observed surface of last scattering.

the surface of last scattering and us, the observer. Gravitational lensing cannot create polarization, but it can mix E-modes into B-modes. Figure 1.7 is a cartoon illustration of this effect. Imagine a circular beam coming from Earth and going out to the surface of last scattering. If the beam passes through a gradient in matter density, the beam will be distorted. This shearing would convert a purely E-mode signal to some mixture of E- and B-modes. Because of the angular scale of gravitational structure, this effect is predicted to peak at smaller angular scales than the peak in the tensor metric perturbations, as shown in figure 1.6. This lensing effect contains information about the evolution of the matter power spectrum. The CMB is the ultimate back-light for lensing, and the effect is dominated by the matter distribution at intermediate redshifts, which is very sensitive to the sum of the neutrino masses (*hot* dark matter), and to changes in the equation of state of dark energy [15].

1.4 Current state of the field

A few CMB polarization experiments have measured the E-mode polarization signal to be consistent with predictions from the acoustic oscillation model [16, 17, 18, 19]. All of these experiments have put only upper bounds on the B-mode signal. Along with precisely measuring the E-mode polarization anisotropies, the POLARBEAR experiment will have sufficient sensitivity to measure the predicted B-mode polarization signal from gravitational lensing, and to search for the B-mode polarization signal from inflation, detecting the signal if the tensor-to-scalar ratio r is greater than 0.01.

Chapter 2

POLARBEAR Instrument Overview

To characterize the B-modes in the CMB polarization, POLARBEAR must have unprecedented sensitivity on the angular scales over which the signal exists (angular wavenumber ℓ between 20 and 2000, see figure 1.6), and precise control of systematic instrumental effects. This chapter describes how the overall design of the instrument addresses these goals.

2.1 Spectral region of observation

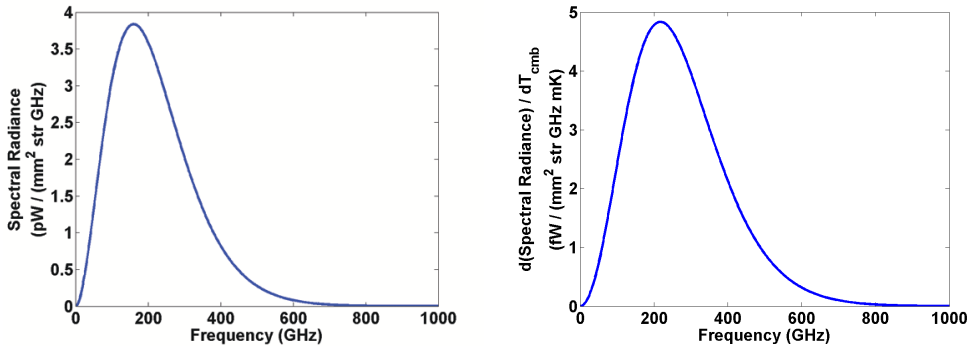

(a) (b)

Figure 2.1: **(a)** Blackbody spectral radiance for a temperature of $T_{cmb} = 2.725$ K, and **(b)** the derivative of **(a)** with respect to T_{cmb}.

The blackbody spectrum of the 2.725 K CMB has its highest spectral radiance at 160 GHz (see figure 2.1**(a)**). To measure variations in the temperature of the CMB about this average temperature, we would in general like to measure at frequencies

where $d(\text{Spectral Radiance})/dT_{cmb}$ is greatest[1]. Figure 2.1**(b)** shows that this function is maximized at 220 GHz; frequencies where it is within a factor of 2 of this peak are between 100 and 380 GHz.

Astrophysical foregrounds (signals that originate from astrophysical sources other than the CMB) also play a role in defining the region of the spectrum best for measuring the CMB. Two astrophysical foregrounds are dominant over the spectral range of interest: polarized emission by dust and synchrotron emission by electrons in magnetic fields [20]. The signal from dust emission is increasing as a function of frequency, and the signal from synchrotron emission is decreasing. Because the spatial distribution of the two signals is different, the frequency of minimum foreground signal changes as a function of spatial scale and position on the sky, but is ~ 100 GHz.

For a CMB experiment measuring from the ground, the atmosphere is one unavoidable source of both CMB signal attenuation and the emission of optical power that contaminates the measurement. To minimize this parasitic effect, ground-based CMB experiments observe in spectral bands where the atmospheric attenuation is low (atmospheric windows) between molecular absorption features. The goal is to "fill" the atmospheric window with the spectral band so that the detector is sensing as many CMB photons and as few photons from the atmosphere as possible.

The CMB's blackbody spectrum is well established, so a useful discriminator between signal from the CMB and that from other astrophysical sources is the power in the signal as a function of frequency. For that reason, it is beneficial to map the sky through multiple atmospheric windows. However, broadband anti-reflection coatings for the optical elements within the cryogenic receiver (see section 2.4) are more difficult to construct than those with the 25% fractional bandwidth necessary to utilize the single atmospheric window. For this reason, the initial POLARBEAR receiver consists of detectors with only a single spectral band. In the future, the POLARBEAR experiment will expand its frequency coverage over other atmospheric windows to allow a more thorough examination of the data for astrophysical foreground contamination.

The spectral band for the POLARBEAR experiment is defined by structures within each focal plane pixel, and is designed to exploit the atmospheric window between 120 and 180 GHz. A discussion of the exact location and shape of the spectral band is left until chapter 6.

2.2 Telescope

As discussed in chapter 1, the B-mode anisotropies due to gravitational lensing are of an angular scale such that the peak of their power spectrum is at $\sim 0.1°$. Characterizing this signal therefore requires an experiment with this resolution on the sky. Achieving this resolution with an imaging experiment requires a primary

[1]This is only exactly true if the experiment's throughput and noise are independent of frequency, neither of which will be true in a real experiment.

aperture large enough that its diffraction-limited beam is smaller than this[2]. The angular resolution of an imaging telescope is given by

$$\theta_{res} \propto \frac{\lambda}{D}, \tag{2.1}$$

where λ is the wavelength of observation, D is the diameter of the telescope[3], and the constant of proportionality is a quantity close to unity that depends on exactly how angular resolution is defined and how the telescope's primary aperture is illuminated by the detectors [21]. The details of equation 2.1 are discussed further in chapter 4; for the purpose of this section, requiring $\theta_{res} = 0.05^\circ$ results in $D \approx 2$ m.

The sensitivity of the experiment must be such that it can make the desired measurement within a reasonable time (as compared to the human lifetime, or more importantly, the lifetime of a typical funding-agency grant). This sets a requirement on the electromagnetic throughput (product of $A\Omega$, where A is the effective area of the primary aperture and Ω is the integral over the angular field of view (FOV) of the experiment). For a given primary aperture size, a wider FOV optical system (a larger Ω) results in a larger electromagnetic throughput. It is important to reiterate that the sensitivity of the experiment is *not* dictated by the size of the primary aperture alone, but rather the throughput of the optical system, because CMB photons are arriving from all directions (it is a completely distributed source).

The Huan Tran Telescope (HTT) is shown in figure 2.2. It has a precision primary aperture (a reflector) 2.5 meters in diameter to provide the angular resolution necessary to characterize the predicted B-modes due to gravitational lensing [22, 8]. The HTT optical system was designed to have the large optical throughput necessary for the experiment's high sensitivity, while minimizing instrumental polarization (leakage of the Stokes intensity vector to the Stokes polarization vectors), cross-polarization (leakage between the Stokes polarization vectors), and response outside of the diffraction-limited main beam (sidelobe response) [23, 24, 25].

2.3 Experiment location

There have been successful space-, balloon-, and ground-based CMB experiments, and each type has its strengths. A ground-based CMB experiment must observe through the partially opaque atmosphere, while space and balloon experiments have the benefit that there is very little between them and the CMB. However, balloon flights last at most tens of days, and spacecraft are very expensive and cannot easily be upgraded. Spacecraft have the ability to measure the entire sky, but that is not necessary for the ℓ-range of POLARBEAR, for which observing time is better spent

[2]Interferometry can augment this requirement, but efficient bolometric interferometry is difficult, and the sensitivity requirements of the experiment motivate the use of bolometric detectors

[3]For an off-axis telescope, this diameter is as projected perpendicular to the pointing on the sky

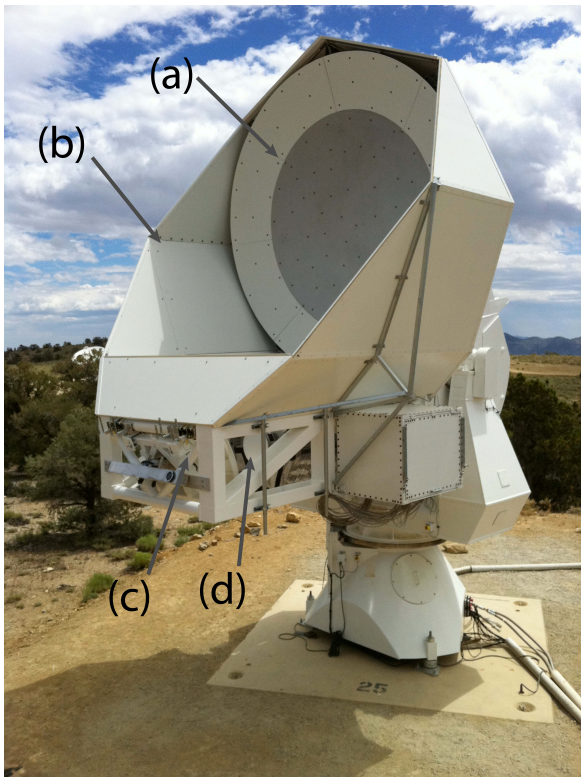

Figure 2.2: The Huan Tran Telescope (HTT) installed at the Cedar Flat site, showing **(a)** the primary reflector, **(b)** the co-moving ground shield, **(c)** the secondary reflector, and **(d)** the cryogenic receiver.

gaining higher sensitivity on one or a few patches of sky. A balloon's short flight time makes it difficult for it to be competitive with ground-based experiments at frequencies where the atmosphere is mostly transmissive. Within the frequency range of interest, atmospheric absorption/emission is dominated by O_2 and H_2O emission, so any ground-based experiment should be located in a high-altitude desert where the atmosphere is thin and dry. The two premier ground-based sites for mm-wave astronomy are the South Pole, which is the driest place on Earth and is at an elevation of 2.8 km, and the Atacama desert in Chile, which is not as consistently dry but is at an elevation of 5.1 km [26].

The South Pole has a six-month winter night with a stable atmosphere and the ability to measure the same patch of sky at the same elevation angle all night long, because the polar location means that from earth the sky appears to rotate around the zenith. From a mid-latitude site, the orientation of a patch of sky with respect to the ground changes over the course of the day and the year (an effect referred to as

sky rotation). This can be an advantage in mitigating systematic instrumental effects [27].

After its engineering run at the Cedar Flat site in Eastern California, POLARBEAR will be sited in the Atacama desert in northern Chile, near the ACT experiment [28, 29].

2.4 Cryogenic receiver

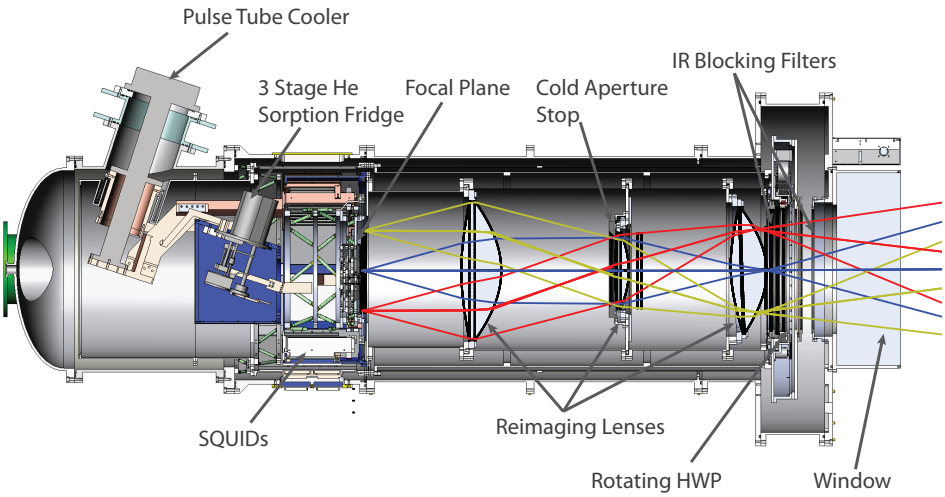

Figure 2.3: Design drawing of the POLARBEAR cryogenic receiver, showing the mechanical and optical design. The labeled elements are discussed in section 2.4. The three colored sets of rays show the optical path through the receiver, each color corresponding to a specific location on the focal plane.

Cryogenic bolometers are the most sensitive detectors of electromagnetic radiation in the frequency range optimized for CMB experiments [30]; individual cryogenic bolometers can be sufficiently sensitive that their noise properties are limited by the intrinsic statistical noise of the radiative signal being detected (referred to as photon noise, see chapter 3 for details) [31]. To achieve that sensitivity, the bolometric detectors must be cooled sufficiently that the detector noise (dominated by thermal carrier noise, see section 3.3) is smaller than the photon noise. Detector temperatures of 0.25 K are sufficient for this purpose. In POLARBEAR, this cooling is achieved using commercial cryogenic refrigeration: a pulse-tube cooler[4] and a three-stage helium sorption refrigerator[5]. To maintain this temperature, the detectors must be shielded

[4]Pulse-tube cooler manufactured by Cryomech, model PT415

[5]Helium sorption refrigerator manufactured by Chase Cryogenics, the 'Berkeley He-10'

by thermal filtering, which is integrated into the POLARBEAR cryogenic receiver. Also in the cryogenic receiver is a rotating Half-Wave Plate (HWP) to provide polarization modulation and three re-imaging lenses that couple the array of detectors to the telescope. Figure 2.3 is a design drawing of the POLARBEAR cryogenic receiver that shows the mechanical and optical design.

Photon noise sets a fundamental limit to the sensitivity of CMB experiments. Any attenuating or scattering medium between the detectors and the CMB will decrease the power reaching the detectors from the CMB itself, and if that attenuating medium is hotter than the CMB, its emission will increase the optical power on the detectors and thus the photon noise. In both of these ways, attenuation and scattering act to decrease the sensitivity of the experiment. For this reason, every element in the optical path should be optimized to serve its purpose with as little attenuation or scattering, and at as low a temperature, as possible.

2.4.1 Thermal filtering

Thermal filtering is provided by the combination of the Zote Foam cryostat window [32], the HWP (which is primarily a polarization modulator, but also blocks thermal radiation), single- and multi-layer metal mesh filters [33], porous polytetrafluoroethylene (PTFE)[6], and the ultra-high molecular weight polyethylene (UHMWPE) re-imaging lenses. Because the re-imaging lenses and the multi-layer capacitive metal mesh filters have significant emissivity within the detector's spectral band (as estimated from the properties of high density polyethylene [34]), they must be kept at low temperature to reduce their contribution to the optical power on the detector.

2.4.2 Half-wave plate

The HWP is a single-crystal disk of A-plane cut sapphire[7]. Because of the difference in optical index along its fast and slow axes [34], a plate 3.1 mm thick acts as a half-wave plate [35]. Rotation of this HWP therefore acts to modulate how polarized signals on the sky are mapped to the polarization-sensitive detectors on the focal plane, and provides a systematic check of the CMB measurement. Thermal emission by the HWP within the spectral band of the detectors is partially polarized along one of its axes [34], and leads to both excess photon noise and a change in optical power that is correlated with the rotation angle of the HWP. The HWP is cooled to 70 K to reduce this thermal emission.

[6]Porous PTFE manufactured by Porex; the porosity produces a lower effective dielectric constant at long wavelengths

[7]Sapphire HWP manufactured by Rubicon

2.4.3 Re-imaging lenses and cold aperture stop

The Gregorian-Dragone telescope is coupled to three cryogenically cooled re-imaging lenses that are anti-reflection (AR) coated with porous PTFE. These lenses produce both an aperture plane within the cryostat and a flat, telecentric focal plane. At the aperture plane, a cold aperture stop suppresses sidelobes by truncating the beam with an absorbing edge taper. The flat, telecentric focal plane is necessary to couple the telescope to a planar array of identical detectors.

2.4.4 Focal plane detector array

The focal plane detector array is designed to maximize sensitivity while minimizing systematic instrumental effects, and is the primary topic in this thesis. Chapter 3 discusses the fundamentals of the sensitivity of the bolometric detectors. Optimization of the pixelization of the focal plane is described in chapter 4. The pixel architecture and fabrication is described in chapter 5, and the optimization of the spectral sensitivity of the pixels is described in chapter 6.

2.5 Detector electrical/digital interface

The Field-Programmable Gate Array (FPGA) based frequency-domain multiplexed readout (DfMUX) is used to electrically bias the bolometers while providing a means for detecting the transition edge sensor's (TES's) response to optical power. It produces AC voltage biases with frequencies between 0.1 and 1 MHz, and biases 8 detectors using a single pair of bias wires. Optical power deposited on the bolometers amplitude modulates the current induced by these voltage biases, and Superconducting Quantum Interference Device (SQUID) amplifiers in a shunt feedback configuration measure that amplitude modulation. This system has been described in, i.e., Spieler *et al.* [36]. Some important points are included below.

2.5.1 SQUID ammeter

TES bolometers operate stably with a low source impedance voltage bias across the thermistor [37]. A change in the incident power on the bolometer changes the bias current flowing through the voltage-biased thermistor. Measuring that changing current requires an ammeter in series with the thermistor. To maintain the voltage bias, this ammeter must present an input impedance significantly smaller than the thermistor impedance. A SQUID amplifier is a low-impedance ammeter. In POLARBEAR, a SQUID ammeter in concert with a room-temperature amplifier in a shunt feedback configuration provides the low-impedance ammeter necessary for reading out the $\sim 1\ \Omega$ bolometers.

2.5.2 Multiplexing

The astrophysical signal being measured is spatially bandwidth-limited by the fact that the telescope has finite resolution (see chapter 4) and averages over the structure on the sky smaller than the telescope beam. Spatial information on the sky translates to temporal information in the timestream of the detectors because the telescope scans across the sky. The telescope scan speed is limited by mechanical constraints, so this limits the temporal bandwidth that can contain astrophysical signal. For ground-based experiments, this is limited to $\sim 10^2$ Hz. Most available amplifiers (and transmission line technologies) perform well over bandwidths significantly larger than this bandwidth of the astrophysical signal of interest. This allows the possibility of multiplexing, where several sensors share the available bandwidth of many of the readout components. Multiplexing promises several significant advantages, described below.

Thermal power

Heat flow through readout transmission lines is a significant component of the thermal loading on all the cryogenic stages. If the signal from n detectors is transmitted on one transmission line, the thermal loading can be a factor of n lower if the single multiplexed transmission line can be thermally identical to the transmission lines used for non-multiplexed sensors. In practice, this is not always possible.

Cost of readout components

The readout hardware is a significant fraction of the total cost of the experiment. Each component that can be used for n detectors rather than one results in a factor of n cost savings on those components.

Power consumption of readout

It is generically true that the readout power consumption will decrease with fewer components, and fewer components are the goal of a multiplexed readout system. For our specific readout system and many likely readout systems in the future, the dominant power consumption is the FPGA. Multiplexing is important to the extent that is utilizes the power consumption of the FPGA efficiently.

Readout wire count

As the number of bolometers in a focal plane increase, the number of wires to read them all out increases. The complexity of routing all the cryogenic wires from room temperature to the detectors is a significant problem. Some aspects of this problem become easier when there are fewer wires, as in a multiplexed system.

2.5.3 Implementation of multiplexing

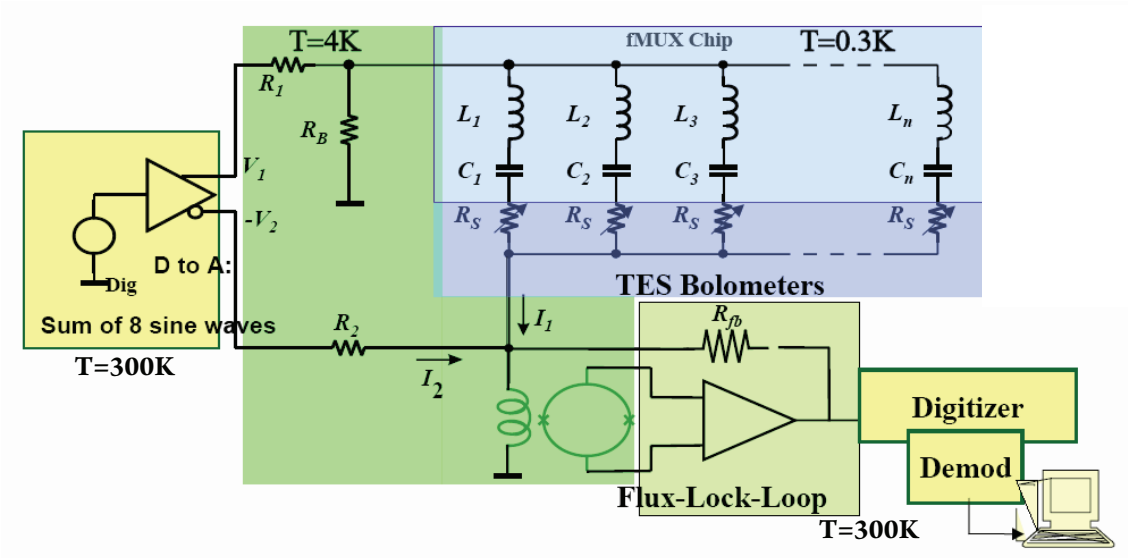

Figure 2.4: Simplified schematic of the POLARBEAR multiplexer circuit. The temperatures of the cryogenic receiver at which different parts of the circuit reside are labelled. The circuit is described in section 2.5.3. The variable resistors R_s represent the bolometers, which change resistance due to changes in incident optical power.

For the reasons described above, POLARBEAR uses a multiplexed readout system. Figure 2.4 shows a simplified circuit diagram for the components attached to a single SQUID in the readout system. In the POLARBEAR system, the multiplexing factor is eight. Each of the eight bolometers is connected in series with a superconducting inductor and a capacitor. This series resonator sets the frequency at which the voltage bias will be applied to the bolometer. Eight of these series resonators are connected in parallel, all at the sub-Kelvin temperature stage. For each set of eight parallel resonators, a single transmission line connects the sub-Kelvin stage to the direct digital synthesizer creating the biasing sine waves. All eight sinusoidal voltage biases are carried by that single transmission line, and are split at the sub-Kelvin stage along the eight separate paths to bias the eight bolometers. As the bolometer resistance changes in response to incident optical power, the amount of current going through each of the bolometers changes, and the current sensed by the SQUID at each frequency is amplitude-modulated. This signal is amplified by the SQUID and its associated shunt-feedback loop, and digitized. It is then demodulated in an FPGA and the demodulated data are stored on disk.

Chapter 3

Bolometer Noise Properties

The dominant noise source fundamental to bolometric detectors receiving no optical power is thermal carrier noise [38]. Also important in bolometric systems are the Johnson noise due to the thermistor and the noise from the readout electronics. When the bolometer is exposed to radiation, these noise sources are added in quadrature with the photon noise due to the radiation. This chapter describes all of these noise sources. Sections 3.1 and 3.2 define some important terminology, section 3.3 derives the bolometer thermal carrier noise and points out the factors that affect it, and section 3.4 describes the photon noise in the signal. Sections 3.5 and 3.6 describe the Johnson and readout noise, and why it is lower than the thermal carrier noise in POLARBEAR. Finally, section 3.7 describes how to relate these noise terms to the CMB signal.

3.1 Power spectral densities

It will be useful to first present some definitions of the quantities used here to describe noise properties. It is often interesting to know the frequency distribution of the power in a timestream, be it noise or signal. This is called the power spectral density of the timestream. To correctly measure the power in a discretely sampled timestream, the timestream must be sampled at the nyquist sampling rate Δt_{nyq}, where

$$\frac{1}{\Delta t_{nyq}} = 2 f_{max}, \tag{3.1}$$

with f_{max} the maximum frequency at which there is power in the signal. The magnitude squared of the discrete Fourier transform (DFT) of the timestream is then the power spectral density of the timestream. This $|\mathrm{DFT}|^2$ is normalized so that the integral of the $|\mathrm{DFT}|^2$ over positive frequencies up to f_{max} is equal to the mean variance per discrete timestream sample, $\overline{\sigma^2_{sample}}$ [39]. To illustrate this, consider a timestream

with power spectral density that has no dependence on frequency (this is referred to as *white*). This integral is trivial, and

$$\overline{\sigma^2_{sample}} = \int_{f=0}^{f_{max}} |\mathrm{DFT}|^2 \, df = |\mathrm{DFT}|^2 \cdot f_{max}. \tag{3.2}$$

Bolometer noise is often referred to power at the input of the bolometer. If this signal is being measured in W, the power spectral density of the signal has units of W^2/Hz. For a signal dominated by noise, the Noise Equivalent Power (NEP), with units of $\mathrm{W}/\sqrt{\mathrm{Hz}}$, is the square root of the power spectral density. If the NEP is white, equation 3.2 applies, and can be rewritten as

$$\overline{\sigma^2_{sample}} = \int_{f=0}^{f_{max}} |\mathrm{NEP}|^2 \, df = |\mathrm{NEP}|^2 \cdot f_{max}. \tag{3.3}$$

The NEP is interpreted as the power that a signal with 1 Hz of bandwidth would have to have to be equal to the noise in the power spectrum of the timestream. There is another slightly different way of quoting noise level: the power a signal would have to have in order to have a Signal-to-Noise Ratio (SNR) of one after measuring for 1 second. Let's call this quantity the Timestream NEP (NEP_t). Since the timestream samples are assumed to be independent, and the number of samples per second is equal to $1/\Delta t_{nyq}$, the mean variance in the signal after 1 second of measurement is given by

$$\overline{\sigma_1^2} = \overline{\sigma^2_{sample}} \cdot \Delta t_{nyq} = \frac{\overline{\sigma^2_{sample}}}{2 f_{max}} = \frac{|\mathrm{NEP}|^2}{2}, \tag{3.4}$$

where the simplifying example of white noise is again used with equations 3.1 and 3.3. The NEP_t is then equal to the square root of this mean variance, or

$$\mathrm{NEP}_t = \frac{\mathrm{NEP}}{\sqrt{2}}. \tag{3.5}$$

Although this discussion showed only the equations for white bandwidth-limited noise, the definition above holds true for any noise spectrum.

3.2 Definition of bolometer parameters

Figure 3.1 shows a cartoon drawing of a bolometer. The thermally released area is at operating temperature T_c. The thermal bath to which it is attached is at operating temperature T_b. The operating power P_{oper} is the sum of all the power sources incident on the bolometer during operation: the optical power and the power deposited by the voltage bias. Changes in the bias current through the bolometer are a measure of the changing optical power incident on the bolometer [40]. The thermal link between the thermally released area and the thermal bath is made of a material with temperature-dependent thermal conductivity $k(T)$.

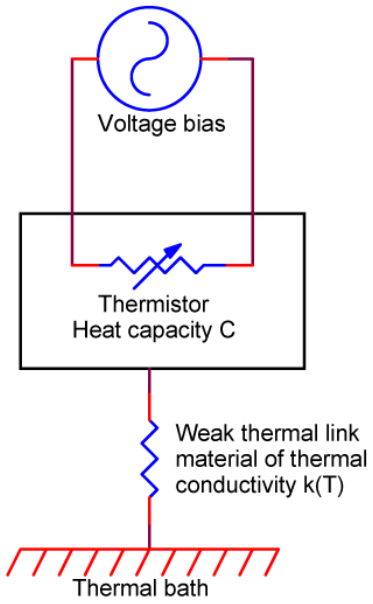

Figure 3.1: A cartoon drawing of a bolometer. The thermally released area is at operating temperature T_c. The thermal bath to which it is attached is at temperature T_b. The operating power P_{oper} is the constant power flowing across the thermal link during operation. The thermal link between the thermally released area and the thermal bath is made of a material with temperature-dependent thermal conductivity $k(T)$.

3.3 Thermal carrier noise

One unavoidable source of noise in bolometric detectors is the fundamental energy fluctuation noise in the bolometer. This is generally referred to as *thermal carrier noise*, referring to the source of the detected power fluctuations, the thermal energy carriers themselves. This distinguishes it from *photon noise*, which refers to power fluctuations in the incoming photons, and *Johnson noise* (or *Nyquist noise*), the electronic noise due to thermal motion of the charge carriers. This section presents an analysis of the thermal carrier noise to be expected in bolometers, applicable to a wide range of bolometer parameters.

3.3.1 Fundamental power fluctuations

A fundamental property of macroscopic systems is that the energy fluctuations in the system ΔE are related to the heat capacity C_v of the system by [41]

$$\langle \Delta E^2 \rangle = kT^2 C_v. \tag{3.6}$$

For two systems of the same temperature T separated by thermal conductance g, equation 3.6 can be rewritten as

$$\langle \Delta P^2 \rangle = kT^2 C_v \frac{g^2}{C_v^2} = \frac{kT^2 g^2}{C_v}. \tag{3.7}$$

The power spectral density of power fluctuations is white at low frequencies and bandwidth limited with a single-pole roll-off at frequency f_0 given by [42]

$$f_0 = \frac{g}{2\pi C_v}. \tag{3.8}$$

The white level (low frequency limit) of the power spectral density of the power fluctuations, NEP_g, can be calculated by setting

$$\int_0^\infty \frac{\mathrm{NEP}_g^2}{1 + \left(\frac{f}{f_0}\right)^2} df = \frac{kT^2 g^2}{C_v} \tag{3.9}$$

$$\Rightarrow \mathrm{NEP}_g^2 \cdot f_0 \cdot \frac{\pi}{2} = \frac{kT^2 g^2}{C_v} \tag{3.10}$$

$$\Rightarrow \mathrm{NEP}_g^2 = 4kT^2 g. \tag{3.11}$$

3.3.2 Thermal conductance parameters

There is thermal conduction between the TES thermistor at temperature T_c and the bath at temperature T_b. That thermal conduction can be parameterized in a variety of ways. The two used here are the average thermal conductance $\bar{G}$ and the small signal thermal conductance g. As their names suggest, they are defined by

$$\bar{G} = \frac{P_{oper}}{T_c - T_b}, \tag{3.12}$$

$$g = \frac{dP_{oper}}{dT_c}, \tag{3.13}$$

where P_{oper} is the total power being deposited on the bolometer, and the derivative in 3.13 does not depend on feedback. g and $\bar{G}$ are different if the thermal link between the bolometer and the bath is constructed of material with a thermal conductivity that depends on temperature.

Assuming a thermal conductivity model for this material of $k(T) = k_0 T^n$, the power P flowing through any one differential length of the thermal link δx is related to the temperature drop across that length of thermal link δT by $P\delta x = Ak(T)\delta T$, where A is the effective cross-sectional area of the thermal link. This equation can be integrated to find an expression for the power flowing across the thermal link:

$$P_{oper} = \int_{T_b}^{T_c} \frac{A}{l} k(T) dT = \frac{A}{l} \frac{k_0}{n+1} (T_c^{n+1} - T_b^{n+1}). \tag{3.14}$$

For a thermal link with no temperature dependence ($n = 0$), the thermal conductance of the thermal link is related to the constant thermal conductivity k_0 of the material by the simple relationship, $g = \bar{G} = \frac{A}{l} k_0$.

3.3.3 Connection to previous work

The average thermal conductance $\bar{G}$ of a bolometer is the operating power of the bolometer at operating temperature T_c, divided by the difference between T_c and the temperature of the thermal bath, T_b. For a bolometer with no optical load, the operating power is just the bias power, so $\bar{G}$ can easily be measured with no assumptions about the thermal link between the TES and the bath.

In the limit that $T_c \approx T_b$ (*not* the limit the POLARBEAR bolometers are in), the spectral density of thermal carrier noise (which will be referred to as NEP_g) can be calculated directly from equation 3.11 as

$$\text{NEP}_g = \sqrt{4kT_c^2 g} \text{ (for } T_c \approx T_b). \tag{3.15}$$

The parameter that is generally set by outside experimental constraints is the total operating power on the bolometer, P_{oper}. Once that is set, NEP_g can be rewritten using 3.12 (and the *incorrect* approximation $T_c \approx T_b \Rightarrow g \approx \bar{G}$) as

$$\text{NEP}_g = \sqrt{4kP \frac{T_c^2}{T_c - T_b}} \text{ (for } T_c \approx T_b). \tag{3.16}$$

Given a bath temperature T_b (set by balancing noise requirements with cryogenic technological constraints), The T_c at which NEP_g is minimized can easily be found analytically from equation 3.16 to be $T_c = 2T_b$. Clearly, the assumption $T_c \approx T_b$ has been broken, so a more careful investigation is warranted. Without the assumption $T_c \approx T_b$, the spectral density of thermal carrier noise is [38]

$$\text{NEP}_g = \sqrt{\gamma 4kT_c^2 g}, \tag{3.17}$$

where

$$\gamma = \frac{\int_{T_b}^{T_c} \left(\frac{Tk(T)}{T_c k(T_c)}\right)^2 dT}{\int_{T_b}^{T_c} \frac{k(T)}{k(T_c)} dT} = \frac{1}{T_c^2 k(T_c)} \frac{\int_{T_b}^{T_c} (Tk(T))^2 dT}{\int_{T_b}^{T_c} k(T) dT}. \tag{3.18}$$

Again assuming a model $k(T) = k_0 T^n$ for the thermal conductivity of the thermal link material, equation 3.18 can be simplified to

$$\gamma = \frac{n+1}{2n+3}\frac{1-(T_b/T_c)^{2n+3}}{1-(T_b/T_c)^{n+1}}. \tag{3.19}$$

Writing NEP_g in terms of P_{oper} and T_b:

$$\begin{aligned}
\mathrm{NEP}_g &= \sqrt{4k\gamma T_c^2 g} && (3.20)\\
&= \sqrt{4kP_{oper}T_b}\sqrt{\frac{(n+1)^2}{2n+3}\frac{T_c}{T_b}\frac{1-(T_b/T_c)^{2n+3}}{\left(1-(T_b/T_c)^{n+1}\right)^2}} && (3.21)\\
&= \sqrt{4kP_{oper}T_b}\sqrt{\frac{(n+1)^2}{2n+3}\frac{(T_c/T_b)^{2n+3}-1}{\left((T_c/T_b)^{n+1}-1\right)^2}}. && (3.22)
\end{aligned}$$

The thermal carrier noise has a very simple dependence on P_{oper} and T_b, going as the square root of these quantities. The rest of expression in equation 3.22 depends only on the temperature profile of the weak thermal link (n), and the ratio of the T_c to T_b.

3.3.4 Special materials

It is now interesting to narrow this discussion to special values n, shown in table 3.1. Notice that γ does not go to 1 when $n = 0$ (no temperature dependence in the thermal conductivity). Specifically,

$$\forall n, \lim_{T_c \to T_b}(\gamma) = 1, \text{ but for } T_c \neq T_b, \gamma \neq 1. \tag{3.23}$$

Thermal carrier	n	γ
no temperature dependence (hypothetical)	0	$\frac{1}{3}\frac{1-(T_b/T_c)^3}{1-(T_b/T_c)}$
electrons	1	$\frac{2}{5}\frac{1-(T_b/T_c)^5}{1-(T_b/T_c)^2}$
phonons	3	$\frac{4}{9}\frac{1-(T_b/T_c)^9}{1-(T_b/T_c)^4}$

Table 3.1: Thermal carrier noise nonequilibrium factor (γ) for some special materials

Choosing T_c/T_b to minimize NEP_g is now more complicated than it was with equation 3.16, but can easily be done. The location of this minimum, along with its value, are given in table 3.2. This result is valid for all bath temperatures T_b and bolometer operating powers P_{oper}. With these optimal transition temperatures,

$$\mathrm{NEP}_{g,phonons,optimal} = 1.19 \cdot \mathrm{NEP}_{g,electrons,optimal}. \tag{3.24}$$

Note that the incorrectly chosen $T_c = 2T_b$ from section 3 is a fairly good choice for a bolometer with a metal link, but a worse choice for a bolometer with a phonon

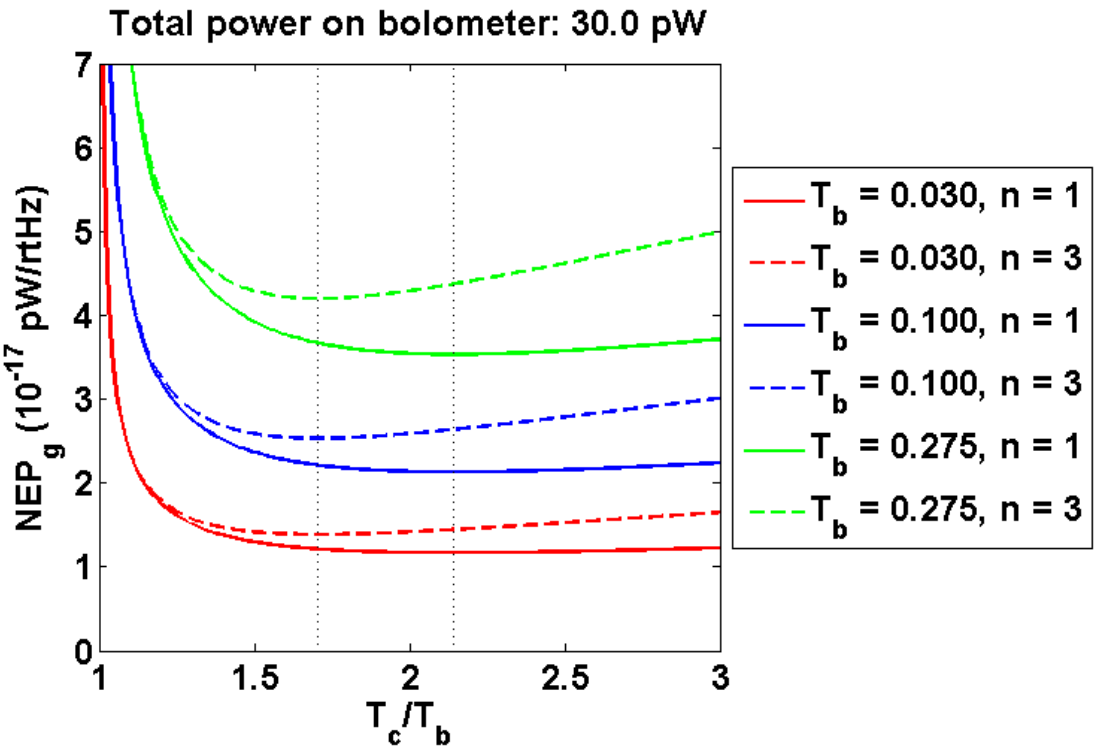

Figure 3.2: NEP_g as a function of T_c for several bath temperatures T_b. The dashed black lines show the T_c/T_b ratio at which NEP_g is minimized, which does not depend on the total power P_{oper} or the bath temperature T_b.

n	T_c/T_b	$\mathrm{NEP}_g/\sqrt{4kP_{oper}T_b}$
0	2.732	1.468
1	2.143	1.655
3	1.705	1.967

Table 3.2: Optimized transition temperature T_c and the thermal carrier noise NEP_g associated with that optimum.

thermal link. It is interesting to point out that for a hypothetical link with no temperature dependence, the minimum is at a significantly higher T_c, and the noise level at that minimum is lower. It is also interesting to point out the coincidence that for $n = 3$ and $T_c = 2T_b$, $\gamma g = \bar{G}$ to closer than 1%, making the incorrect equation $\mathrm{NEP}_g = \sqrt{4kT_C^2\bar{G}}$ seem valid, though this is just a coincidence for this specific point in parameter-space.

Figure 3.2 shows NEP_g as a function of TES temperature T_c for $n = 1$ and $n = 3$ at several bath temperatures. For a reasonable bath temperature of 0.275 K, optimal transition temperatures are 0.59 K for electron thermal carriers and 0.47 K for phonon thermal carriers.

Sensitivity to fabrication errors

The two parameters set by fabrication are the geometry and material of the thermal link (characterized by the index of the thermal conductivity n and what will be referred to as the geometrical factor $\frac{A}{l}\frac{k_0}{n+1}$) and the bolometer transition temperature T_c. Both of these are likely prone to variations. The impact of these variations on NEP_g and P_{oper} is shown in figure 3.3. Note that the minimum NEP_g, which is in the center of all these figures, does not appear to be a minimum because P_{oper} is not being held constant (as is clear in figure 3.3**(b)** and **(d)**). The bolometer parameters were optimized for $P_{oper} = 30$ pW, which is why that power appears in the center of those plots. Note that the $n = 3$ case is considerably more sensitive to fabrication errors, both in P_{oper} (which in turn affects the size of the readout noise as well, because a higher voltage bias will be needed), and in NEP_g.

Material selection

The unambiguous conclusion is that electron thermal carriers are preferable to phonon thermal carriers. The POLARBEAR detectors have a thermal link consisting of low-stress nitride, silicon dioxide, and superconducting niobium. Low-stress nitride films of this thickness from the UC Berkeley Microlab has been shown to have $n \approx 2$ [43, 44]. n for the other materials is unknown, although there are clearly very few electron thermal carriers. $n = 3$ is used for all the noise calculations in the following chapters.

3.4 Photon noise

For a thermal source of temperature T emitting radiation, the Boltzmann occupation number n_{occ} is defined as

$$n_{occ} = \left(e^{\frac{h\nu}{k_bT}} - 1\right)^{-1}. \tag{3.25}$$

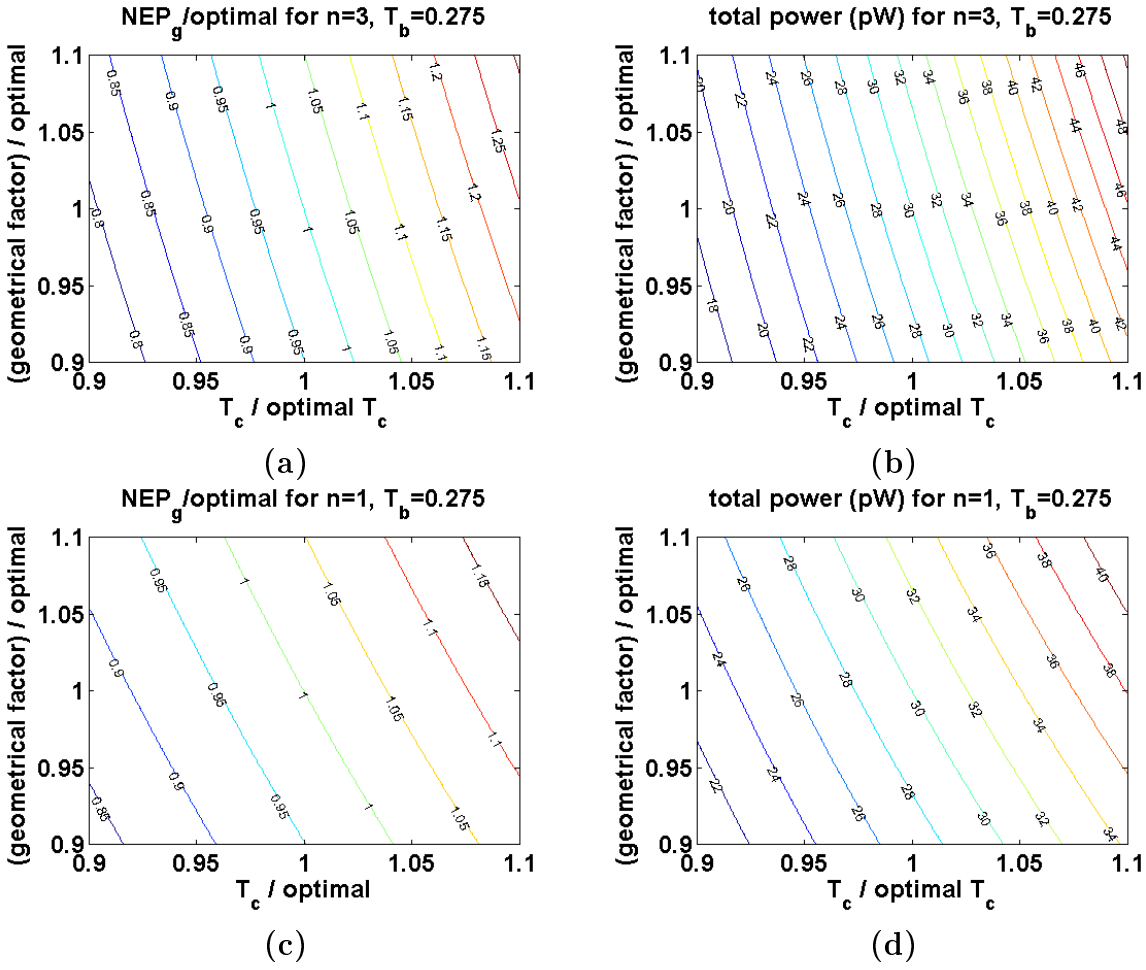

Figure 3.3: Bolometer properties: sensitivity to fabrication errors. **(a)** and **(b)** show NEP_g and P respectively as a function of non-optimal T_c and $\frac{A}{l}\frac{k_0}{n+1}$ for phonon thermal carriers ($n = 3$). **(c)** and **(d)** are the same plots for electron thermal carriers ($n = 1$).

h is Planck's constant, ν is the frequency of the radiation, and k_b is Boltzmann's constant. This is interpreted as the average number of photons per spatial mode as a function of frequency [45]. Since each photon has energy $h\nu$, the integrated power in a single mode from a thermal source to which the sensor is connected with frequency-dependent efficiency $\eta(\nu)$ is

$$P_\gamma = \int_\nu \eta(\nu) h\nu n_{occ} d\nu. \tag{3.26}$$

There will be fluctuations in the radiative power incident on any measuring apparatus. The variance in the measured optical power after a time τ will be [45]

$$\sigma^2 = \frac{1}{\tau} \int (h\nu)^2 \eta n_{occ}(1 + \eta n_{occ}) d\nu. \tag{3.27}$$

Note the two terms within the integral, one $\propto \eta n_{occ}$ and one $\propto (\eta n_{occ})^2$. When the photon occupation number is small (for high frequency or low temperature), the first term dominates. This is the optical limit, where Poisson statistics dictate the variations in the arrival rate of the photons, and thus the uncertainty in any measurement of the power scales as the square root of the power. When the photon occupation number is large (low frequencies or high temperatures), the second term dominates. This is the radio limit, where the photons are highly bunched, and the uncertainty in the power scales linearly with the power. Note that in this limit, a noiseless detector does not gain in SNR by receiving more power, since the signal is proportional to the noise. For reference, figure 3.4 shows the photon occupation number as a function of frequency and temperature.

The POLARBEAR detectors are in the transition between the two limits. It is worth noting that the correlated term in the noise has not been experimentally verified for bolometric detectors, although it is well known in coherent detectors. The ACBAR experiment saw photon noise slightly smaller than the equation above would suggest [46], so it may be reasonable to assume some decorrelation of the photons in the system, resulting in an actual noise between the value suggested by the equation above and the value that would be suggested by only assuming the Poisson noise factor. However, any decorrelation in ACBAR may be due to specifics of those detectors, which were of significantly different architecture. In designing POLARBEAR and the noise analysis in chapter 7, equation 3.27 was taken to be correct. Equation 3.4 can be used to convert the photon noise to an NEP at the bolometer input:

$$\mathrm{NEP}_\gamma = \sqrt{2 \int (h\nu)^2 \eta n_{occ}(1 + \eta n_{occ}) d\nu}. \tag{3.28}$$

In the limit that $\eta(\nu)$ is sharply peaked at ν_0 with integrated bandwidth $\Delta\nu_I$, equation 3.28 becomes

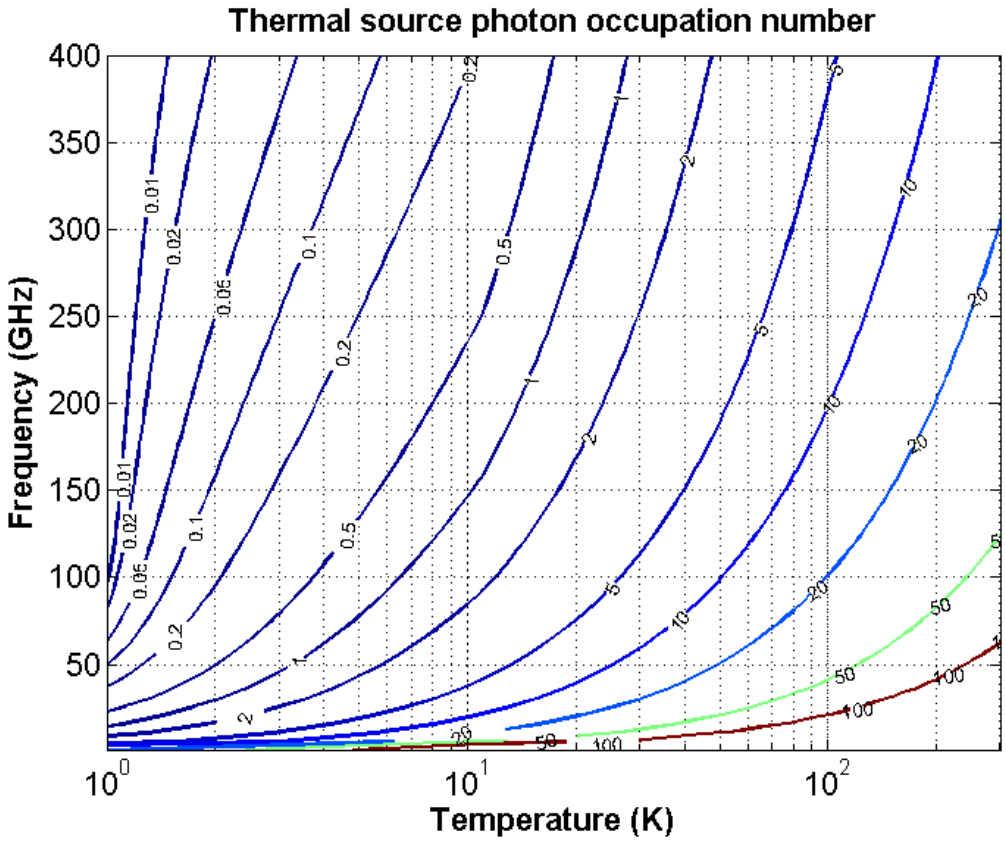

Figure 3.4: Boltzmann photon occupation number n_{occ} as a function of frequency and temperature.

$$\mathrm{NEP}_\gamma \approx \sqrt{2}\sqrt{h\nu_0 P_\gamma + \frac{P_\gamma^2}{\Delta\nu_I}}, \tag{3.29}$$

where P_γ is the photon power incident on the detector. The validity of this approximation varies with source temperature (spectrum of n_{occ}), but for the POLARBEAR design band and thermal source above 50 K, the approximation overestimates the photon noise by 7 to 8 %.

3.5 Johnson noise

The Johnson (or Nyquist) noise from a resistor of resistance R at temperature T_c can be written in terms of the noise equivalent current produced in a loop of resistance R_{loop} as

$$\mathrm{NEI} = \frac{1}{R_{loop}}\sqrt{4k_b T_c R}. \tag{3.30}$$

For a bolometer operating with electrothermal loop gain $\mathcal{L}$ [37], and R_{loop} dominated by R so that $R_{loop} \approx R$, the current noise is reduced by the electrothermal feedback to be [38][1]

$$\mathrm{NEI}_{johnson} = \frac{1}{\mathcal{L}}\sqrt{\frac{4k_b T_c}{R}}. \tag{3.31}$$

This current noise can be referred to a power signal at the input of the bolometer using the current responsivity of the bolometer, S_I, where

$$S_I = -\frac{1}{V_{bias}}\frac{\mathcal{L}}{\mathcal{L}+1}. \tag{3.32}$$

Combining equations 3.31 and 3.32, The Johnson noise referred to the input of the bolometer is

$$\mathrm{NEP}_{johnson} = \frac{\mathcal{L}+1}{\mathcal{L}^2}\sqrt{4k_b T_c P_{bias}}. \tag{3.33}$$

Here P_{bias} is the power deposited on the thermistor by the voltage bias V_{bias}. It is most useful to compare this to the thermal carrier noise on the bolometer, or as done in section 3.3, to the quantity $\sqrt{4kP_{oper}T_b}$:

$$\frac{\mathrm{NEP}_{johnson}}{\sqrt{4kP_{oper}T_b}} = \frac{\mathcal{L}+1}{\mathcal{L}^2}\sqrt{\frac{P_{bias}}{P_{oper}}\frac{T_c}{T_b}}. \tag{3.34}$$

Since the quantity under the square root is similar to unity and the POLARBEAR bolometers are designed to operate in the regime where $\mathcal{L} \gg 1$, the Johnson noise is always smaller than the thermal carrier noise.

3.6 Readout noise

The noise in an ammeter can be characterized by its noise equivalent current $\mathrm{NEI}_{readout}$. This quantity will be used here to encompass all of the noise sources in the readout system, as referred to the input of the SQUID amplifier. It can be referred to the input of the bolometer as a noise equivalent power using the bolometer responsivity in equation 3.32.

[1] In the nomenclature of [38], the $\mathcal{L} = (R-Z)/(R+Z)$, with R the resistance of the bolometer and Z the dynamic impedance.

$$\begin{aligned} \mathrm{NEP}_{readout} &= V_{bias}\frac{\mathcal{L}+1}{\mathcal{L}} \cdot \mathrm{NEI}_{readout} && (3.35)\\ &\approx V_{bias} \cdot \mathrm{NEI}_{readout} && (3.36)\\ &= \sqrt{RP_{bias}} \cdot \mathrm{NEI}_{readout}. && (3.37) \end{aligned}$$

Again, comparing this to the standard quantity,

$$\frac{\mathrm{NEP}_{readout}}{\sqrt{4kP_{oper}T_b}} = \mathrm{NEI}_{readout}\sqrt{\frac{R}{4kT_b}}\sqrt{\frac{P_{bias}}{P_{oper}}}. \quad (3.38)$$

For the POLARBEAR detectors and the DfMUX readout, $\mathrm{NEI}_{readout} \approx 7$ pA/$\sqrt{\mathrm{Hz}}$, $R \approx 1\ \Omega$, and $P_{bias}/P_{oper} \approx 0.6$, so

$$\frac{\mathrm{NEP}_{readout}}{\sqrt{4kP_{oper}T_b}} \approx 1.5. \quad (3.39)$$

Comparing to table 3.2, this is similar to but just less than the optimal thermal carrier noise values. The noise of the POLARBEAR bolometers with no optical power on them is dominated by thermal carrier noise.

3.7 Noise equivalent temperature on the CMB

It is also useful to refer noise values in the system to the CMB itself. Given a detector NEP and the electromagnetic throughput from the CMB that the detector is sensing, the NET_{cmb} is the temperature fluctuation on the CMB that would create enough power in the signal at the detector to have a SNR of 1 after 1 second of integration time. In the parlance of section 3.1, this is the "Timestream NET". The change in power due to a differential change in CMB temperature T_{cmb} is given by

$$\frac{dP_\gamma}{dT_{cmb}} = (h^2/k)\int \eta(\nu) n_{occ}^2 (\nu/T_{cmb})^2 e^{\frac{h\nu}{kT_{cmb}}} d\nu. \quad (3.40)$$

The conversion between NEP_t and NET_{cmb} is

$$\mathrm{NET}_{cmb} = \frac{\mathrm{NEP}_t}{\frac{dP}{dT_{cmb}}}. \quad (3.41)$$

In this dissertation all of the noise equivalent powers quoted are NEP, not NEP_t, so it is more useful to write

$$\mathrm{NET}_{cmb} = \frac{\mathrm{NEP}}{\sqrt{2}\frac{dP}{dT_{cmb}}}. \quad (3.42)$$

Chapter 4

Focal Plane Pixelization

As is mentioned at the beginning of section 2.4, individual cryogenic bolometers can be so sensitive that their noise properties are limited only by the intrinsic noise of the radiative signal being detected. The radiative signal of interest here is the electromagnetic radiation focused onto the focal plane by the optics of the POLARBEAR instrument. If all of the electromagnetic power in this signal could be deposited on a single bolometer, this bolometer would be able to make the highest SNR measurement of the total power incident on the telescope. However, the measurement would not achieve the spatial resolution discussed in section 2.2, because the detector would be summing the power from several adjacent diffraction-limited spots on the sky; the angular resolution would just be equal to the field of view of the telescope. Achieving spatial resolution requires pixelization of the focal plane. This chapter will describe some of the principles guiding such a pixelization.

4.1 Point-source resolution

Pixelization of the focal plane is required to achieve the resolution as limited by the primary aperture size. This resolution is often discussed in terms of the telescope's distortion of a point source, or its point-spread function.

An astrophysical point source illuminates the primary aperture uniformly with a flat wavefront. In the geometric ray-optics limit, the primary aperture focuses this uniform illumination down to a point on the focal plane. However, diffraction limits the telescope's ability to refocus to an arbitrarily small point. Fourier optics provides a convenient method of obtaining the actual pattern on the focal plane when reimaging a point source [35]. Since the primary aperture is not infinite in size, uniform illumination of the primary aperture is actually a circular top-hat illumination, with no power outside the primary aperture. This is shown schematically with a simple refracting telescope in figure 4.1. The intensity on the focal plane is plotted as a

function of radial distance on the focal plane in $F\lambda$, where λ the wavelength of the electromagnetic radiation and

$$F = \frac{f}{D} \tag{4.1}$$

is the *f-number* of the telescope, with D the primary aperture diameter and f the effective focal length.

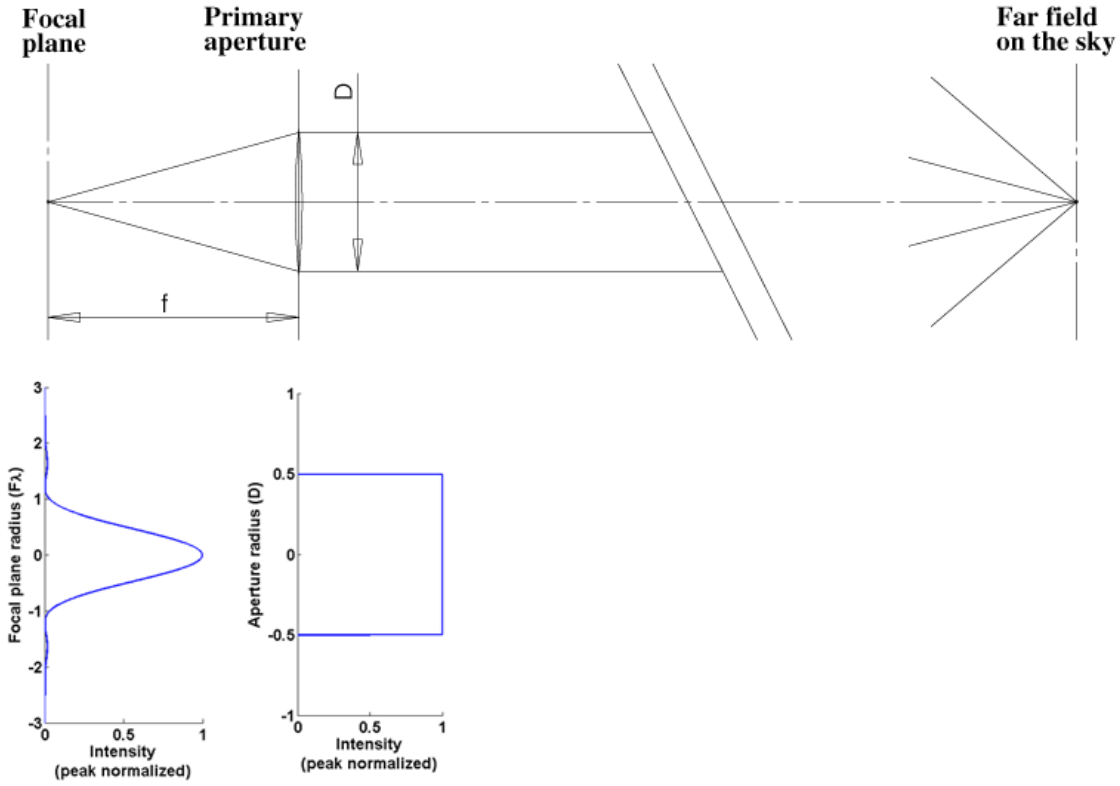

Figure 4.1: Schematic drawing of a simple refracting telescope imaging an astrophysical point source on boresight. Images below the schematic show the power of the illumination at that plane.

4.2 The pixel in transmission

It is useful to look at the same simple schematic of a telescope, considering a pixel that transmits uniformly into all forward angles and illuminates the aperture uniformly. The transmitted pattern on the sky is then the Fourier transform of the circular top-hat illumination pattern, as shown in figure 4.2. The beam from the pixel

(in transmission) is equivalent to the pixel's spatial sensitivity (in reception) [47]. In the example of figure 4.2, the pixel's sensitivity to a point source directly on boresight is twice as high as its sensitivity to a point source an angle of $0.5\frac{\lambda}{D}$ off boresight.

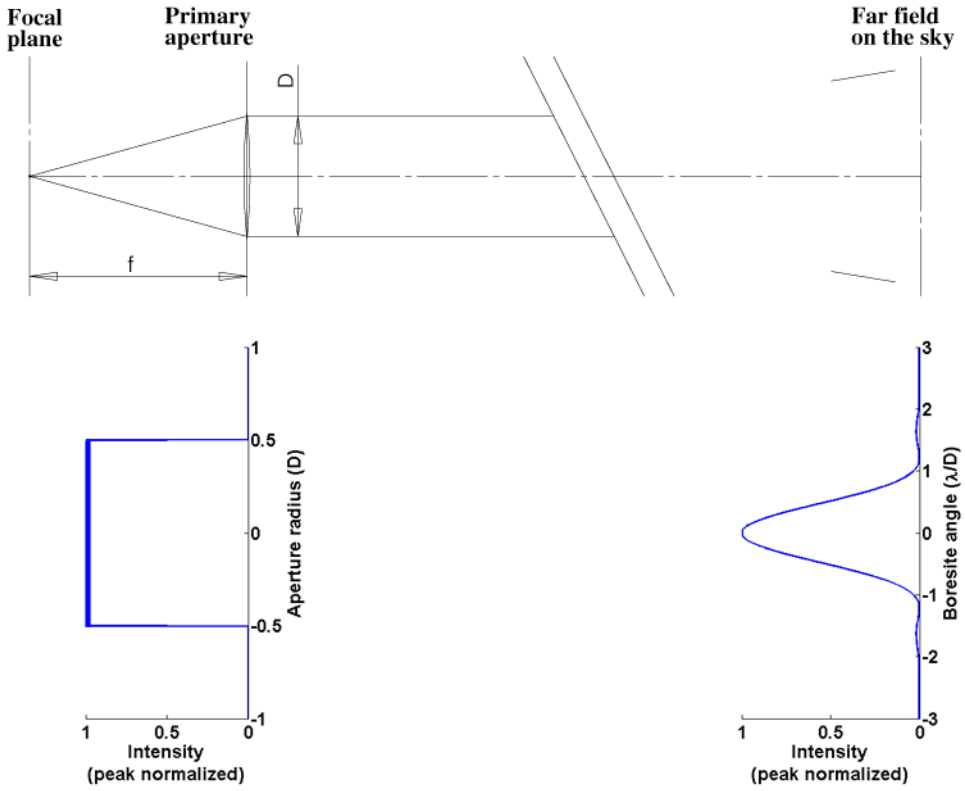

Figure 4.2: Schematic drawing of a simple refracting telescope with a single pixel transmitting a beam to the sky. Images below the schematic show the intensity on that plane. The pixel's beam on the sky (in transmission) is equivalent to its spatial sensitivity (in reception).

4.3 Single- and multi-moded pixels

The above section referred to a hypothetical pixel that senses radiation from all angles uniformly. In practice, pixels in mm-wave experiments can be categorized into two groups: multi-moded and single-moded pixels.

The angular sensitivity of a multi-moded pixel is usually dictated by geometric concerns. The simplest example of such a pixel is a flat absorber that collects all radiation incident upon it. Such an absorber has spatial sensitivity $b(\theta) \propto \cos(\theta)$, where θ is the angle from the boresight of the pixel. This beamshape is simply because

the pixel's projected area decreases as $\cos(\theta)$. Its electromagnetic throughput is $A\pi$, where A is the area of the pixel and $\pi = \int_\Omega \cos\theta d\Omega$.

Single-moded pixels have total electromagnetic throughput λ^2 [42]. The selection of a single electromagnetic mode is achieved by coupling a free-space wave to a guided wave, with the wave-guiding structure only supporting a single propagating mode. Radiation that does not couple to this propagating mode is reflected back away from the pixel. The most common example of such a pixel is a horn coupled to a waveguide, with an absorber at the other end of the waveguide. The absorber itself would be multi-moded, but since it is coupled to the waveguide, it only has access to a single mode of radiation. The horn acts to couple the single propagating mode in the waveguide to a single propagating mode in free space. Such a structure is generically called an antenna—a horn is a type of antenna.

There are several examples of single-moded pixel architectures, including different waveguide and horn designs, waveguide probes that feed radiation into a planar waveguide, and phased arrays of planar antennas. In the case of the POLARBEAR pixel, a planar double-slot dipole coupled to a lenslet acts to couple radiation into the single-moded microstrip waveguide before that radiation is spectrally filtered and then deposited onto the bolometer.

In a single-moded pixel, the spatial sensitivity is dictated by the fields/currents that can be driven on the antenna by the single propagating mode. In general, the spatial beam function $b(\theta)$ can be very complicated. For pixel architectures that are useful in CMB experiments, the beam functions of single-moded pixels are often characterized by their Gaussisity and beamsize (θ_{FWHM}). Gaussisity is the fraction of the beam that couples to the free-space propagating mode of Gaussian profile. This is a unique mode because it is the propagating mode with the smallest diffraction-limited divergence [22]. In the diffraction-limited case, the divergence angle of the beam goes as the inverse radius of the pixel, as in equation 2.1 of section 2.2. In this case, the illumination pattern that the pixel (in transmission) makes on the primary aperture depends on the size of the pixel. The illumination pattern is the beam function of the pixel, truncated at an angle $\theta_{trunc} = \arctan\frac{1}{2F}$.

4.4 The cold aperture stop

The previous sections have focused on the radiation transmitted through the primary aperture, but not the radiation from around the aperture. From the point of view of the detector, the primary aperture takes up a solid angle $\Omega \approx \frac{\pi}{4}F^2$, which for reasonable F may be about a third of the 2π solid angle in front of the detector. Since the noise on the detector is set by the amount of optical power deposited on it, it is unacceptable to let this power be dominated by radiation not transmitted through the optics of the telescope. A low-temperature box around the detectors and a low-temperature aperture stop around the primary aperture will decrease this parasitic

power. This setup is shown schematically in figure 4.3. The low-temperature box must be very cold to not be a significant source of power on the detector. In practice, the ratio of this box temperature to the effective temperature of the atmosphere is the important quantity for a ground-based experiment.

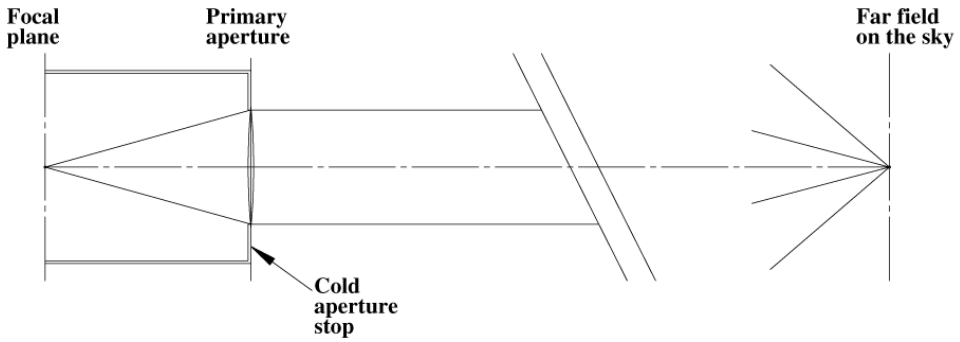

Figure 4.3: Schematic drawing of a simple refracting telescope showing a cold aperture stop at the aperture lens. This cold aperture stop reduces the power on the detectors from outside the aperture. However, it is difficult to implement without more complicated optics.

Figure 4.3 presents a problem. Section 2.2 sets the primary aperture size at ~ 2 m. This then requires cooling an absorbing cryogenic box to a few Kelvin with a > 2 m window to allow a clear view of the primary aperture. This is untenable with current cryogenic technology. A solution that still allows the area around the aperture to be cold is to create an optical system that produces a demagnified image of the primary aperture inside the cryostat where it can be shrouded by the cold aperture stop. The cold aperture stop reduces radiation on the pixel from large angles, and defines the illumination on the primary. In transmission, the pixel beam is truncated, and that truncated beam is imaged onto the primary aperture. In the optical ray limit, the pixel can only receive radiation from the cold box or the primary aperture.

The shadow of the aperture stop does not simply image through the system, but rather the beamshape propagates in a diffraction-limited manner, and sharp discontinuities in the aperture plane correspond to spatial ringing in the field plane. That spatial ringing, called sidelobes, can terminate on a hot surface and increase loading on the bolometer. Far sidelobes can be reflected down onto the ground or some other hot source, and become responsible for a systematic instrumental effect. The sidelobes can be reduced by illuminating the aperture with a power profile that is smoothly decreasing from the center toward the edge, so that the discontinuity at the edge is smaller.

4.5 Resolution and pixel size

A pixel with a beam profile that has decreased substantially (and smoothly) by θ_{trunc} will have a smaller portion of the beam diffracted out to large angles inside the cryostat. For POLARBEAR, where control of the spatial beam is so important, only single-moded pixel architectures—pixels that have a more directed beam—were considered. However, if the beam is so small that it only illuminates the inner part of the primary aperture, this is equivalent to having a smaller primary aperture, and thus it results in a larger diffraction-limited resolution on the sky.

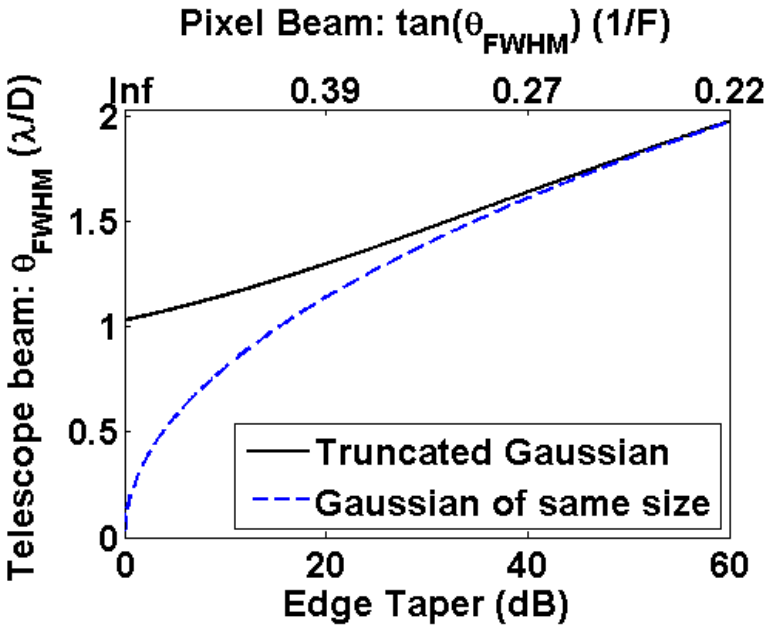

Figure 4.4: Telescope beam Full Width at Half Maximum (FWHM) as a function of Gaussian edge taper in dB (bottom axis) or equivalently, pixel beamwidths in units of inverse F (top axis). At the left end of the plot, the curve asymptotes to the value associated with uniform illumination of the primary aperture. At the right end, the truncation of the illumination pattern is unimportant, and the beam FWHM approaches that of an unobscured Gaussian beam of the same size.

The illumination of a primary aperture by a pixel producing a Gaussian beam can be characterized by the edge taper of the illumination, given in dB by

$$\text{Edge Taper [dB]} = -10 \log_{10} \frac{P_{edge}}{P_{center}}. \tag{4.2}$$

Figure 4.4 shows the beamwidths on the sky (θ_{FWHM} of the main lobe) produced by a primary aperture of diameter D for different Gaussian edge tapers, or equiva-

lently, pixel beamwidths in units of inverse F (this figure is similar to those in [48, 21]). Note that the beam width increases by 40% (as compared to uniform illumination) for a Gaussian illumination pattern with an edge taper of 30 dB. Less aperture-filling illumination patterns were not considered. Toward the 0 dB edge taper side of figure 4.4, there is a maximum power at truncation that can be allowed while maintaining tolerable sidelobe performance in the optical system. This is characterized in figure 4.5 below.

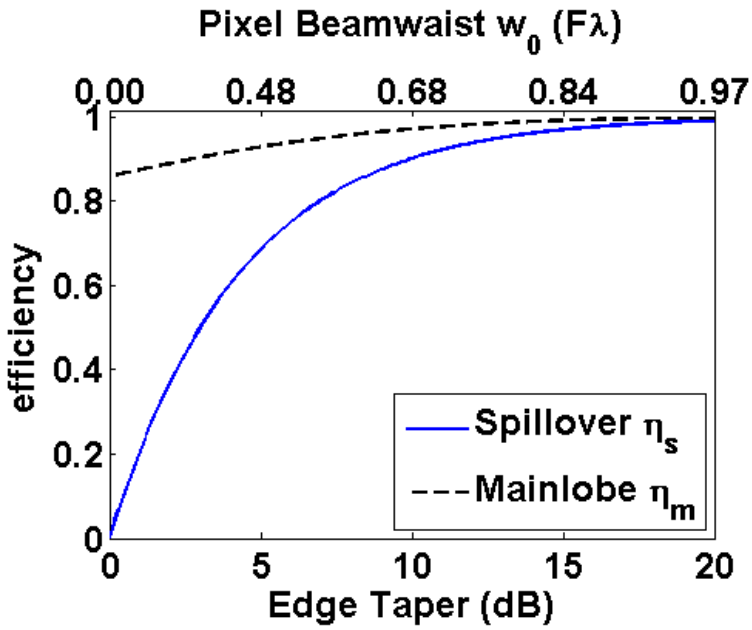

Figure 4.5: The spillover efficiency, η_s, and the mainlobe efficiency, η_m, as a function of the Gaussian edge taper. Note the horizontal axis has changed scale as compared to figure 4.4. η_s is simply the fraction of the power in the complete Gaussian beam that falls within the primary aperture and is not truncated. η_m is the fraction of the beam on the sky that falls within its main lobe.

The primary aperture is in the far field of the focal plane pixel, so the angular size of the Gaussian beam, in the paraxial limit, is related to its waist at focus by [22]

$$\theta_{FWHM} = \frac{\sqrt{2\ln 2}}{\pi}\frac{\lambda}{w_0}. \tag{4.3}$$

Much as the telescope primary aperture size was matched to the required resolution of the experiment, the pixel size must be matched to the desired illumination pattern on the telescope.

In optimizing the size of the pixel, it is useful to define three quantities. Following the notation of [21]:

- Spillover efficiency η_s is the amount of the beam from the pixel that is inside the truncation angle θ_{trunc}. The rest of the beam $1 - \eta_s$ senses only radiation from inside the cold box around the aperture stop.

- Aperture efficiency η_a is the coupling of the pixel beam to an astrophysical point-source. Since POLARBEAR is not designed to observe point sources, η_a is not a particularly valuable metric.

- Mainlobe efficiency η_m is the fraction of the beam on the sky that is in the central lobe (inside of the first minimum). This increases as the edge taper increases, but at the expense of having a larger main lobe.

Figure 4.5 is a plot of the η_m and η_s as a function of edge taper (bottom axis). The top axis of figure 4.5 is the waist size of the Gaussian beam on the focal plane that would create such an illumination pattern. As the edge taper decreases, η_s decreases, but since the pixel size is decreasing, the number of pixels that can fit on the focal plane increases. How these two effects change the sensitivity of the experiment is the subject of section 4.7. At very low edge tapers (uniform illumination), a significant part of the power in the beam is not in the main lobe, as characterized by η_m.

4.6 Comparison of some pixel types

The previous sections have referred to a single-moded pixel on the focal plane coupling to a Gaussian beam of waist w_0. This section will compare a few antennas for this purpose.

A corrugated horn of entrance diameter D couples to a Gaussian beam with waist size w_0 at the focal plane, with $D = 1.6 \cdot 2w_0$. The Gaussisity of the corrugated horn is 0.98 [49]. An interesting figure of merit for a pixel is the *pixel's* taper efficiency, $\eta_{\tau,pixel}$. This is the ratio of the integration over the illumination pattern of the pixel to the pixel's diameter. This can be analyzed by approximating the illumination pattern as a truncated Gaussian, just as was done for the primary aperture. The pixel taper efficiencies $\eta_{\tau,pixel}$ for a few pixel types are given in table 4.1.

A conical horn couples to a Gaussian beam with waist size w_0 related to the diameter of the horn aperture by $D = 1.3 \cdot 2w_0$. This pixel architecture collects more of the electromagnetic throughput at the focal plane then a corrugated horn of the same diameter. The POLARBEAR pixel, a synthesized elliptical lenslet coupled to a crossed double-slot dipole antenna, is described in detail in section 5.1.1. Correctly implemented, the $\eta_{\tau,pixel}$ and Gaussisity of this pixel is very similar to that of a conical horn [50, 51]. The details of producing a lenslet-coupled pixel with these properties are discussed in section 5.1.1.

Pixel type	$\eta_{\tau,pixel}$	Gaussisity
Corrugated horn	0.69	0.98
Smooth-walled horn	0.81	0.90
dipole-coupled lenslet	0.81	0.90

Table 4.1: Column 1 lists some common antenna types. Column two is the taper efficiency of the *pixel* (not the telescope), as described in the text. This is calculated assuming the beam is the Gaussian beam to which the antenna best couples. The third column is the antenna beam's Gaussisity.

4.7 Pixel size optimization

Using the relationship between the pixel size and the Gaussian beamwaist that it couples to, the pixel size optimization is a matter of optimizing the illumination on the primary aperture while taking into account the total power on the pixel. As the pixel size changes, the power from the cold aperture stop scales as $1 - \eta_s$, while the power from everything on the sky side of the aperture stop (including the rest of the instrument, the atmosphere, and the CMB itself) scales as η_s. For each pixel size, the total optical power P_γ, the power from the CMB P_{cmb}, and the noise on the detector (NEP) is calculated. This is enough information to determine the SNR on each detector and thus the SNR of the entire focal plane, as characterized by its mapping speed, defined in section 4.7.2.

4.7.1 Noise scaling

In the limit of a very opaque atmosphere, the photon noise from the atmosphere is strongly bunched, so that $NEP_\gamma \propto P$ (see section 3.4). In that limit, the SNR from photon noise for a single detector is not changed by limiting the detector throughput, except for the noise generated by the cold aperture stop (it is assumed that the detector operating power is reoptimized for any pixel size so that the detector noise decreases with the expected loading). If the SNR for a single detector remains constant with pixel size, but smaller pixels allow more detectors to be within the FOV, then the array sensitivity increases with smaller pixel size.

In the optical limit of high frequencies and/or a more transmissive atmosphere, the photon noise from the atmosphere and the instrument will be dictated by Poisson statistics, and $NEP_\gamma \propto \sqrt{P}$. In this limit, the SNR is reduced with smaller pixel size, and there is competition between the decreasing SNR of a single detector, and the added signal due to many detectors.

The POLARBEAR experiment is between the two regimes. The precise instrument model used in the optimization below is given in table 6.1.

4.7.2 Definition of mapping speed

The extended source mapping speed of an array is defined for the purposes of this chapter as

$$S = \frac{N_{det}}{\mathrm{NET}_{cmb}^2}, \tag{4.4}$$

where N_{det} is the number of detectors in the array, and NET_{cmb} is the noise equivalent temperature at the CMB for a single detector. The units of mapping speed used in the plots below are $(\mu\mathrm{K}^2\mathrm{s})^{-1}$. This means that, for a map of the CMB binned into n_{map} pixels, and an observing time τ that is spread evenly between those pixels, the SNR on a $1\mu K$ signal, $SNR_{1\ \mu K}$, is given by

$$SNR_{1\mu K} = S\frac{\tau}{n_{map}}. \tag{4.5}$$

It is important to note that S goes as the inverse NET squared, so to get the same SNR on a signal of 0.5 μK takes four times as long.

4.7.3 Assumptions

Due to fabrication constraints, the actual numbers of pixels that will fit in a focal plane is not a continuous function. To illuminate the dependencies, this section will assume a number of pixels proportional to the inverse pixel-pixel distance squared. To normalize this relationship, table 4.2 is used. Table 4.2 shows the number of pixels of a nominal size that can fit on a single hexagon cut out of a 4" wafer. Seven hexagonal wafers fill the POLARBEAR focal plane array. The analysis is done for three monochromatic focal plane designs, each sensitive to a different spectral band.

Freq (GHz)	pixel-pixel distance (mm)	pixel-pixel distance ($F\lambda$)	pixels/wafer
94.3	9.56	1.67	37
147.8	6.79	1.86	91
224	4.25	1.76	217

Table 4.2: The number of pixels of various sizes that can fit in the POLARBEAR focal plane, for three possible center frequencies. This was used as the starting point for the pixel size optimization calculations for the POLARBEAR focal plane.

4.7.4 Comparison of the two sites (photon noise only)

The differing atmospheric opacities of the Chilean and Cedar Flat sites have a noticeable effect on the pixel size optimization (the details of atmospheric modeling

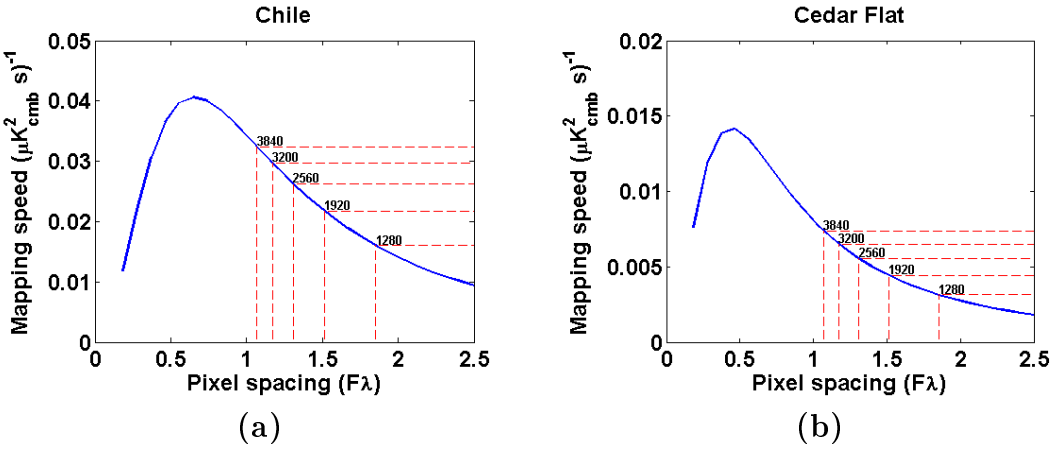

Figure 4.6: Mapping speed as a function of pixel spacing, accounting for photon noise only. Pixel spacing is 1.05 times pixel diameter. Atmosphere is simulated for a 30° zenith observation angle at **(a)** the Chilean site with 1 mm precipitable water vapor and **(b)** the Cedar Flat site with $\tau_{225,z} = 0.28$. Note that the two plots have differing vertical axis scale. Details of the spectral band optimization are in chapter 6. Dashed lines delineate the number of bolometers needed to fill the 19 cm diameter $F = 1.8$ field of view on the POLARBEAR focal plane. The aperture stop temperature is 6 K.

and the spectral response of the detectors are described in chapter 6). Figure 4.6 shows the mapping speed for the pixels with spectral band centered at 147.8 GHz as a function of pixel separation for the Chilean and Cedar Flat sites, accounting for only the photon noise. By looking at where the red lines intersect the vertical axis, note the relationship between mapping speed and detector number. For the Cedar Flat site, the mapping speed is closer to being proportional to N_{det}, because there is less NET change per detector as a function of η_s. Also notice where the peak of the mapping speed curve lies. At Cedar Flat, maximum mapping speed is at smaller pixel size, because the ratio of the power from the Cedar Flat atmosphere to the power from the 6 K aperture stop is higher.

4.7.5 Analysis of the Chilean site (all noise sources)

Figure 4.7**(a)** is the same as figure 4.6**(a)**, but with all noise sources accounted for. Note that the peak in mapping speed has moved to larger pixel size, because of the finite detector and readout noise that is introduced with each detector. This analysis is done with $P_{bias} = 1.5 \cdot P_\gamma$. To isolate the effect of the aperture stop loading, compare figure 4.7 plots **(a)** and **(b)**, which are the same but for a difference in aperture stop temperature. Notice that the maximal mapping speed is lower for the 1 K aperture stop, as it was for the hotter Cedar Flat atmosphere shown in figure 4.6**(b)**.

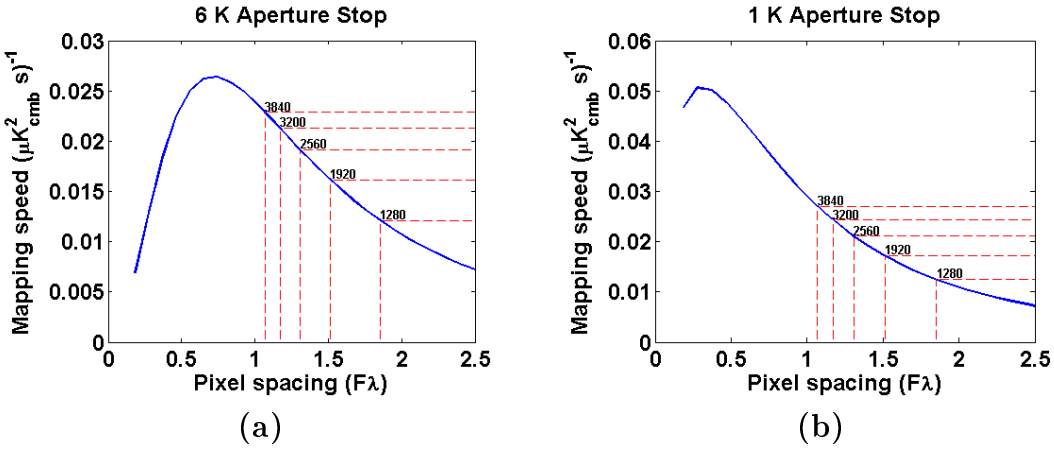

Figure 4.7: Mapping speed as a function of pixel spacing, accounting for all noise sources, for aperture stop temperatures of **(a)** 6 K and **(b)** 1 K. Note that the two plots have differing vertical axis scale. Details of the spectral band optimization are in chapter 6. $P_{bias} = 1.5 \cdot P_{\gamma}$. Pixel spacing is 1.05 times pixel diameter. Atmosphere is simulated for the Chilean site at 30° zenith angle, 1 mm precipitable water vapor. Dashed lines delineate the number of bolometers needed to fill the 19 cm diameter $F = 1.8$ FOV on the POLARBEAR focal plane.

Finally, figure 4.8 shows the same analysis as figure 4.7**(a)**, but for the spectral bands centered at 94.3 and 224 GHz.

4.8 The POLARBEAR focal plane array

The initial POLARBEAR focal plane array contains 637 pixels (1274 bolometers) spread over seven hexagonal sub-arrays. This corresponds to a pixel-pixel spacing of 6.8 mm (1.9 $F\lambda$) for the detectors with spectral band centered at 148 GHz. As shown in figures 4.6 and 4.8, the sensitivity of the experiment would be higher with more detectors in the same DLFOV, but the readout challenge of 1300 detectors limited the design of the first POLARBEAR array. The construction of this array is described in the next chapter.

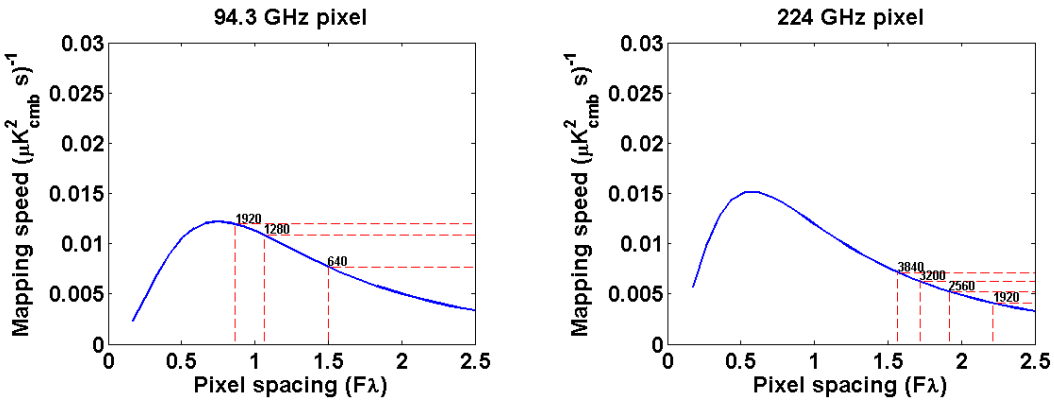

Figure 4.8: Mapping speed as a function of pixel spacing accounting for all noise sources for the spectral bands centered at **(a)** 94 GHz, **(b)** 224 GHz. Details of the spectral band optimization are in chapter 6. $P_{bias} = 1.5 \cdot P_{\gamma}$. Pixel spacing is 1.05 times pixel diameter. Atmosphere is simulated for the Chilean site at 30° zenith angle, 1 mm precipitable water vapor. Dashed lines delineate the number of bolometers needed to fill the 19 cm diameter $F = 1.8$ FOV on the POLARBEAR focal plane. The aperture stop temperature is 6 K.

Chapter 5

Focal Plane Design and Fabrication

Chapter 4 motivates the use of an array of detectors at the focal plane. This chapter describes the array of detectors in POLARBEAR, and the considerations that motivated the design. Section 5.1 describes the focal plane architecture, and section 5.2 describes the fabrication of the focal plane in the Berkeley Microlab.

5.1 Focal plane array architecture

The POLARBEAR detectors integrate several features into a single pixel: polarization-sensitive antennas separate the signal into polarized components and couple these components from free space into superconducting microstrip waveguide, spectral bandpass filtering transmits only the desired frequency band (within the atmospheric window), and superconducting TES thermistors on the thermally released bolometers provide the photon-noise limited detection of the transmitted electromagnetic wave. An overview of this architecture is shown in figure 5.1, which shows a single hexagonal sub-array. The POLARBEAR focal plane consists of seven of these sub-arrays. Figure 5.2 shows a design drawing of the planar structures in the POLARBEAR pixel, of which there is a picture in figure 5.1**(c)**.

The POLARBEAR pixel is designed with the same goals as the entire POLARBEAR optical system: to maximize sensitivity while minimizing systematic instrumental effects. The components are described below.

5.1.1 Antenna design: lenslet-coupled crossed double-slot dipole

Chapter 4, and specifically table 4.1, refer to the pixel beam's Gaussisity and taper efficiency. This section will describe the design of the lenslet-coupled planar antenna that achieves these characteristics. The idea of increasing an antenna's directivity with a directly contacting dielectric lenslet has been used across many applications and spectral regions [52, 53, 54, 55]. This configuration has several benefits:

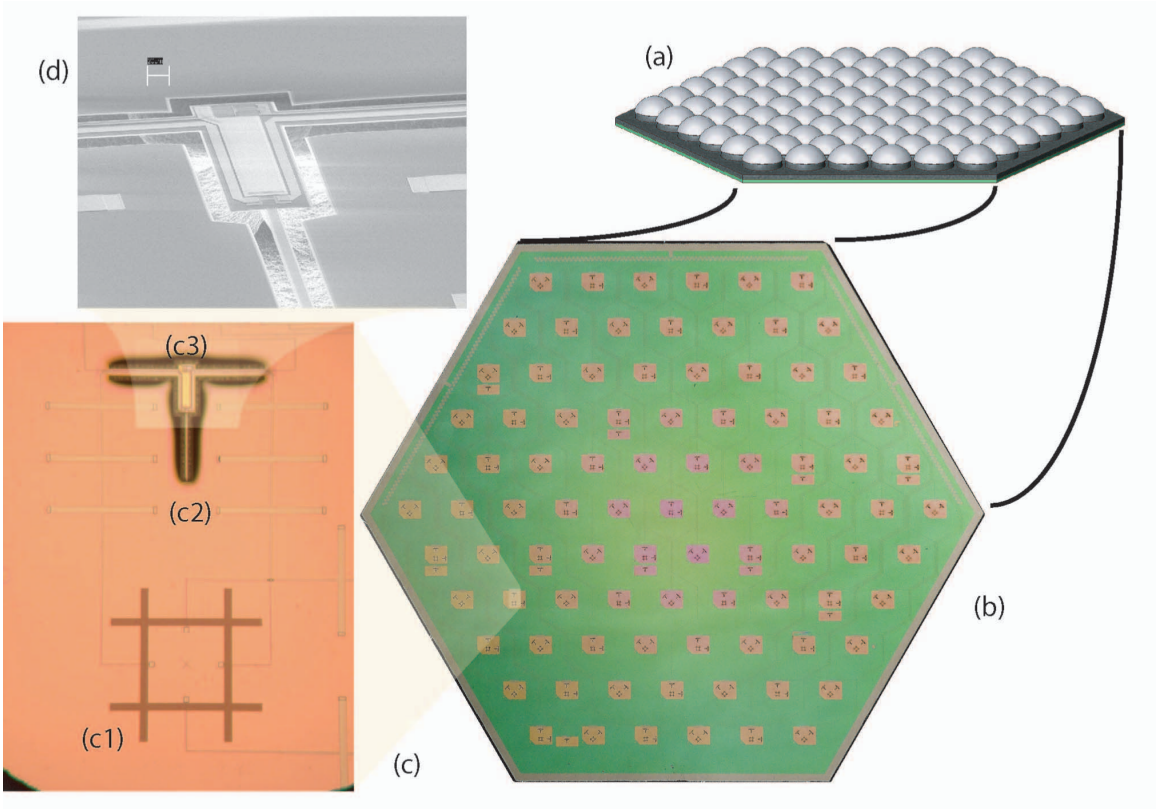

Figure 5.1: A single focal plane sub-array. The POLARBEAR focal plane consists of seven of these sub-arrays. **(a)** The array of contacting dielectric lenslets each with its own anti-reflection coating. Below this is the device wafer, with the devices on the face of the wafer opposite the lenslets. **(b)** The device wafer, a hexagonal array of dual-polarization crossed double-slot dipoles, which separate the signal into its polarized components and transmit each polarization to a bolometer. **(c)** A photograph taken through an optical microscope showing **(c1)** the dual polarization antenna, **(c2)** the microstrip filtering for one of the polarizations, and **(c3)** the bolometer for one of the polarizations. **(d)** A scanning electron micrograph of the bolometer, showing that it is mechanically (and thus thermally) isolated from the silicon substrate, suspended by its three horizontal silicon nitride supports.

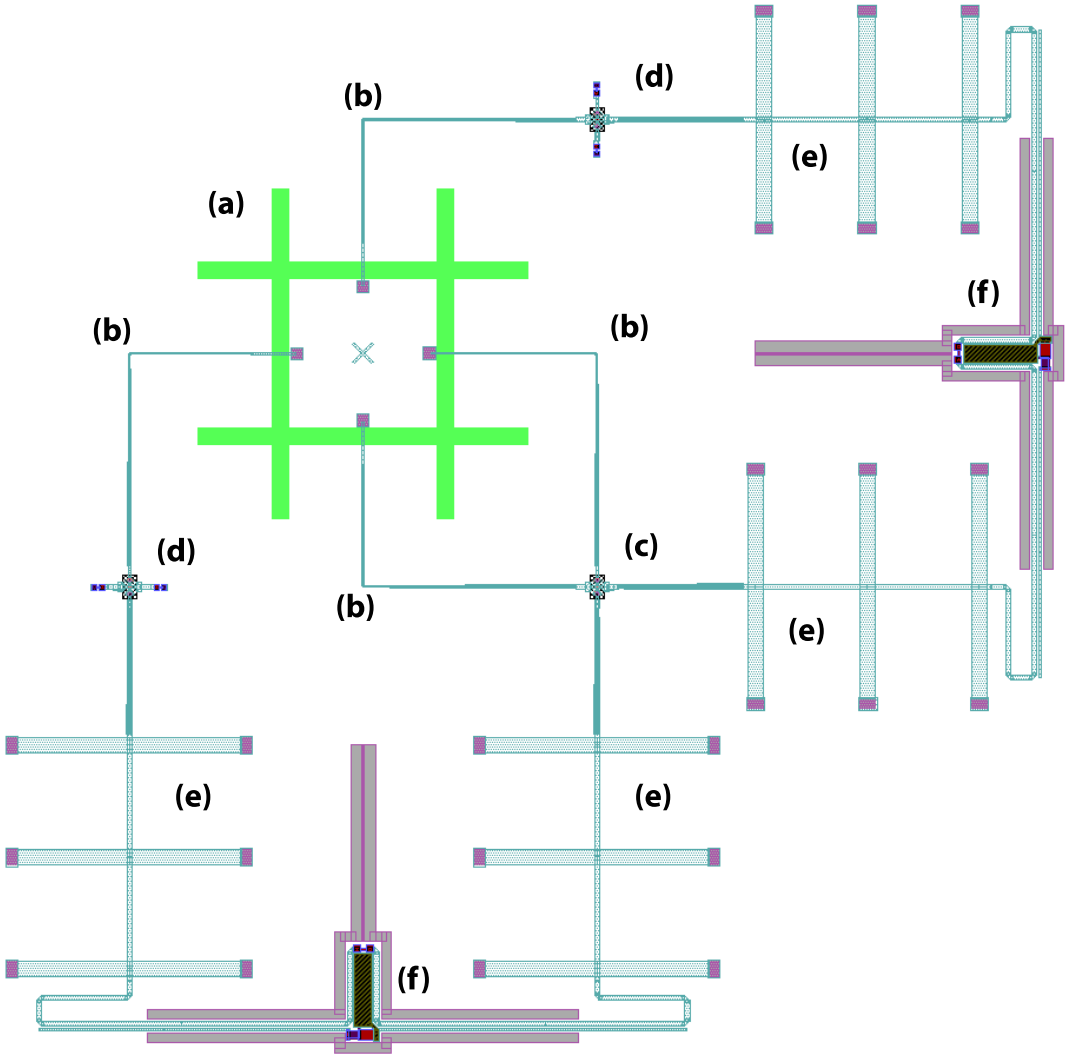

Figure 5.2: A design drawing of the planar structure pictured in figure 5.1(**c**). The structures are labelled in the order that the CMB photon travels through them: (**a**) Crossed double-slot dipole, (**b**) Dolph-Chebychev microstrip transformer (**c**) microstrip cross-under, (**d**) cross-under balancing structures, (**e**) microstrip filters, and (**f**) bolometers. Figure 5.9 shows a more detailed drawing of the bolometer structure.

- Because there is a difference in near-field dielectric constant between the sides of the planar antenna, the beam is formed more strongly in the direction of the high dielectric constant. In the case of silicon, with a relative dielectric constant of 11.7, 91% of the power in the beam goes in that direction [54].

- Standard lithographic techniques produce planar antennas on dielectric substrates. While the radiation is preferentially in the direction of the substrate as described above, that radiation will refract at the substrate boundary, with total internal reflection leading to modes propagating within the planar substrate (often referred to as substrate modes). An extended hemisphere of dielectric material can limit that total internal reflection and eliminate substrate modes.

- The hemispherical dielectric lenslet acts as a beam-forming element, coupling the planar structure's broad beam within the dielectric to a more directed beam in free space. Looking at this in the receiving sense rather than the transmitting sense, the lenslet acts to magnify the active size of the antenna. This leaves room under the lenslet (away from its center) for other microwave elements, without using the valuable focal plane area coupled to the diffraction-limited field of view of the telescope.

- Refracting optics have a wide bandwidth of operation. Given that the lenslet medium has low loss, the loss in coupling to free space is dominated by the reflection loss at the surface of the lenslet. This can be mitigated using an anti-reflection coating. For the POLARBEAR pixel, a single-layer quarter-wavelength anti-reflection coating is sufficient to reduce the reflection loss over the spectral band of interest. In the future, multichroic antennas coupled to lenslets with multi-layer antireflection coatings will have the capability to measure several spectral bands through a single pixel [51, 56].

Dielectric lenslet and anti-reflection coating

In the geometric ray-optics limit, rays from a point source emitter within a dielectric will be refracted to be parallel if the surface of the dielectric is the far side of an ellipse of the correct eccentricity [35]. Figure 5.3**(a)** shows this refraction for an ellipse of the eccentricity required given the optical index of silicon. Using the language of chapter 4, this configuration maximizes the taper efficiency of the pixel. For lenslets of high dielectric constant this eccentricity is small, and thus the ellipse can be well-approximated by an extended hemisphere. Figure 5.3**(b)** shows an extended hemisphere approximating an ellipse, and figure 5.4 shows the transmitted angle for such a lenslet as a function of position on the lenslet surface for several extension lengths, as calculated using ray-optics.

The goal is to produce a pixel that has high taper efficiency $\eta_{\tau,pixel}$ and high Gaussicity. The nominal POLARBEAR pixel size is $R = 1.6\lambda$, with λ the free-space

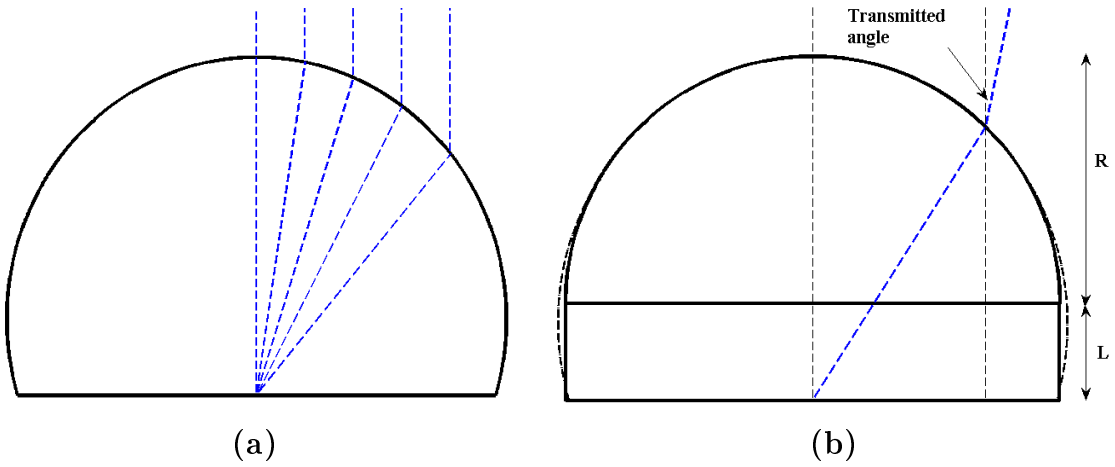

Figure 5.3: Refraction at the surface of a dielectric lenslet for **(a)** an elliptical lenslet and **(b)** an extended hemisphere approximating the elliptical lenslet shape. In the case of the elliptical lenslet, all rays emanating from the center exit the lenslet vertically. In the case of the extended hemisphere, the transmitted angle depends on the extension length and the position on the lenslet surface. This dependence is shown in figure 5.4.

wavelength of the center of the spectral band. For a range of lenslet extension lengths L between $0.36R$ and $0.39R$, the lenslet-coupled double-slot dipole antenna produces a beam with high Gaussisity and directivity [54]. Due to fabrication variability, the POLARBEAR dielectric lenslet extensions have some variability. The above values were chosen as bounds for acceptable extension thickness.

For lenslets of high dielectric constant, the reflection loss at the surface of the lenslet is significant. This reflection loss can be mitigated by employing a quarter-wavelength anti-reflection coating at the lenslet surface. As the extension length increases, the reflectance at the quarter-wavelength coating increases because of the non-normal incidence of the radiation and the curvature of the surface [54]. A re-optimization of the coating thickness as a function of distance from the center of the lenslet dictates that the coating be slightly thicker at the side of the lenslet, but this optimization was not attempted for the POLARBEAR lenslets [51], which were anti-reflection coated with uniform thickness thermoformed polyetherimide, a plastic of optical index 1.7.

Reducing pixel size

Chapter 4 suggests that smaller pixel sizes could lead to a more sensitive experiment. If the pixel size is reduced in future focal planes, some complications should be remembered:

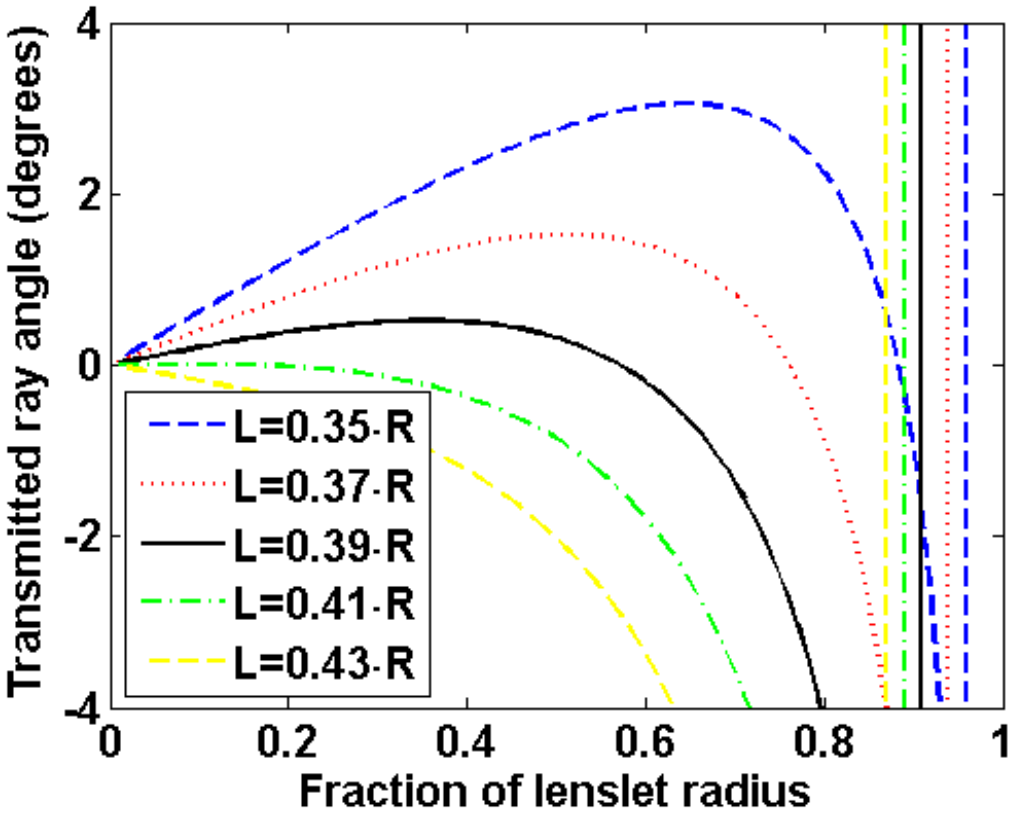

Figure 5.4: Geometric calculation of the transmitted ray angle when exiting the lenslet surface for rays emanating from the center of the planar crossed double-slot dipole. For a true ellipse, this angle would be zero at all points along the radius of the lenslet. The five different lines are for different extension lengths related to the pixel radius as shown in the legend. The vertical lines mark the point after which total internal reflection occurs.

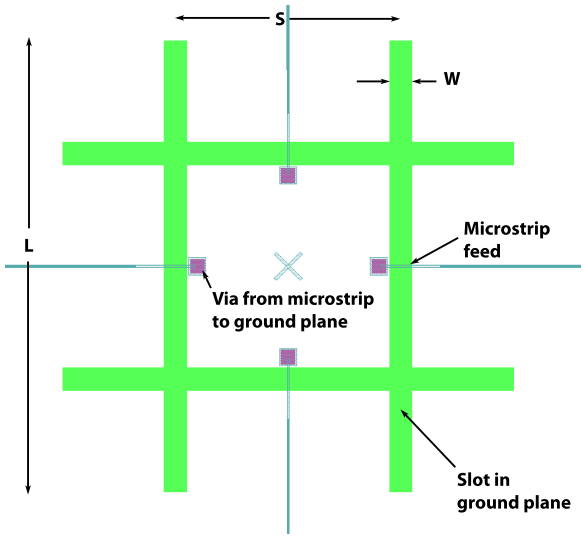

Figure 5.5: Design drawing of the planar crossed double-slot dipole. Areas in green represent slots in the niobium ground plane. Microstrip feeds are shown at the center of each rectangular slot, with a via from the microstrip to the ground plane (in purple) internal to each slot. The incoming radiation excites a voltage across the slot and current around the slot, which excites a propagating wave in the microstrip. For the POLARBEAR pixel, $W = 33.9$ μm $(0.017\lambda_0)$, $S = 338.7$ μm $(0.167\lambda_0)$, and $L = 677.5$ μm $(0.334\lambda_0)$. This antenna was designed to be resonant at 148 GHz.

- The effect of higher power at truncation is spatial ringing in the beam (quantified by the mainlobe efficiency η_m). The edge truncation at which this is unacceptable has not been quantified.
- The predicted beam-shaping properties of the synthesized elliptical lenslet are based on the assumption that the lenslet surface is in the far field of the crossed double-slot dipole, an assumption that clearly breaks down when the lenslet size is smaller than a wavelength.
- The forward gain of the antenna depends critically on an electrically large volume of dielectric on the sky side of the crossed double-slot dipole, which would also break down at sufficiently small pixel sizes.
- Anti-reflection coating of the lenslets requires a quarter-wavelength coating, which does not scale with pixel size, and so for smaller pixels becomes a larger part of the lenslet.

Superconducting planar crossed double-slot dipole

The planar structure coupled to the dielectric lenslet must:

- be able to couple photons efficiently into the on-wafer planar waveguide structures across the desired spectral band.
- have low cross-polarized response across its spatial beam, at least within the angles that transmit through the aperture stop.
- couple efficiently through the lenslet to the diffraction-limited telescope optics.

The resonant crossed double-slot dipole used in POLARBEAR was adapted from the antenna presented in Chattopadhyay and Zmuidzinas [57], which was designed at 500 GHz; the dimensions of the POLARBEAR antenna were scaled so that the antenna would resonate at 148 GHz. A design drawing of the crossed double-slot dipole with dimensions is shown in figure 5.5. This antenna is useful for its relatively low driving impedance (see below), low cross-polarized response, and relatively circular beams [58, 51].

5.1.2 Dolph-Chebychev microstrip transformer

The antenna described above has a resonant impedance of 30 Ω [57, 51]. This impedance is achievable with the microstrip waveguide used to feed the antenna, but because of limitations in the resolution and repeatability of the optical lithography used to print the microstrip, wider (lower impedance) microstrip can be fabricated with greater repeatability. For this reason, the band pass filter is designed to couple to a lower input and output impedance of 10 Ω. A microstrip transformer is used to transition from the antenna impedance to the filter input impedance. Four of these microstrip transformers are used in each pixel, as shown in figure 5.2. As a function of the length along the transformer, l, the design microstrip impedance, Z, is given by [59]

$$Z(l) = Z_{antenna} \cdot e^{\frac{1}{2}\ln\left(\frac{Z_{filter}}{Z_{antenna}}\right)\left[\sin\left(\pi\left(\frac{l}{L}-\frac{1}{2}\right)\right)+1\right]}, \tag{5.1}$$

where L is the total length of the transformer. The transmittance of that transformer, including the effect of the dielectric loss in the microstrip and the microstrip cross-under, is shown in figure 5.6.

5.1.3 Microstrip cross-under

Because of the topology of the antenna, the signals in two of the microstrip lines must cross each other. This is accomplished using a microstrip cross-under structure. The design of this structure is shown in figure 5.7**(a)**. The cross-under was simulated

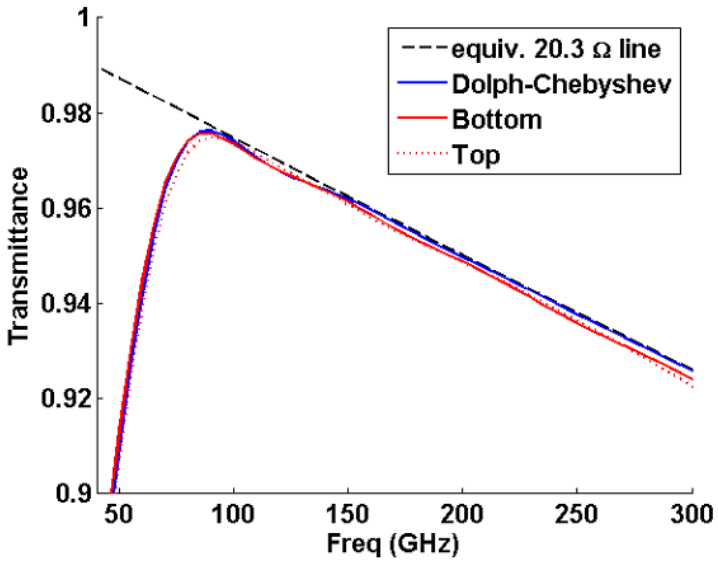

Figure 5.6: Transmitted power ($|S_{21}|^2$) as a function of frequency for the microstrip transformer that connects the antenna to the microstrip filter. This includes dielectric loss, and in the traces labelled 'Top' and 'Bottom', the effect of the microstrip cross-under, discussed in section 5.1.3. the equivalent 20.3 Ω line includes only the dielectric loss in a line of the same length.

using the Sonnet full-wave simulation package. The results of this simulation are shown in figure 5.7**(b)**. The reflected power is less than 1% and the crosstalk power is less than 0.01%.

As shown in the pixel layout in figure 5.2, this cross-under actually occurs in the middle of the microstrip transformer. A network model of the transformer and cross-under was used to optimize the cross-under input lines.

5.1.4 Bandpass filter

The bandpass filter is a standard resonant filter design: a shorted quarter-wavelength stub filter [60]. A shorted stub filter, as compared to an open stub filter, was chosen because the next resonant passband occurs at $3\nu_0$, with ν_0 the design center frequency, rather than at $2\nu_0$ as for an open stub design. As shown in figure 5.8, a network model of the filter closely reflects the results of a full-wave simulation using Sonnet, when the superconducting niobium microstrip is correctly modeled [61]. The parameters of the microstrip filter can be varied to produce filters of different bandwidths and band shapes. These parameters were optimized given the expected atmospheric absorption profile; this optimization is described in chapter 6.

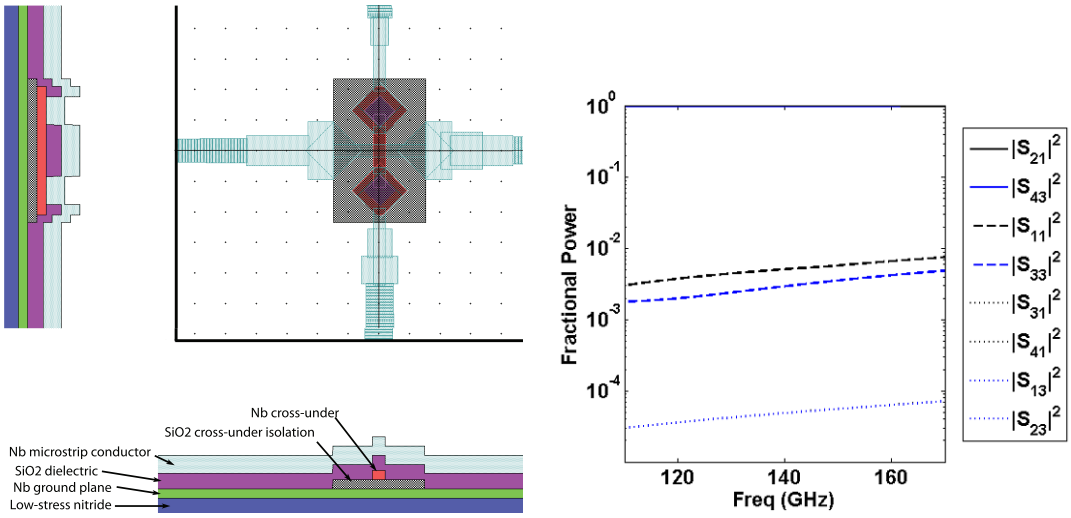

Figure 5.7: Microstrip cross-under **(a)** design and **(b)** simulated performance. **(a)** shows cross-section views from two angles. In the cross-sections, the vertical scale is enhanced by a factor of 10 for clarity. **(b)** shows the scattering parameters as simulated in Sonnet. Ports 1 and 2 connect to the top line, ports 3 and 4 the bottom

5.1.5 Bolometer structure

The fundamental structure of a bolometer (shown schematically in figure 3.1) is: a place where radiative power is deposited that is in thermal contact with a thermistor of heat capacity C, all of which has a weak connection to a thermal bath.

Suspension structure

The weak thermal link between the thermistor and the thermal bath is provided by a silicon nitride suspension with the silicon substrate etched away beneath the suspension. The scanning electron micrograph in figure 5.1**(d)** shows this suspension. The thermal path between the thermistor and the silicon wafer is along the silicon nitride suspension, which is ~ 1 μm in thickness. The operating power of the bolometer is set by the thermal conductance of this suspension and the thermistor's superconducting transition temperature.

Bolometer heat capacity

The electrothermal bandwidth of the bolometer Δf_{et} is proportional to its small-signal thermal conductance, g, the electrothermal loop gain $\mathcal{L}$, and inversely proportional to its heat capacity, C [37]:

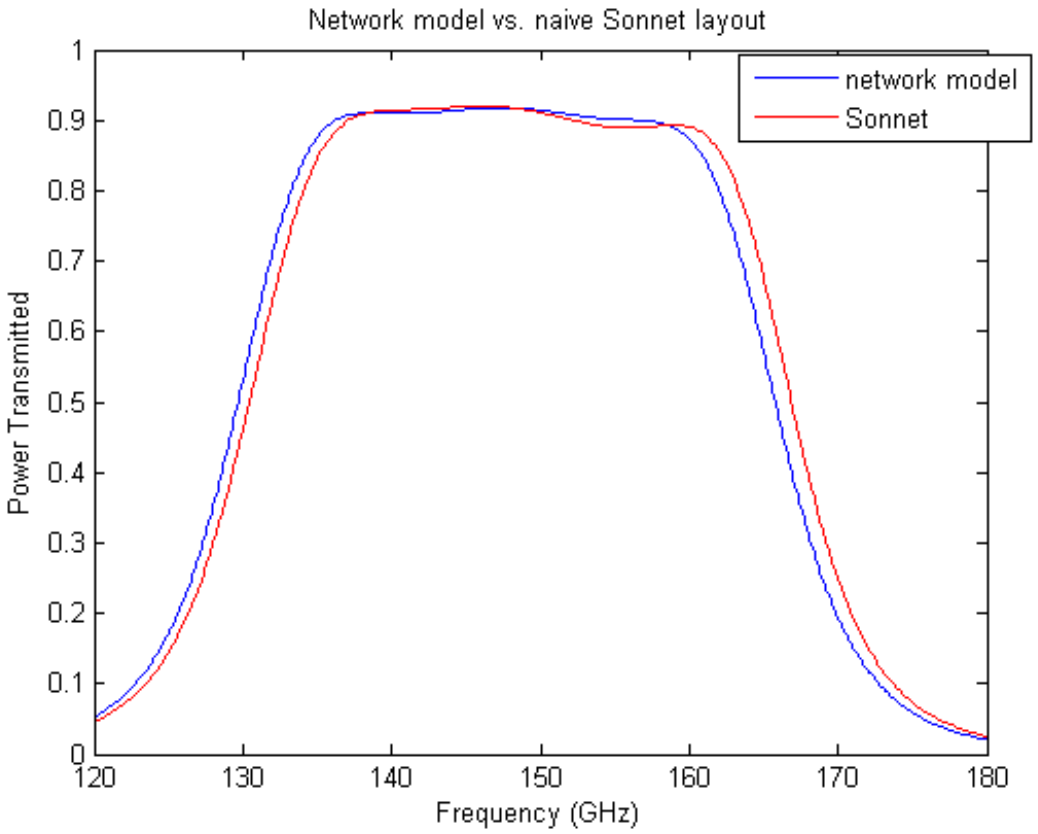

Figure 5.8: Comparison of the network model of the microstrip filter with a Sonnet full-wave simulation of the same structure.

$$\Delta f_{et} = (\mathcal{L} + 1)\,\frac{g}{\pi C}. \tag{5.2}$$

Whatever the electrothermal bandwidth, the readout bandwidth for that bolometer must be larger by a factor of ~ 5 [62]. The limited readout bandwidth available can best be used multiplexing several bolometers, each with only the necessary electrothermal bandwidth, rather than fewer bolometers, each with an unnecessarily large detector electrothermal bandwidth. As discussed in section 2.5, the scanning speed of the telescope limits the bandwidth over which there is useful astrophysical signal to $\sim 10^2$ Hz. Since g is set by the bolometer properties and the desired operating power, C is controlled in fabrication to achieve the desired Δf_{et} at reasonable $\mathcal{L}$.

C is controlled by depositing gold on the bolometer that is in good thermal contact with the thermistor [63]. Figure 5.9 shows a design drawing of the bolometer, with several components on the bolometer labelled. The thermistor material extends underneath the gold, and the gold extends onto the thermistor leads, so as to make

the best thermal contact possible without strongly affecting current flow across the thermistor.

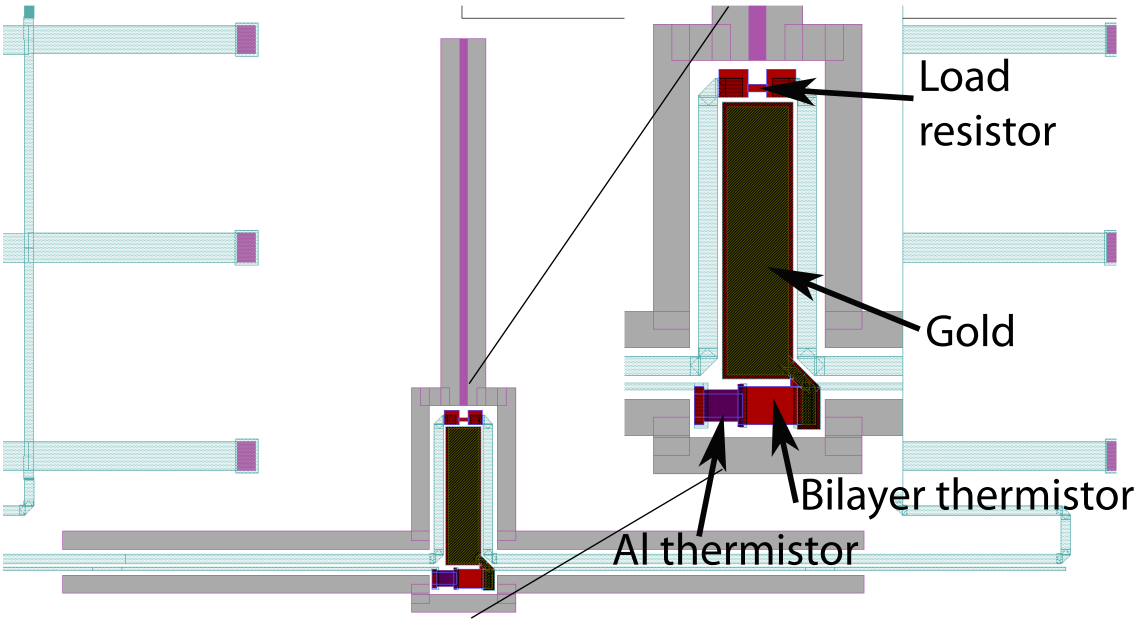

Figure 5.9: Design drawing of the POLARBEAR bolometer, showing in detail the central bolometer island with the dual thermistors, the gold to add heat capacity, and the load resistor onto which the radiative power is deposited.

Load resistor

The optimal load resistor for absorbing power from two balanced 10 Ω microstrip lines has a real impedance of 20 Ω and no imaginary impedance, creating a virtual ground in the center of the load resistor. For ease of fabrication, the aluminum/titanium bilayer used for the TES thermistor is also the metal used for the load resistor. Although the Al/Ti is going through its superconducting transition at about the bolometer temperature, the 150 GHz photon energy is larger than the energy gap of the superconductor, so the Al/Ti is resistive at these frequencies. However, the Al/Ti has a normal resistance of $\sim 1\ \Omega/\square$, which would mean that the load resistor would have to be 20 squares long. Given the distance to the ground plane, this structure would have significant inductance, and that inductance would cause power to be reflected away from the load resistor. There are two ways to address this: one is to reduce the inductance per square of the structure by moving it closer to the ground plane; the other is to use a higher resistance film so that the structure can be fewer squares long. It turns out that etching the Al layer out from underneath the

Al/Ti bilayer produces a Ti-only film that has a higher resistivity, $\sim 10\ \Omega/\square$. This allows fabrication of a load resistor with negligible inductance. Although there was some concern that this would inhibit thermal flow between the load resistor and the bolometer itself, there is not another apparent path for the heat to follow, and there is no evidence that the thermal connection of the load resistor to the bolometer is compromised.

5.1.6 Dual-TES thermistors

The POLARBEAR bolometers employ a dual-TES thermistor [64] to allow for two modes of observation: a low noise science-quality mode and a higher noise mode with larger dynamic range. The low noise mode uses an aluminum/titanium bilayer thermistor with a transition temperature of $T_{c,bilayer} \approx 0.5$ K, while the mode with larger dynamic range employs a bare aluminum thermistor with a transition temperature of $T_{c,Al} = 1.4$ K.

The design of the bilayer thermistor is somewhat independent of the Al thermistor. When operating the bolometer with the bilayer thermistor, the Al thermistor is simply a part of the superconducting thermistor leads. The bilayer thermistor operating resistance is $\sim 1\ \Omega$, which provides the bolometer responsivity necessary and couples correctly to the readout system.

The relationship between the operating power for the two transitions can be predicted using equation 3.14:

$$\frac{P_{Al}}{P_{bilayer}} = \frac{T_{c,Al}^{n+1} - T_b^{n+1}}{T_{c,bilayer}^{n+1} - T_b^{n+1}}, \tag{5.3}$$

which for $n = 3$ and $T_b = 0.25$, evaluates to a power ratio of 65. Given that the bilayer transition will be tuned to measure a radiative signal of brightness temperature $\sim 30\ \mathrm{K}_{RJ}$, the Al TES will have more than enough dynamic range to observe signals from a brightness temperature of $300\mathrm{K}_{RJ}$.

When operating using the Al TES, the bilayer thermistor is a series normal resistance. To achieve high electrothermal loop gain, the resistance of the Al TES should be larger than this series resistance. Exactly how much larger is a parameter to be optimized.

Electrothermal bandwidth

The bolometer's fundamental electrothermal bandwidth $\Delta f_{et} = \frac{g}{\pi C}$ is proportional to the small signal thermal conductance, $g \propto T_c^n$, and inversely proportional to $C \propto T_c$, so

$$\frac{\Delta f_{et,Al}}{\Delta f_{et,bilayer}} = \left(\frac{T_{c,Al}}{T_{c,bilayer}}\right)^{n-1}. \tag{5.4}$$

This comparison does not include the effect of loop gain on the electrothermal bandwidth. To some extent, the upper transition can be operated at a different loop gain to provide control of the electrothermal bandwidth.

Stability of the upper transition

If the Al thermistor has higher resistance than the normal bilayer thermistor, stable operation of the TES bolometer in the Al transition should be possible. Any transitioning thermistor R_t can be understood to first order as a series combination of a transitioning resistor and a normal resistor.

Assume that the bolometer has a thermistor of resistance R_t in series with a series resistor of resistance R_s. The series resistance always stays normal, while the thermistor transitions from the normal to the superconducting state. A voltage bias V_b is put across the series combination of R_s and R_t so that the current through the resistors is

$$I = \frac{V_b}{R_s + R_t}. \tag{5.5}$$

The electrical power being deposited on the bolometer is then

$$P = I^2 R_t + I^2 R_s = \left(\frac{V_b}{R_s + R_t}\right)^2 (R_t + R_s) = \frac{V_b^2}{R_t + R_s}. \tag{5.6}$$

This is clearly just the power across the sum of the two resistors. A standard bolometer with small series resistance is in the limit of $R_s \ll R_t$, so the above equation becomes

$$P = \frac{V_b^2}{R_t(1 + R_s/R_t)} \approx \frac{V_b^2}{R_t}(1 - R_s/R_t) = \frac{V_b^2}{R_t} - \frac{V_b^2 R_s}{R_t^2}. \tag{5.7}$$

The first term is the standard equation for electrical power on a bolometer, and shows that the feedback is negative: when the resistance R_t decreases, the power increases. The second term is correct to first order in R_s/R_t, and by assumption is smaller than the first.

In the other limit where $R_t \ll R_s$:

$$P = \frac{V_b^2}{R_s(1 + R_t/R_s)} \approx \frac{V_b^2}{R_s}(1 - R_t/R_s) = \frac{V_b^2}{R_s} - \frac{V_b^2 R_t}{R_s^2}. \tag{5.8}$$

Note the sign of the term linear in R_t. It is negative, so the feedback is still negative, although the strength of the feedback is decreasing as R_t decreases.

5.2 Focal plane array fabrication

As shown in figure 5.1, a single sub-array consists of a hexagonal device wafer of antenna-coupled bolometers on one side, with its other side in contact with a hexagonal array of lenslets. This section describes the fabrication of both of these units.

5.2.1 Lenslet sub-array

The lenslets are produced from semiconductor-grade single-crystal silicon. They are ground into spheres[1] and then ground flat along a plane intersecting a great circle of the sphere. This leaves a hemisphere to be integrated with the antenna as described in section 5.1.1.

The lenslet wafer acts as both part of the extension length providing the synthesized elliptical lenslet shape, and an alignment wafer to properly center each lenslet on its associated crossed double-slot dipole. Circles of diameter slightly (~ 40 μm) larger than the diameter of the lenslets are etched into the lenslet wafer using a deep reactive ion etching process [65]. Figure 5.10**(a)** shows the entire hexagonal array of these alignment recesses, and figure 5.10**(b)** shows a scanning electron micrograph of the steep sidewalls produced by the etch. These sidewalls act to locate each lenslet to within $\sim \lambda_0/100$. The entire lenslet wafer is then optically aligned to the device wafer using transmission infrared microscopy.

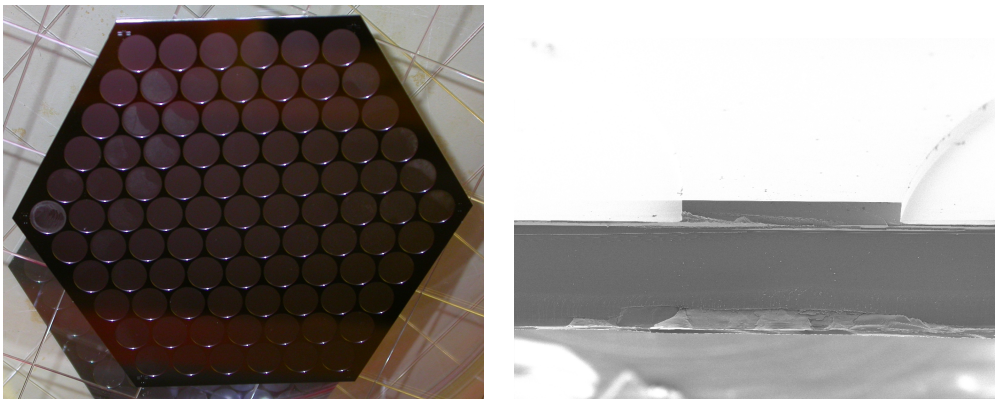

(a) **(b)**

Figure 5.10: **(a)** Lenslet sub-array before adhesion of the hemispherical silicon lenslets. The recesses in the wafer correctly locate the hemispherical silicon lenslets. The alignment accuracy is about 20 microns, or $\lambda_0/100$. **(b)** A scanning electron micrograph of one of the sidewalls of the lenslet-locating recesses.

[1] The commercial process of grinding into spheres is done by Rayotek Scientific, Inc.

5.2.2 Device wafer

Material	Thickness (microns)	Deposition Process	Etch Process
Silicon Substrate	500	Prime-grade wafers	XeF_2 vapor
Silicon Dioxide	0.05	Thermal growth	CF_4 RIE
Low Stress Nitride	0.7	LPCVD	CF_4 RIE
Niobium	0.3	DC Magnetron Sputter	CF_4 / O_2 RIE
Silicon Dioxide	0.3	350^0C PECVD	CHF_3 / O_2 RIE
Niobium	0.3	DC Magnetron Sputter	CF_4 / O_2 RIE
Silicon Dioxide	0.5	350^0C PECVD	CHF_3 / O_2 RIE
Niobium	0.6	DC Magnetron Sputter	CF_4 / O_2 RIE
Aluminum/Titanium Bilayer	0.04/0.12	DC Magnetron Sputter	Premixed wet etch / SF_6 RIE
Gold	1.5	Evaporation	Liftoff in acetone

Table 5.1: Layers in the POLARBEAR device wafer, along with thickness, deposition process, and etching process. Acronyms used in the table: RIE: Reactive Ion Etch; CVD: Chemical Vapor Deposition; PECVD: Plasma-enhanced CVD; LPCVD: Low-Pressure CVD.

The POLARBEAR device wafers require an eight layer process on a silicon substrate. The process is outlined in table 5.1, in order of layer deposition. The etching process for each layer is given; the etches for the layer are not in order, because they do not all occur immediately after deposition.

Substrate

The silicon substrate forms part of the dielectric contacting lenslet, so its microwave loss properties are important. A Fourier-transform spectrometer was used

to measure loss in commercial semiconductor-grade silicon at the frequencies of interest. The upper bound for loss on this measurement was low enough that it was not a significant source of loss in the pixel. It is important to note that some silicon with a higher impurity content did have significant loss and was unacceptable for this application.

Photoresist coating and patterning

Patterning is done in standard positive photoresist with a thickness of 1–4 microns, with the exact recipe depending on the process step. Patterning of the individual pixels is accomplished using a step and repeat 10X optical reduction printer, a GCA wafer stepper. Test pixels, wafer border, and alignment marks are also printed by the wafer stepper. The niobium thermistor leads, which transmit signals from the edge of the wafer to the thermistors, are patterned using a wafer-scale contact printer. After each patterning step, the photoresist undergoes a post-exposure bake and then an automated puddle develop. After development, the wafer is exposed to a 1 minute low-power oxygen plasma to remove any residual photoresist where the pattern was developed.

Microwave structures

The continuous niobium ground plane is broken only where necessary for the bolometer release and for the slots of the crossed double-slot dipole. Those slots are connected to superconducting microstrip waveguides that consist of a niobium ground plane, silicon dioxide dielectric, and niobium top conductor. The dielectric loss in the silicon dioxide is the primary source of loss in this superconducting microstrip transmission line [66].

The microwave structures, including the cross-under, are constructed of three layers of niobium and two layers of silicon dioxide. Notice that the silicon dioxide is not deposited in a furnace. This is important because high temperatures degrade the quality of the niobium as a superconductor [67]. Also notice that the thicknesses of the niobium ground plane and microstrip are 300 and 600 nm, respectively. At this thickness, both films are significantly thicker than the penetration depth [68], which reduces the dependence of the microstrip impedance on film thickness [69].

Bolometer structure

The TES thermistor is an aluminum/titanium bilayer. The layers of this bilayer must be deposited in direct succession without the wafer leaving the vacuum environment, and with an etch before the deposition to remove the native niobium oxide on the niobium thermistor leads. The gold bling that is used to increase the heat capacity of the bolometer is deposited using electron beam evaporation onto already patterned photoresist, so that the gold is removed everywhere other than where it is

desired by dissolving the photoresist in a lift-off procedure. The TES bolometer suspension structure is provided by the Low-stress Silicon Nitride (LSN) film deposited directly on the silicon wafer. This deposition is first, but the etching of the LSN occurs much later in the process, after all of the deposition steps are complete. To release the suspended TES structure, trenches are etched into the LSN, and then the silicon substrate underneath the LSN is removed by an isotropic gaseous xenon difluoride (XeF_2) etch. Figure 5.1**(d)** shows a scanning electron micrograph of a released bolometer. The rough surface below the bolometer is where the silicon has been etched by the XeF_2, leaving the suspended bolometer structure.

Chapter 6

Spectral Band Optimization

Many experiments have sought to utilize the atmospheric windows between 60 and 300 GHz to measure the CMB from the ground. Even within the atmospheric windows, emission of the relatively hot atmosphere will dominate the radiative load on the detectors of a well-designed experiment. The placement, width and shape of the detectors' spectral bands will determine the amount of radiative power from both the atmosphere and the CMB.

There are three factors to consider when deciding band placement and design:

1. **Signal/Noise**: The total optical power and photon noise on the detector depend on the spectral response, as does the amount of power received from the CMB. The NET_{cmb}, quoted here in $mK \cdot \sqrt{s}$, is the figure of merit for the SNR of the detectors. It is explained in section 3.7.

2. **Atmospheric anisotropy**: Temporal and spatial variations in the signal from the inhomogeneous atmosphere are not captured in the above figure of merit. While the O_2 density is constant on short (< 10 s) time scales, there can be significant variation in the integrated H_2O opacity visible to a single detector. This signal is unpolarized so it is common to both of the detectors of the same pixel, and thus is removed when calculating polarization. Since the atmospheric loading is spatially correlated across the array, it can also be understood and removed by correlating signals between nearby pixels.

3. **Astrophysical foregrounds**: The blackbody spectrum of the CMB is well known. Polarized astrophysical foregrounds will not have a blackbody spectrum, so information at several frequencies can help distinguish between the two.

This chapter only analyzes the first of these factors. The analysis is specific to the POLARBEAR microstrip filters, but the technique is generic in its applicability to this problem.

6.1 Atmospheric simulations

The AM atmospheric model [70] has a pre-defined recipe for the Chajnantor Plateau that is used to calculate the atmospheric opacity for the Chilean site. 1 mm precipitable water vapor at the Chajnantor Plateau corresponds to the median observing conditions [26]. For the Cedar Flat site, a mid-latitude recipe was augmented to reflect the air pressure from the US Standard Atmosphere at the Cedar Flat elevation, 2.2 km [71][1]. The integrated precipitable water vapor in this recipe was varied to give a zenith opacity at 225 GHz, $\tau_{225,z}$, of 0.275, which is a slightly higher opacity than the median reported for this site for the best 10 months of the year [72]. The simulated opacity within the frequency range of interest was insensitive to exactly how the mid-latitude recipe augmentation was done. Figure 6.1 shows the simulated atmospheric transmittance and sky brightness temperature at the two sites.

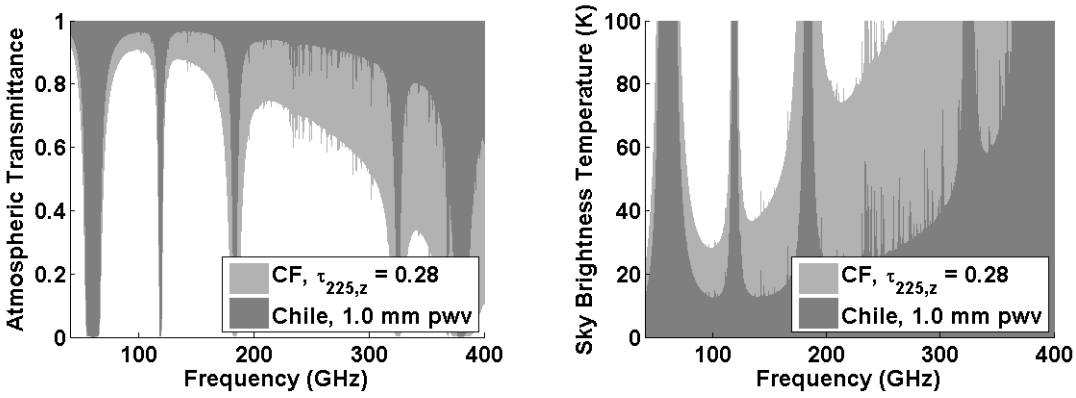

Figure 6.1: Atmospheric simulations for both of the POLARBEAR sites, the lighter shading for Cedar Flat and the darker shading for the Chilean site. **(a)** shows atmospheric transmittance and **(b)** shows sky brightness temperature in K_{RJ} for an observation angle 30° from zenith.

6.2 Filter design parameters

A network model for the distributed microstrip filter, including loss, is used within this optimization. This network model adjusts the band center, width, and number of poles. Three pole, five pole, and idealized top-hat filters are considered to illuminate

[1] Atmospheric calculator at http://www.digitaldutch.com/atmoscalc/

the effect of band-edge steepness. In interpreting the results, it is useful to understand a few generic properties of the filters [66]:

- Steepness of band edges increases with an increased number of poles
- maximum in-band efficiency increases with increasing bandwidth
- maximum in-band efficiency increases with a decreased number of poles

6.3 Cryostat fractional throughput

To understand the optical power on the detector, it is useful to analyze the system in transmission, with the bolometer is emitting 100% of its radiation, and that radiation being partially scattered or absorbed by elements between the bolometer and the CMB. The fraction of the radiation absorbed or scattered at an element, and the temperature at which that radiation terminates, dictate the power that the bolometer receives from that element.

Table 6.1 shows the elements in the optical path that were considered when calculating the optimal band, the percent absorption or scattering at each of these elements, and the temperature of the element. A more realistic version of this table, adjusted after the engineering run, is shown in table 7.1.

6.4 Filter band optimization

Optimization of the bandwidth, center frequency, and number of filter poles was carried out for bands in the atmospheric windows around 90, 150, and 250 GHz. Sections 6.4.1–6.4.3 illustrate how different factors affect this optimization for the atmospheric window around 150 GHz. Section 6.4.4 concludes the chapter by showing the result of this optimization for the other two atmospheric windows.

6.4.1 Top-hat filter model, photon noise only

For a band of arbitrary shape $\eta(\nu)$, the integrated bandwidth $\Delta\nu_I$ is defined as

$$\Delta\nu_I = \frac{\int \eta(\nu) d\nu}{max(\eta(\nu))}. \tag{6.1}$$

To describe the bandwidth optimization first without reference to the specifics of the microstrip filters, this section considers a top-hat band with unity throughput in a band of width $\Delta\nu$ centered on frequency ν_0, with zero throughput outside of the band. Note that for the top-hat band, $\Delta\nu_I = \Delta\nu$. Bandwidths will usually be referred to as fractional bandwidths, the bandwidth divided by the center frequency.

Element	Termination temperature	Loss or Reflection	Cumulative fractional throughput (element to bolometer)	T_{RJ} referred to primary mirror
Load resistor mismatch	0.5	0.0%	1.00	0.00
Microstrip filter*	0.275	10.0%	1.00	0.00
Antenna mismatch	0.275	0.0%	0.90	0.00
Antenna backlobe	0.275	9.0%	0.90	0.00
Lenslet surface reflection	0.275	20.0%	0.82	0.00
Focal plane filters	0.275	2.0%	0.66	0.00
Collimating lens	6	2.0%	0.64	0.08
Aperture lens	6	2.0%	0.63	0.08
Aperture stop truncation**	6	11.0%	0.62	0.43
Aperture filters	6	0.0%	0.55	0.00
field lens	6	2.0%	0.55	0.07
4K filters	6	3.0%	0.54	0.10
50K filters	50	3.0%	0.52	1.48
300K filters	300	2.0%	0.51	6.11
300K Zote Foam	300	1.0%	0.50	2.99
Secondary scattering	200	0.0%	0.49	0.00
Primary scattering	200	0.0%	0.49	0.00
To atmosphere:			**0.49**	**11.35**
Total cumulative fractional throughput divided by aperture stop fractional throughput:			**0.50**	

Table 6.1: Table of the elements in the POLARBEAR optical path that cause absorption or scattering of the detector beam. This is the table of elements used when optimizing the spectral band of the detectors. A more complete table reflecting knowledge gained in the engineering run is shown in table 7.1. *The loss in the microstrip filter depends on the filter design, as described in section 6.3, and **the absorption at the aperture stop (the spatial truncation of the beam) depends on the pixel size, as described in chapter 4.

Figure 6.2 shows the NET_{cmb}, only accounting for photon noise, for the 150 GHz band as a function of center frequency and bandwidth. The optimal filter is the local minimum in NET_{cmb}. Due to fabrication variability, the center frequency of the filter can shift. For this reason, it is preferable to pick the center frequency and bandwidth that maintains the smallest possible NET_{cmb} over the range of variability of the center frequency. For the purpose of this analysis, this variability is taken to be $\pm 5\%$.

6.4.2 Real filter model, photon noise only

Because the real filter does not have band edges as sharp as the top-hat filter, the constraints in the contour plot are not as strong. Figure 6.3 shows the plots for microstrip filters with five and three poles. The three pole filter is the one chosen for the POLARBEAR pixel because it is more forgiving to variability in center frequency.

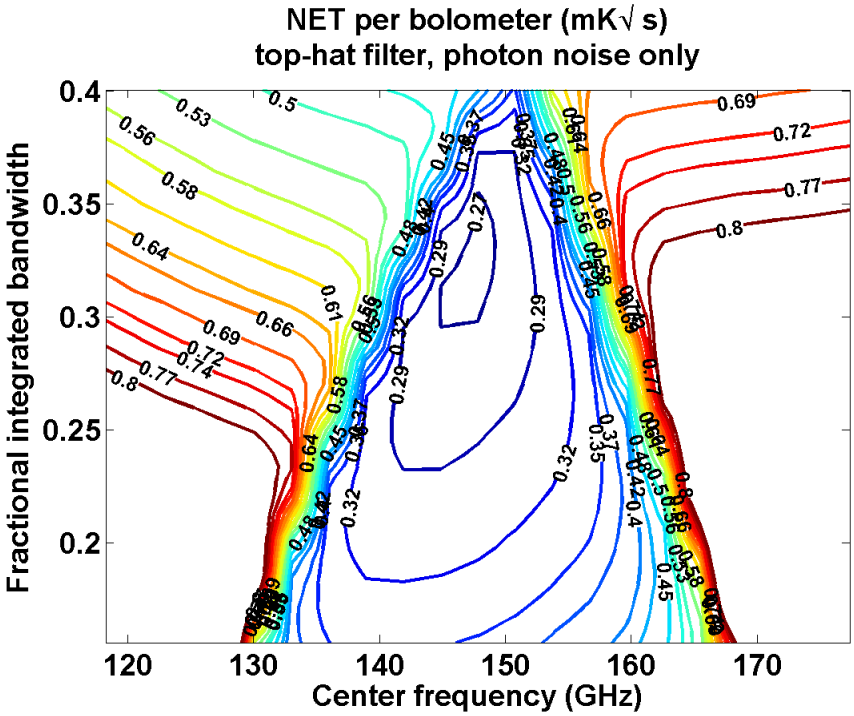

Figure 6.2: $\mathrm{NET}_{cmb,\gamma}$ per bolometer (photon noise only) for a top-hat band, as a function of the center frequency and fractional bandwidth of the microstrip filter. Atmospheric simulation is for the Chilean site with 1 mm precipitable water vapor, observing at 30° zenith angle.

The slightly lower minimum NET_{cmb} for the five pole filter suggests that filter would be better if the fabrication variability in the center frequency were $< 1\%$.

6.4.3 Real filter model, all noise sources

Each pair of bandwidth and center frequency corresponds to an expected optical power on the bolometer. Given a design ratio of electrical to optical power, this sets the design operating power for the bolometer. The bolometer bath temperature (0.25 K) and transition temperature (taken here to be 0.45 K) are set, and a thermal carrier noise equivalent power NEP_g is calculated for each possible spectral band. For these calculations, the electrical power is always 1.5 times the optical power.

Also, the readout system introduces some noise. The two dominant readout noise sources are the input current noise of the SQUID and the voltage noise in the first warm amplifier. All of the readout noise together is approximately 7 $\mathrm{pA}/\sqrt{\mathrm{Hz}}$. Given the bolometer resistance during operation (set here to be 1.0 Ω), these noise sources

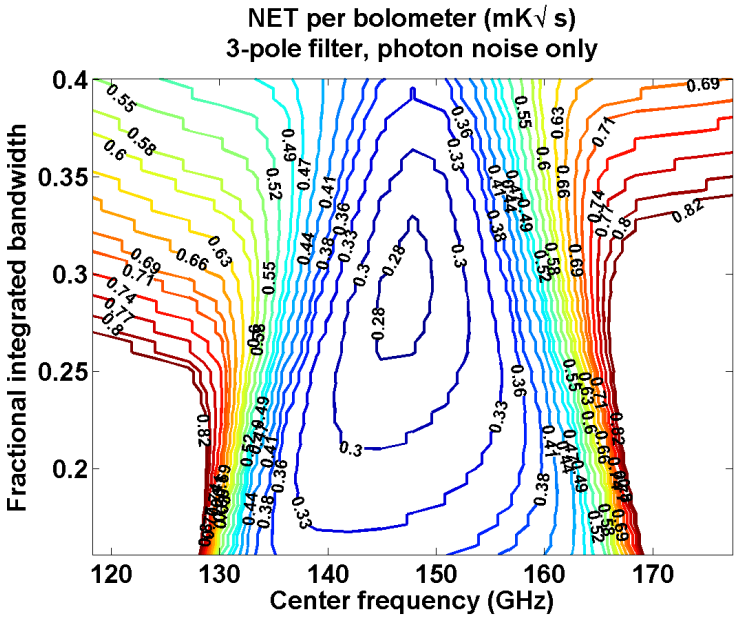

(a)

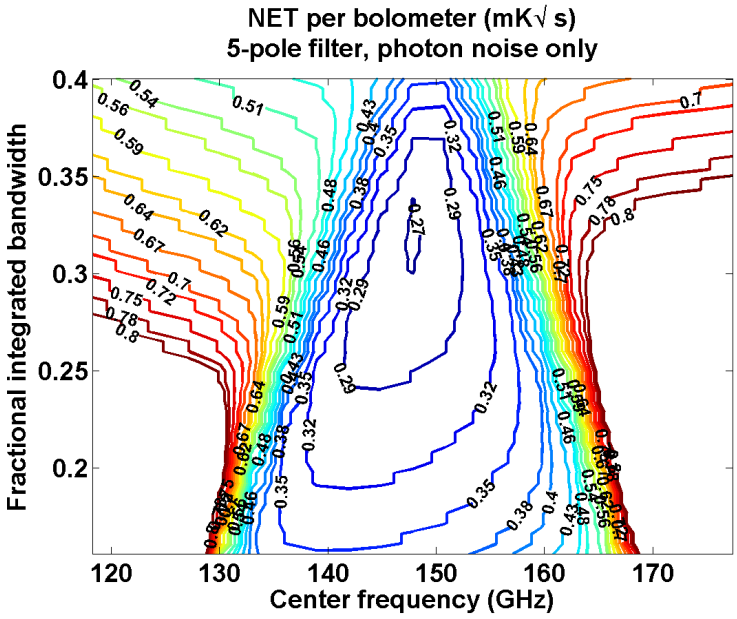

(b)

Figure 6.3: $\mathrm{NET}_{cmb,\gamma}$ per bolometer (photon noise only) for an **(a)** three and **(b)** five pole filter, as a function of the center frequency and fractional bandwidth of the microstrip filter. This is the same as in figure 6.2, but with a realistic rather than a top-hat filter model. Atmospheric simulation is for the Chilean site with 1 mm of precipitable water vapor, observing at 30° zenith angle.

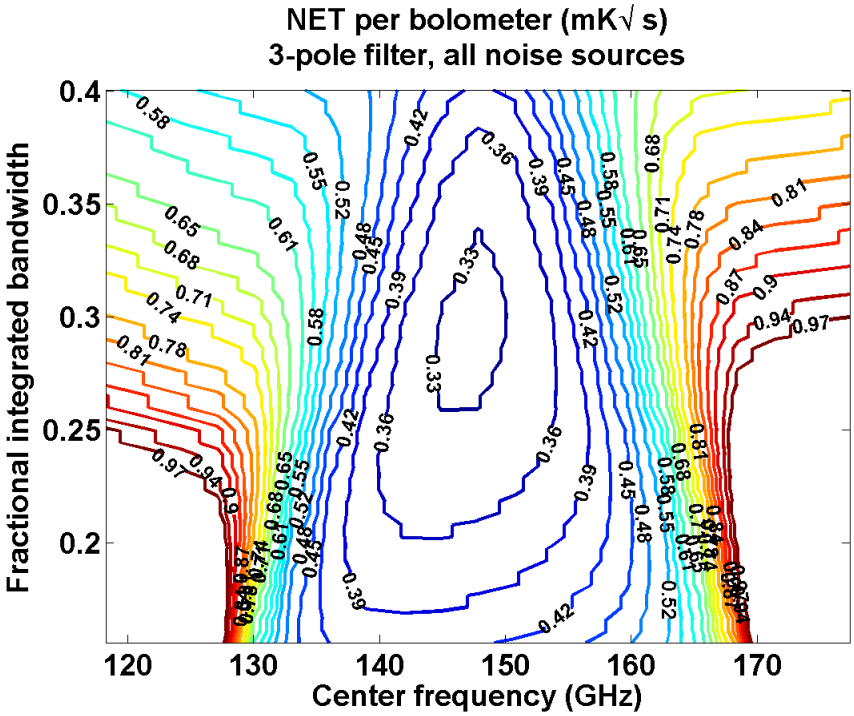

Figure 6.4: NET_{cmb} per bolometer (all noise sources) for a three-pole filter, as a function of the center frequency and fractional bandwidth of the microstrip filter. This is the same as figure 6.3(**a**), but the detector and readout noise is included. Atmospheric simulation is for the Chilean site with 1 mm of precipitable water vapor, 30° zenith angle.

can be referred back to the input of the bolometer as $\mathrm{NEP}_{readout}$, or to the sky as $\mathrm{NET}_{cmb,readout}$.

Figure 6.4 shows the NET_{cmb} contours for a three-pole filter design, including these noise sources. Both NEP_g and $\mathrm{NEP}_{readout}$ are proportional to the square root of the bolometer operating power P_{oper}. Since NEP_γ includes the photon bunching term described in section 3.4, it is more strongly dependent on P_{oper}. For this reason, the contours around the optimal filter band are less steep when considering all noise sources.

Figure 6.5 is the same as figure 6.4, focusing on the neighborhood of the local minimum, and using grid lines to guide the eye. From this figure, the optimal center frequency and bandwidth would be 147 GHz, with a fractional bandwidth of 0.29. However, a lower fractional bandwidth allows for greater variation in center frequency without $\mathrm{NET}_{cmb} > 0.36$ mK$\sqrt{\mathrm{s}}$. The POLARBEAR design spectral band was chosen to be centered at 147.8 GHz with fractional integrated bandwidth of 0.26.

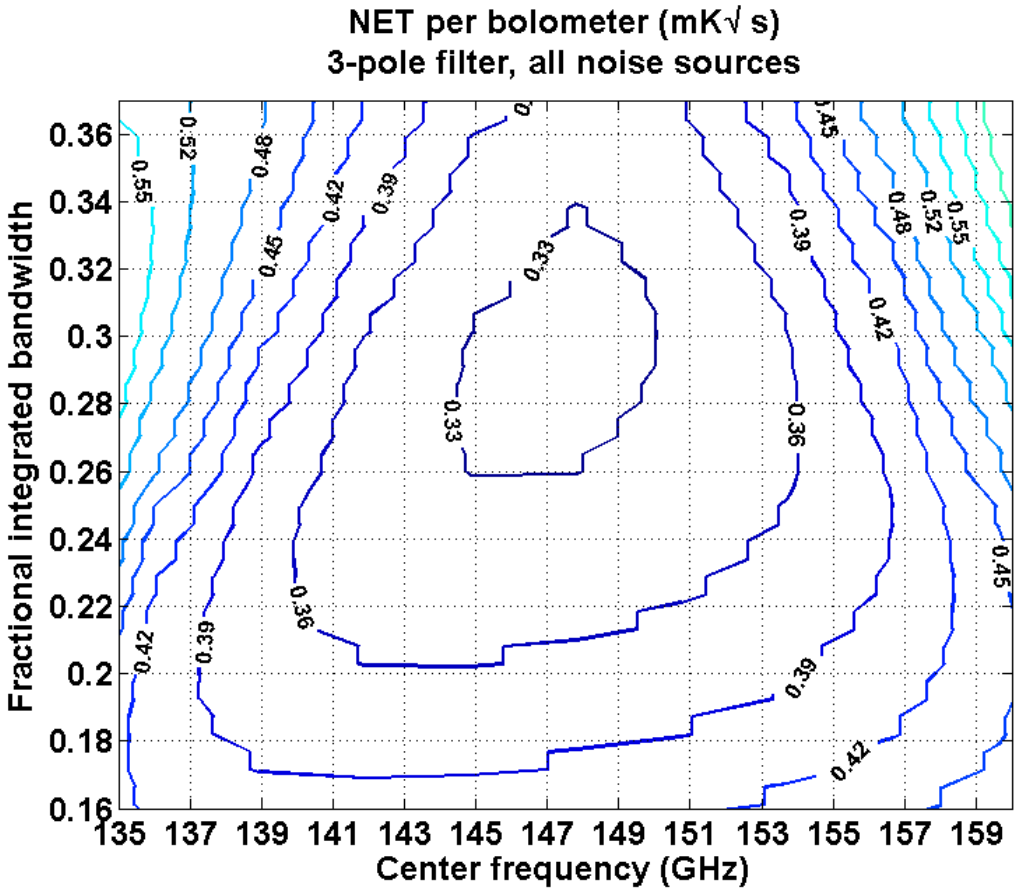

Figure 6.5: Same as figure 6.4, with the desirable region in parameter-space magnified to illustrate the band parameter selection technique. The band parameters that allow for ±5% variation in center frequency while retaining low NET_{cmb} are a center frequency of 147.8 GHz and 0.26 fractional bandwidth. Atmospheric simulation is for the Chilean site with 1 mm precipitable water vapor, observing at 30° zenith angle.

6.4.4 Real filter model, all noise sources, 90 & 250 GHz atmospheric windows

For completeness, figure 6.6 shows the contour plots analogous to figure 6.4 for the atmospheric windows around 90 and 250 GHz.

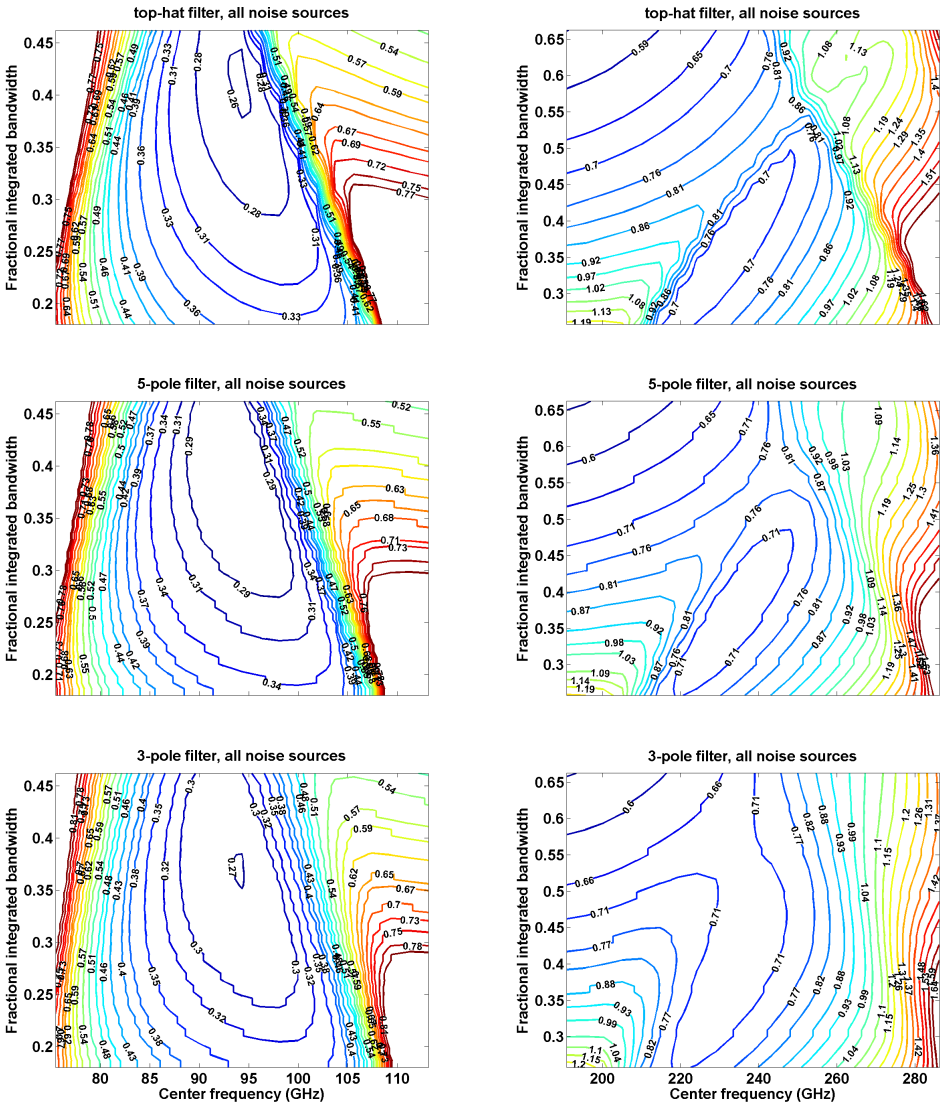

Figure 6.6: NET_{cmb} per bolometer for top-hat, three pole, and five pole filters, including all noise sources (assuming $P_{bias} = 1.5 \cdot P_{opt}$), for the atmospheric windows around 90 GHz (left) and 250 GHz (right). Atmospheric simulation is for the Chilean site with 1 mm precipitable water vapor, 30° zenith angle.

Chapter 7

Instrument Engineering Results and Future Tests

In early 2010, the cryogenic receiver was assembled with a focal plane consisting of three sub-arrays, and was mounted on the Huan Tran Telescope (HTT) at the Cedar Flat site in Eastern California. Figure 7.1**(a)** shows a picture of the focal plane in this configuration, and figure 7.1**(b)** shows one of the sub-arrays and its associated readout hardware. Note that two of the sub-arrays used low cost alumina lenslets and one used the observation-quality single-crystal silicon lenslets that will be used in the Chilean deployment. Also, the Cedar Flat configuration included a cooled attenuating filter in the optical path at a temperature of 6 K to reduce the optical power on the detectors from the relatively opaque atmosphere.

7.1 Bolometer operation

The POLARBEAR dual-TES bolometers each have two superconducting transitions (see section 5.1.6). Measurements of the resistance as a function of temperature for a dual-TES thermistor that had not been thermally released from the substrate are shown in figure 7.2.

A standard test of a bolometer's electrothermal response is to measure the current through the thermistor as the voltage across the thermistor (V_{bias}) is varied. Figure 7.3 shows data from this experiment for one of the POLARBEAR bolometers (using a device from the same wafer as the thermistor for which data are shown in figure 7.2). These data were collected using a non-multiplexed DC biasing system[1], with no optical power on the bolometer. Note the two regions where the derivative dP_{bias}/dV_{bias} is very small. This is the hallmark of strong electrothermal feedback: the changing resistance as a function of temperature causes the power on the bolometer to be constant [40]. These two regions correspond to the two superconducting transitions.

[1]The DC biasing system uses a commercial Quantum Design DC SQUID ammeter

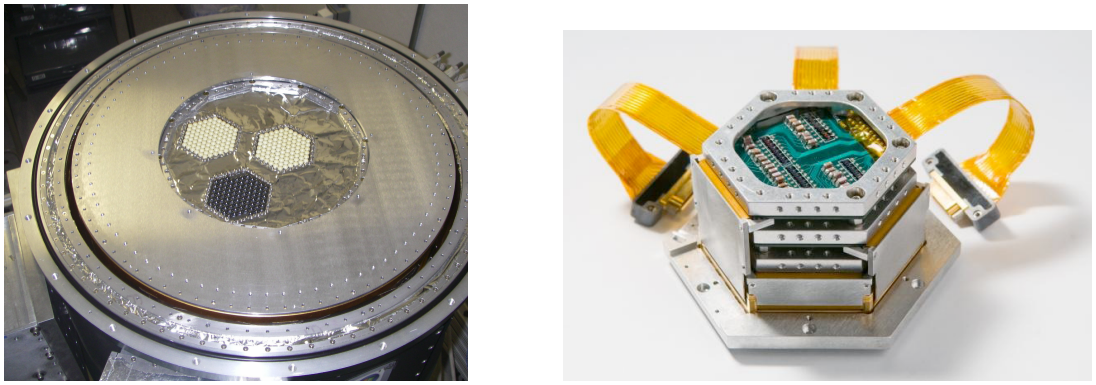

Figure 7.1: **(a)** Picture of the focal plane as it was deployed to Cedar Flat in early 2010. The white lenslets are alumina lenslets that were used for the early arrays because of their low cost. The darker lenslets are the observation-quality single-crystal silicon lenslets. All the lenslets are anti-reflection coated with thermoformed polyetherimide. For the Chilean deployment, the focal plane will consist of seven sub-arrays, all close-packed. **(b)**Picture of one of the sub-array modules, from the side that shows the frequency-domain multiplexed readout hardware. Note that the circuitry all fits behind the sub-array, to allow for close-packing of the sub-arrays in the actual experiment.

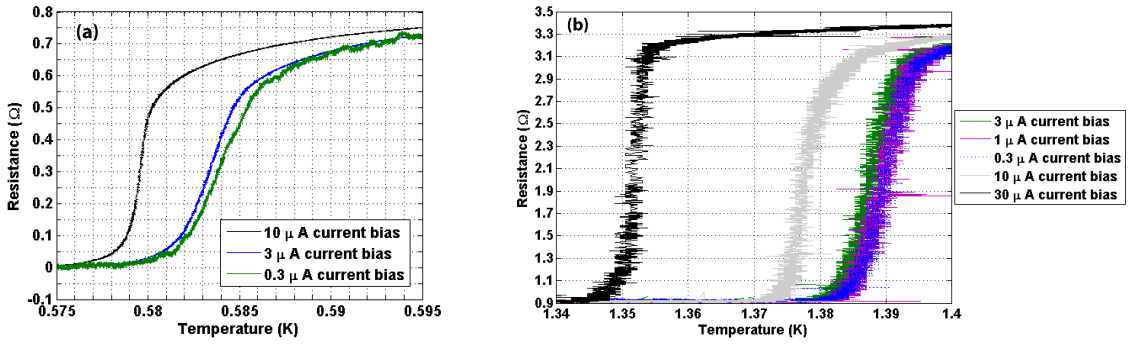

Figure 7.2: Superconducting transitions of the **(a)** aluminum/titanium bilayer and **(b)** aluminum thermistors. Data are from a thermistor that had not been thermally released from the substrate. For an operating bolometer, typical currents are 20–40 μA for the aluminum transition and 4–12 μA for the bilayer transition. Note that there is some change in resistance with current in this regime for both transitions. The horizontal scatter in the data is due to noise in the 4-point resistance measurement of the germanium resistance thermometer.

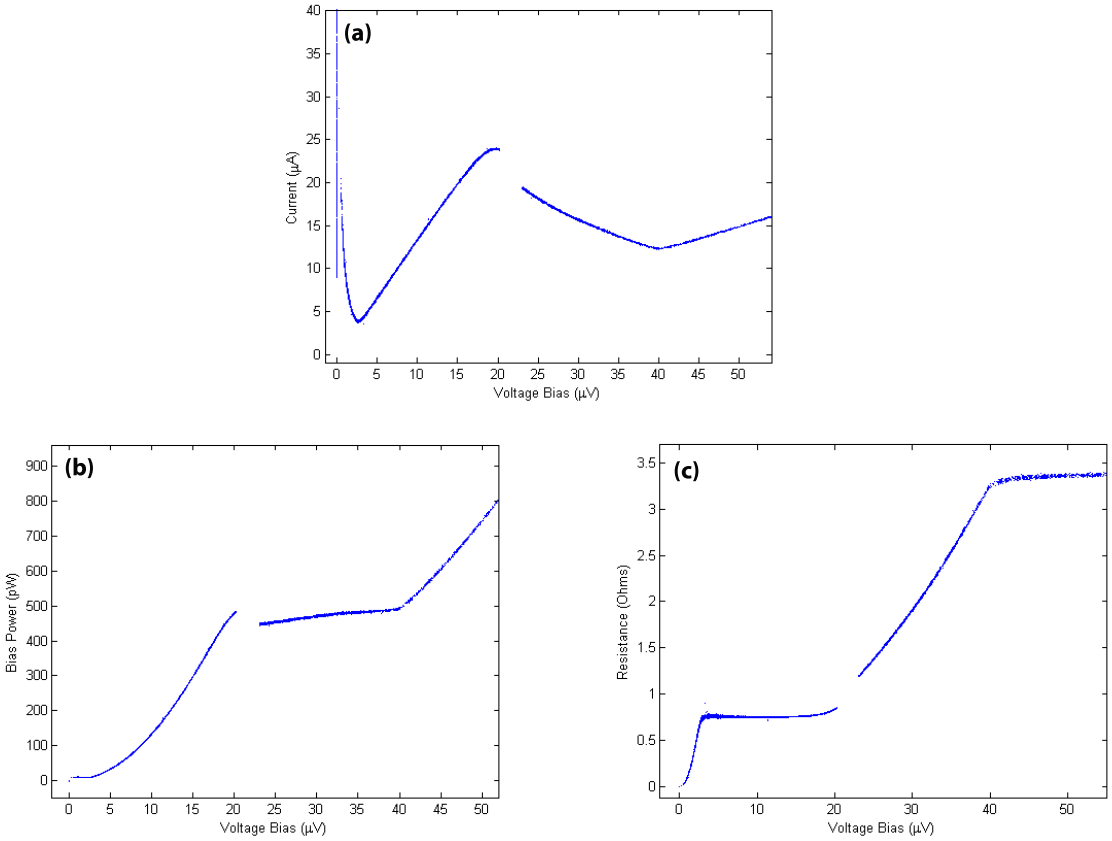

Figure 7.3: Electrothermal response of a Dual-TES bolometer from the same wafer as the transition temperature measurements shown in figure 7.2. The voltage bias is varied and the current through the bolometer measured using a DC SQUID ammeter. This is shown in **(a)**. Plots showing the calculated **(b)** power and **(c)** resistance as a function of voltage bias are also shown. There is no optical power incident on this bolometer.

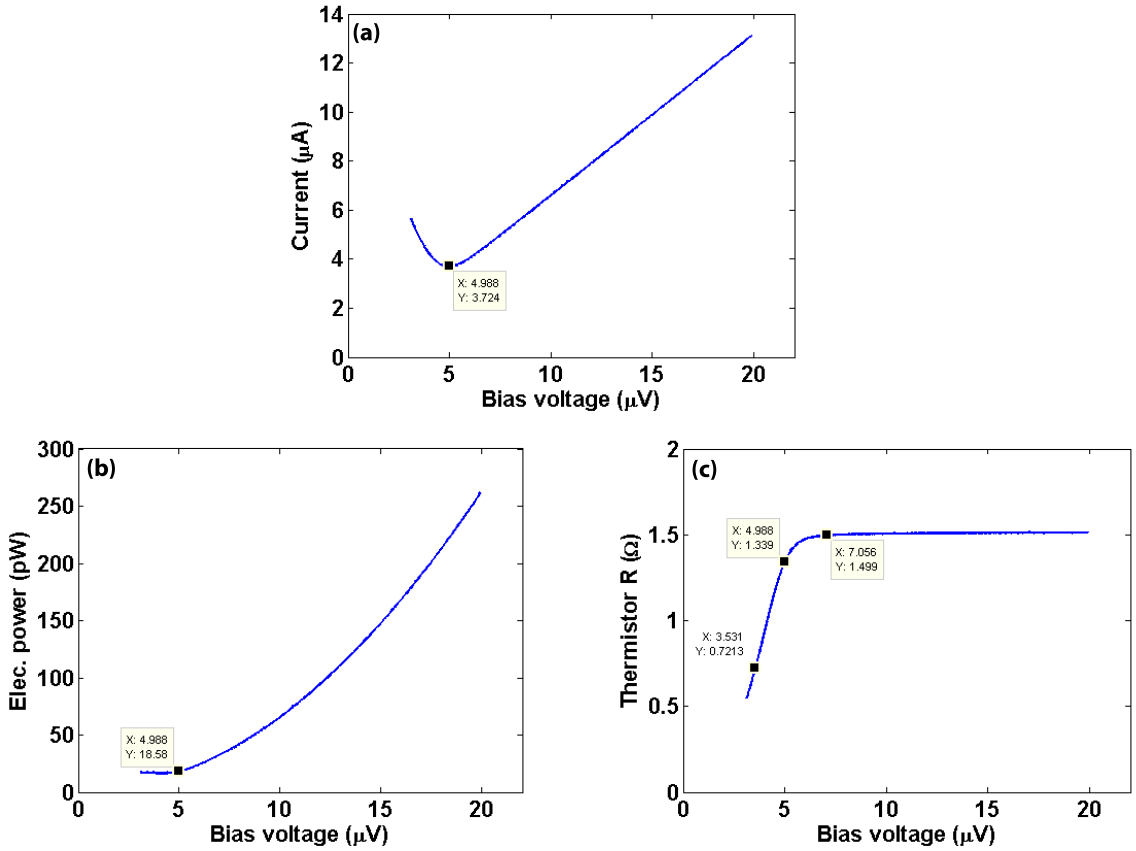

Figure 7.4: Electrothermal response of the bilayer TES bolometer with no optical power. This is a more recent device than that for which the data are shown in figure 7.3. The voltage bias is varied and the current through the bolometer is measured using a SQUID ammeter, shown in **(a)**. Plots showing the calculated **(b)** power and **(c)** resistance as a function of voltage bias are also shown. Markers show the $\mathcal{L} = 1$ point on all plots, as well as the points where the voltage bias is $\sqrt{2}$ higher and lower than this on the resistance versus voltage plot.

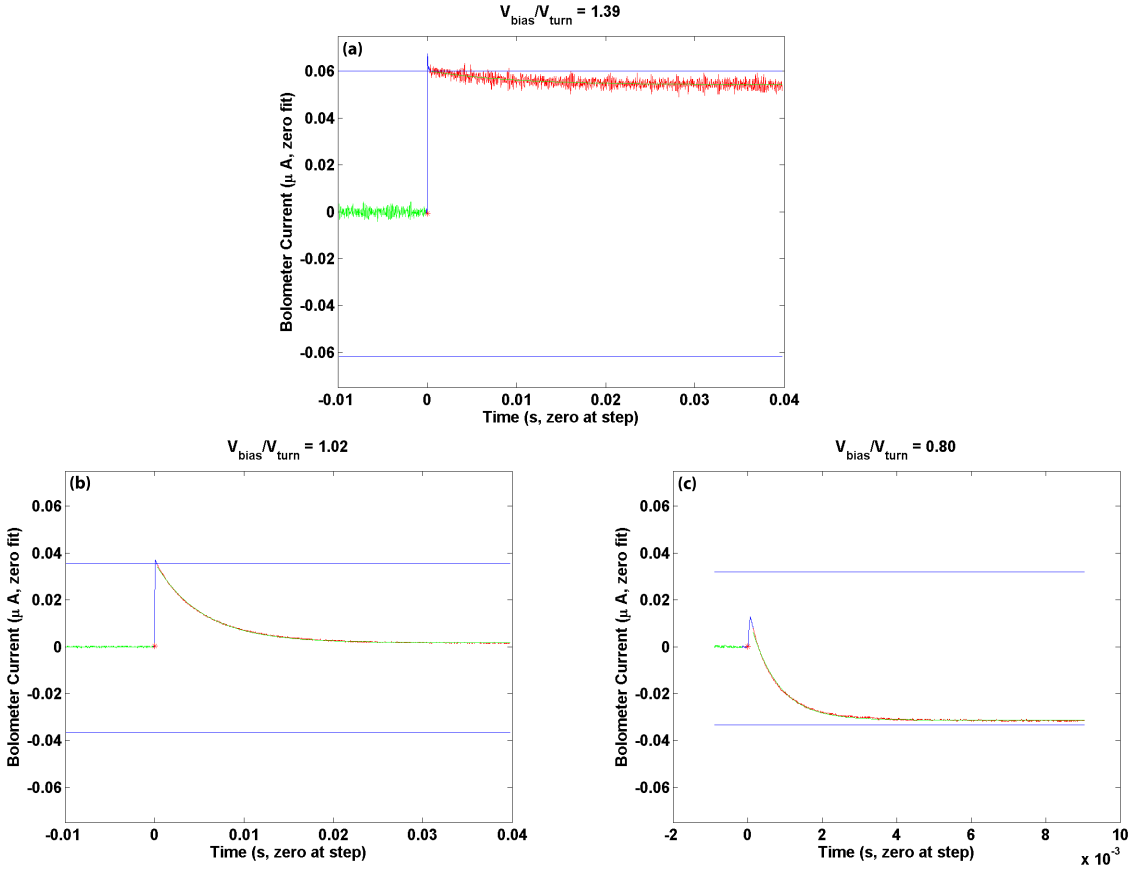

Figure 7.5: Small-signal electrothermal response of the bilayer TES bolometer to a small step in voltage bias for three different starting voltage biases: **(a)** well above the transition, **(b)** at the $\mathcal{L} = 1$ point where the dynamic resistance is infinite, and **(c)** in the strong electrothermal feedback limit where the power on the bolometer stays constant. In all cases, the upper blue line shows the perfectly Ohmic response, and the lower blue line shows the theoretical response in the limit of high electrothermal loop gain. These data are from the same device as those shown in figure 7.4.

Figure 7.4 shows data from the same type of experiment as figure 7.3, but for a different bolometer, and focusing on the bilayer transition. As the voltage bias decreases, the response to a small step in voltage bias changes from being approximately Ohmic (top right of the plots in figure 7.4, where $P_{bias} \propto V_{bias}^2$) to that of a bolometer with high electrothermal loop gain $\mathcal{L}$ (bottom left of the plots, where P_{bias} is constant). As this happens, the thermal response time of the bolometer to a change in V_{bias} (or incident power) decreases. Both of these effects are shown in figure 7.5, where the measured response (in current) to a small step in voltage bias dV_{bias} is plotted for different initial V_{bias}. These data, taken with the DC biasing system, show the electrothermal response in the time domain. The same characterization of the electrothermal response can be made in the Fourier domain with the frequency-domain multiplexing electronics [73].

Figure 7.6 shows the current noise, as referred to the input of the SQUID, of a single operating bolometer from a set of multiplexed bolometers. Note that the bolometer noise is flat and consistent with the expected value from 1 Hz to the roll-off at high frequencies that is imposed by the low-pass filtering in the multiplexed readout. The low-frequency noise here is likely dominated by thermal variations in the test cryostat, and is not fundamental to the bolometer.

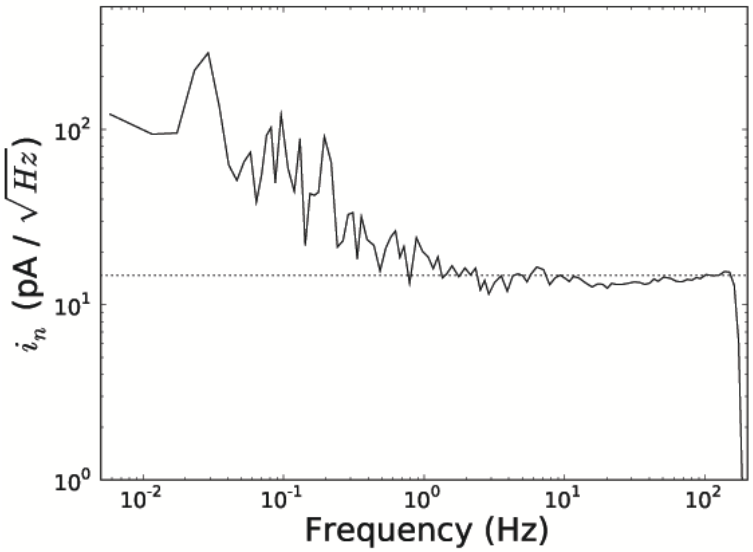

Figure 7.6: Amplitude spectral density noise spectrum for a POLARBEAR bolometer operating at 80% of its normal resistance. The dashed line shows the expected value. These data were recorded and analyzed by the POLARBEAR collaborators at McGill University.

7.2 Spatial sensitivity

The spatial sensitivity (beammap) of each of the detectors was measured in the laboratory before mounting the cryogenic receiver on the telescope. A thermal source 1.25 inches in diameter modulating between room and liquid nitrogen temperatures (by means of a room-temperature chopper wheel and a liquid nitrogen thermal source) was placed 2 inches in front of the cryostat window, with the rest of the cryostat window entirely blocked by room-temperature absorber. The aperture was stepped on a 1 inch square grid, and the bolometer signals at each step were recorded along with a reference signal for the aperture temperature modulation. This reference signal was then used to demodulate the bolometer response.

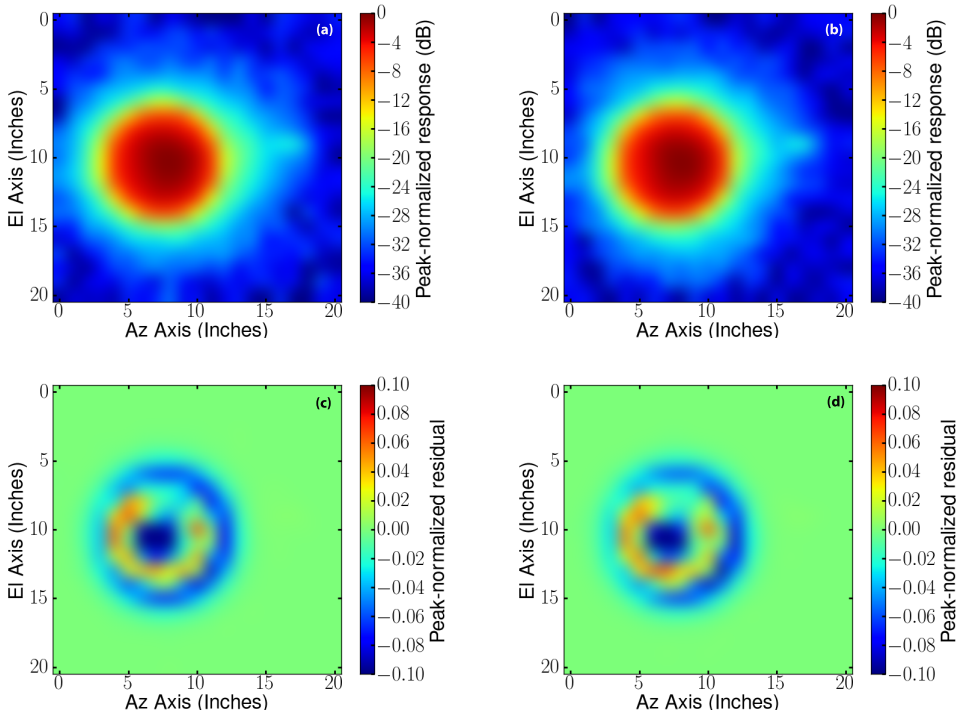

Figure 7.7: **(a)** and **(b)** show measurement of the spatial sensitivity of the two bolometers associated with one of the POLARBEAR pixels in the POLARBEAR observation cryostat. There is some broadening of both beams at -25 dB toward the center of the cryostat (to the right). This was common to all of the measurements of pixels on this side of the cryostat, and did not rotate with the polarization axis of the pixel or the bolometer. The cause of this feature is currently under investigation. **(c)** and **(d)** show the residual power in the beams after subtracting the best-fit circular Gaussian. Note that the non-Gaussianity is everywhere less than 10% of the beam's peak power

The position at which these beammap measurements were performed is neither an aperture plane nor a field plane of the optical system. From the ZEMAX geometric ray-optics model, the shadow of the absorbing aperture at the position of the beammap is 8.3 inches in diameter. The aperture stop is designed to truncate each pixel's beam at the -9 dB contour. Figure 7.7**(a-b)** shows some of the highest SNR beammap measurements for two polarizations of the same pixel. The circular Gaussian that best fits this data has a -10 dB beam diameter of just over 8.5 inches, consistent with the ZEMAX model. There is some structure in both of the beams that peaks at -25 dB and is located toward the center of the cryostat (to the right). This was common to all of the measurements of pixels on this side of the cryostat, and did not depend on the polarization axis of the pixel or the bolometer. The cause of this feature is currently under investigation.

Figure 7.7**(c-d)** shows the residual power in the beammaps from figure 7.7**(a-b)** after subtracting a best-fit circular Gaussian beam. The residuals are plotted as a fraction of peak response on a linear scale—note that the non-Gaussianity is everywhere less than 10% of the beam's peak power, and that on the linear scale the structure toward the center of the cryostat is not visible.

Mounting the receiver on the telescope provided astrophysical sources with which to test the spatial response of the detectors through the entire optical system. Figure 7.8 shows a map of Jupiter, co-added from about half of the bolometers in the focal plane. The θ_{FWHM} is consistent with the expected 3.4 arcminutes.

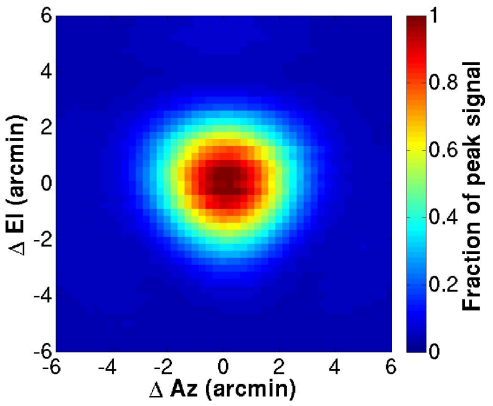

Figure 7.8: Measurement of the co-added spatial response of several of the detectors in the POLARBEAR focal plane using Jupiter as a source.

7.3 Polarization sensitivity

The Polarization sensitivity of these detectors has been measured under several different circumstances. In the lab, a polarized thermal load was created using the same type of aperture used in the beam measurement but with a wire-grid polarizer in between the aperture and the detector. In this configuration, the signal that the bolometer sees at the modulation frequency is polarized with the purity of the wire-grid polarizer. Figure 7.9 shows a measurement of the polarization sensitivity of a single pixel with such a polarized aperture on the boresight of the pixel, with only thermal filters between the pixel and the polarized source. The ratio of minimum to maximum response for the fit sinusoidal function is < 0.02, which is limited by the wire grid polarizer in the test setup.

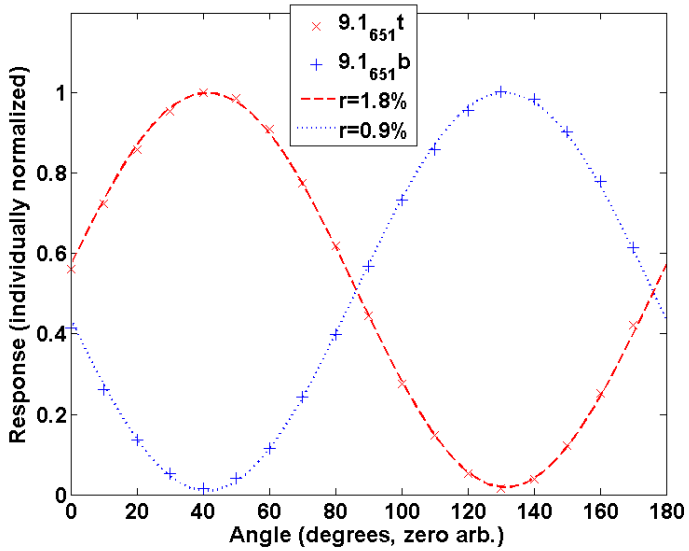

Figure 7.9: Measurement of the polarization sensitivity of a single pixel with a polarized aperture at the boresite of the optical response. This measurement was made in an optical test cryostat, with only thermal filters between the pixel and the polarized source. The fit is a sinusoid with an offset. The ratio of minimum to maximum response for the fit sinusoidal function is < 0.02 for both polarizations, which is near the limit of the polarization efficiency of the wire grid polarizer in the test setup.

Figure 7.10 is a plot of data from the same type of measurement in the POLARBEAR observation cryostat, for a single pixel, at two positions of the HWP, showing that the HWP is acting as a polarization modulator. Here the polarization efficiency is limited by the band-averaged efficiency with which the HWP transforms polarization.

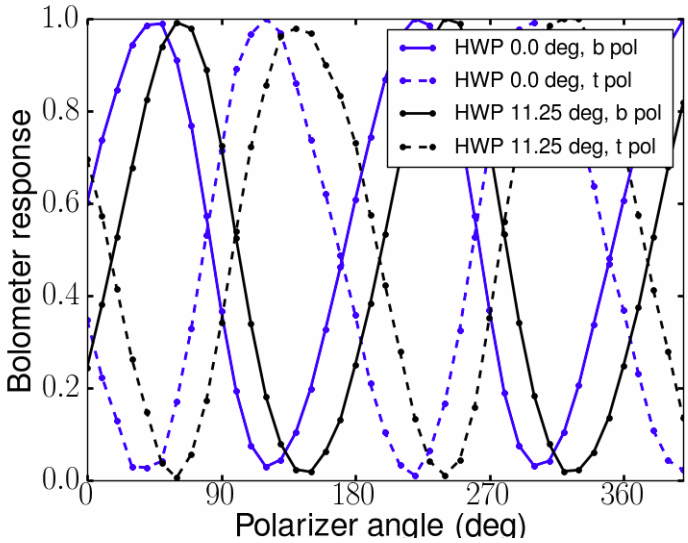

Figure 7.10: Measurement of the polarization sensitivity of two bolometers from the same pixel in the POLARBEAR receiver, at two positions of the HWP. Here the polarization purity is limited by the band-averaged efficiency with which the HWP transforms the polarization. "b pol" and "t pol" refer to the polarization received by the antenna that is transmitted through the bottom and top of the microstrip cross-under, respectively.

Measurements of the polarized source Tau A (a supernova remnant, also known as the Crab Nebula) also provided a check of the polarization sensitivity of the instrument. Measurements of Tau A were made with the HWP at several different positions. The data from two positions of the HWP are plotted in figure 7.11, analyzed by differencing the two detectors from each pixel (individually normalized by their response to atmospheric anisotropies) and calculating the theoretical effect of the HWP to map the measured polarization to polarization on the sky. That they show similar polarization structure on the sky for different HWP positions is another confirmation of the HWP as a polarization modulator. These data can be compared directly with previous measurements of Tau A at 90 GHz [74], which show a similar level and direction of polarization. A more detailed analysis of this data to recover degree-level precision on the measured polarization angle, and to understand all of the systematic uncertainties in the HWP, is underway.

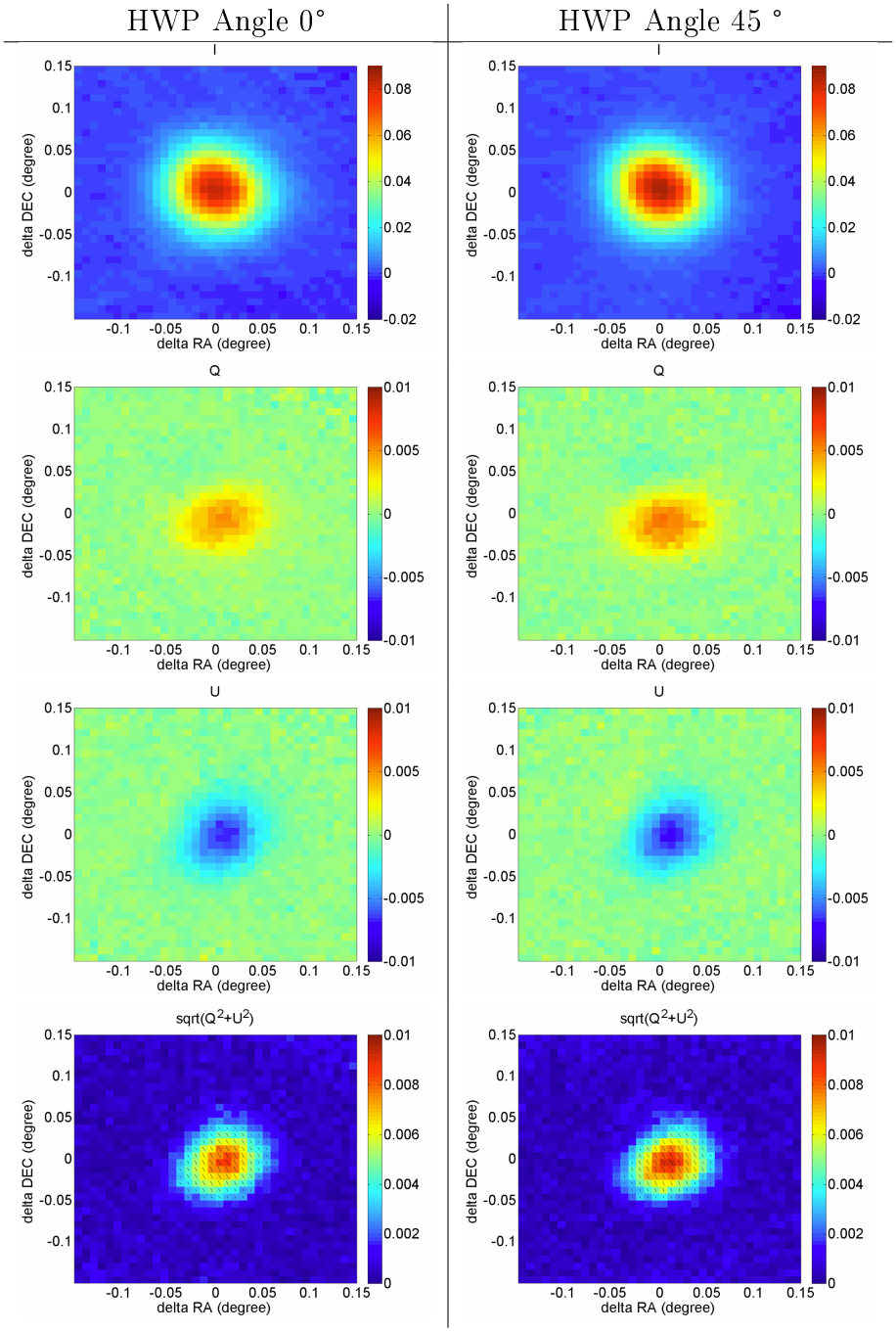

Figure 7.11: POLARBEAR measurements of Tau A (plotted in units of antenna temperature in Kelvin) at two different fixed HWP positions. That they show similar polarization structure on the sky for different HWP positions is confirmation of the HWP as a polarization modulator. These data can be compared directly with previous measurements of Tau A at 90 GHz (figure 2 of [74]).

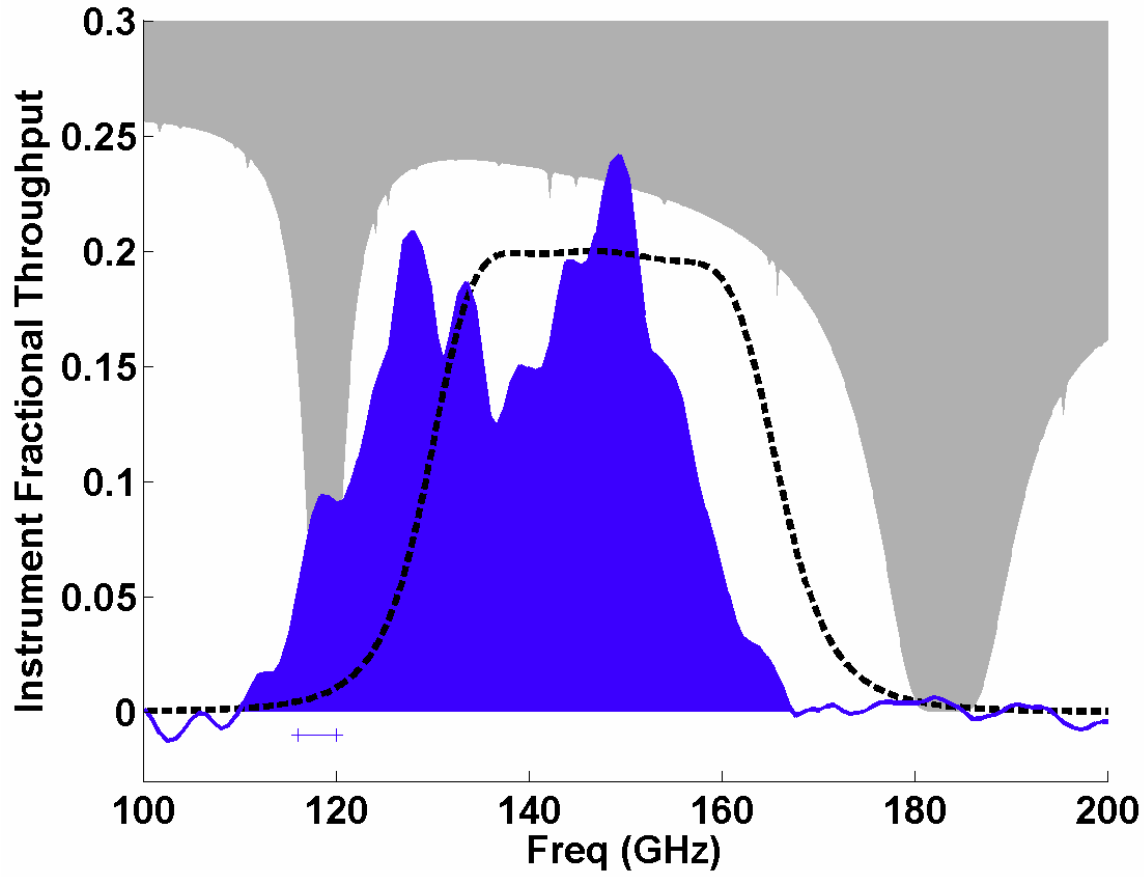

Figure 7.12: Measurement of the spectral response of one of the bolometers, along with the design band and the modeled transmittance of the Cedar Flat atmosphere. The design band is normalized using the instrument model in table 7.1. The measured band is normalized using the average detector response to Jupiter. The line just above the 120 GHz marker shows the resolution at which the data are smoothed.

7.4 Spectral sensitivity

Measurements of the spectral sensitivity of the detectors were made in the observation cryostat using a Fourier Transform Spectrometer (FTS). At the resolution limit of the measurement (1 GHz), the band showed significant structure, some of which would change for a different location of the detector with respect to the FTS. The source of this structure is under investigation. Figure 7.12 shows the spectrum smoothed to a resolution of 5 GHz and normalized using the Jupiter data from Cedar Flat. There are several things to note about this measurement:

- Some of the in-band structure is still obvious despite the smoothing. The cause of this in-band structure is not known. The microstrip filters themselves have been tested separately and were shown, at least in that case, not to have structure of this type [75]. There is mounting evidence that this structure is caused by the coupling of the pixel to the spectrometer, and does not reflect the actual spectrum of the detector. This is currently under investigation.

- The band location is lower than the design band by $\sim 6\%$. This is because variability in the wavespeed of the niobium microstrip causes wafer-to-wafer variability in the bandpass location. This problem is currently being addressed in fabrication by monitoring the wavespeed and adjusting the filter elements as necessary, and by trying to understand the source of the variability.

- In figure 7.12, the band is normalized to the fractional throughput between the bolometer and the primary mirror using the measurements of Jupiter. The design band is normalized using the calculated cumulative fractional throughput from the instrument model shown in table 7.1. That they approximately agree is a success of this instrument model.

Table 7.1 also calculates the level of optical power that the instrument itself is depositing on the bolometers. The optical power from the instrument is discussed more in the following section.

7.5 Optical power from the instrument

The sources of scattering and attenuation in the optical path are detailed in table 7.1. This model was used to produce the design band prediction shown in figure 7.12, and also to predict the power on the detector due to the instrument and the atmosphere. Figure 7.13 shows a histogram of the power from the instrument on the detectors, in terms of its Rayleigh-Jeans temperature (as referred to the sky side of the primary mirror). The optical powers shown in figure 7.13 are calculated based on three measurements: the total power that the detectors received from Jupiter,

the total power that the detectors received when a large liquid nitrogen source was placed in front of the cryostat, and the total electrical power on the detectors when they were receiving to optical power in a test cryostat. The atmospheric attenuation between the cryostat and Jupiter was modeled given the measurements of $\tau_{225,z}$ by the CARMA tipper [72].

Element	Termination temperature	Loss or Reflection	cumulative fractional throughput (element to bolometer)	T_{RJ} referred to primary mirror
Load resistor mismatch	0.5	0.0%	1.00	0.00
Microstrip filter	0.25	8.2%	1.00	0.00
Antenna mismatch	0.25	0.0%	0.92	0.00
Antenna backlobe	0.25	9.0%	0.92	0.00
Lenslet surface reflection	0.25	15.0%	0.84	0.00
Attenuating filter	5	50.0%	0.71	3.99
Collimating lens	7	5.0%	0.36	0.36
Aperture stop truncation	6	13.0%	0.34	0.68
Aperture lens	7	5.0%	0.29	0.30
Metal mesh reflection	7	2.0%	0.28	0.11
Metal mesh absorption	7	2.0%	0.27	0.11
field lens	7	5.0%	0.27	0.27
Metal mesh reflection	7	2.0%	0.25	0.10
Metal mesh loss	20	2.0%	0.25	0.42
4K IR Shader (2)	20	0.0%	0.24	0.00
Half-wave plate reflection	25	2.0%	0.24	0.53
Half-wave plate loss	70	2.0%	0.24	1.60
Metal mesh reflection	50	2.0%	0.23	1.10
Metal mesh loss	90	2.0%	0.23	2.00
Teflon	90	4.0%	0.23	3.91
77K IR Shaders (5)	80	4.9%	0.22	4.07
300K IR Shaders	100	1.0%	0.21	1.00
300K Zote Foam	300	1.0%	0.20	3.03
Secondary scattering	200	0.3%	0.20	0.60
Secondary absorption	300	0.3%	0.20	0.90
Primary scattering	200	0.3%	0.20	0.59
Primary absorption	300	0.3%	0.20	0.89
To atmosphere:			**0.20**	**26.54**
Total cumulative fractional throughput divided by aperture stop fractional throughput:			**0.23**	

Table 7.1: Table of the elements in the POLARBEAR optical path that cause absorption or scattering of the detector beam. Column two lists the percent that each element is absorbing or scattering, and column three lists the temperature of the element, if absorbing, or the temperature to which the beam is scattered. The power reaching the detector can be written in terms of its Rayleigh-Jeans brightness temperature, which is shown in column four. The temperatures here are referred to the sky side of the primary mirror.

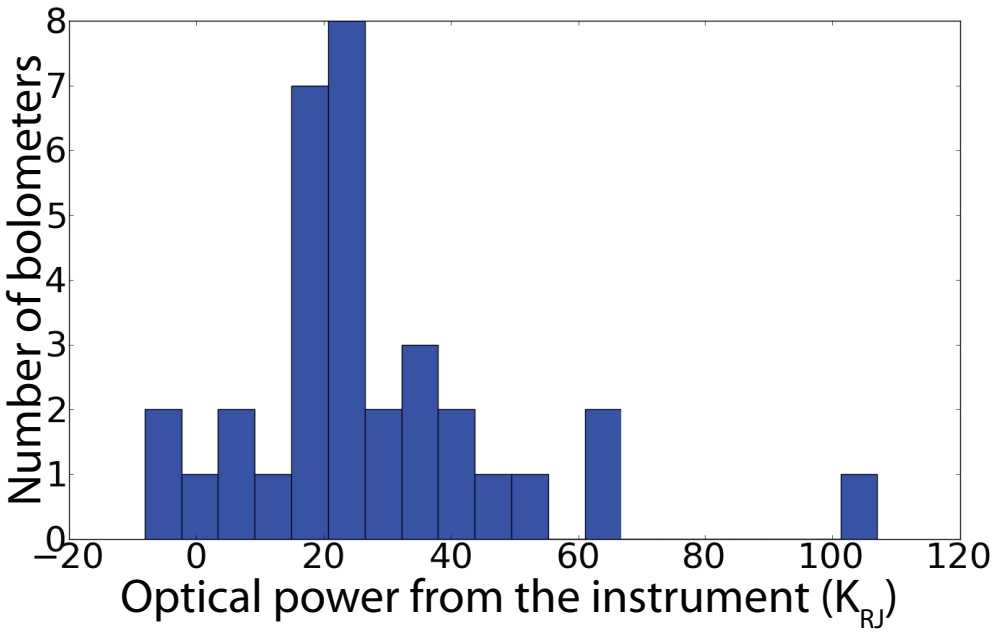

Figure 7.13: Histogram of measured optical power on the bolometers from the POLARBEAR cryostat in terms of its brightness temperature in K_{RJ}. Data are for the pixels with the silicon lenslets. Optical powers were calculated from the response of the bolometers to a beam-filling liquid nitrogen source in front of the cryostat, and the response of the bolometers to Jupiter, modeling the atmospheric transmittance according to the zenith $\tau_{225,z}$ measured by the CARMA tipper at the time [72].

7.6 Noise properties

Table 7.1 shows the expected effective temperature of the cryostat, and the power expected from the atmosphere was calculated from the atmospheric simulations shown with the measured spectral band in figure 7.12. Many of the bolometer properties were measured before deployment, and the expected bolometer noise properties were calculated from those measurements. These expected values for the pixels with silicon lenslet are shown in table 7.2, referred to the sky side of the primary mirror.

The NETs of the bolometers were measured by comparing the response to Jupiter with the white noise of the bolometers. Simulations of atmospheric transmittance were used to reference the NET to the primary mirror rather than above the atmosphere. A histogram of this measurement is shown in figure 7.14.

Noise Source	$\mathrm{NET}_{cmb,bolo}$ $(mK \cdot \sqrt{s})$
Readout	0.31
Bolometer	0.5
Photons	1.0
Total	1.2

Table 7.2: Predicted detector noise at Cedar Flat for a single bolometer.

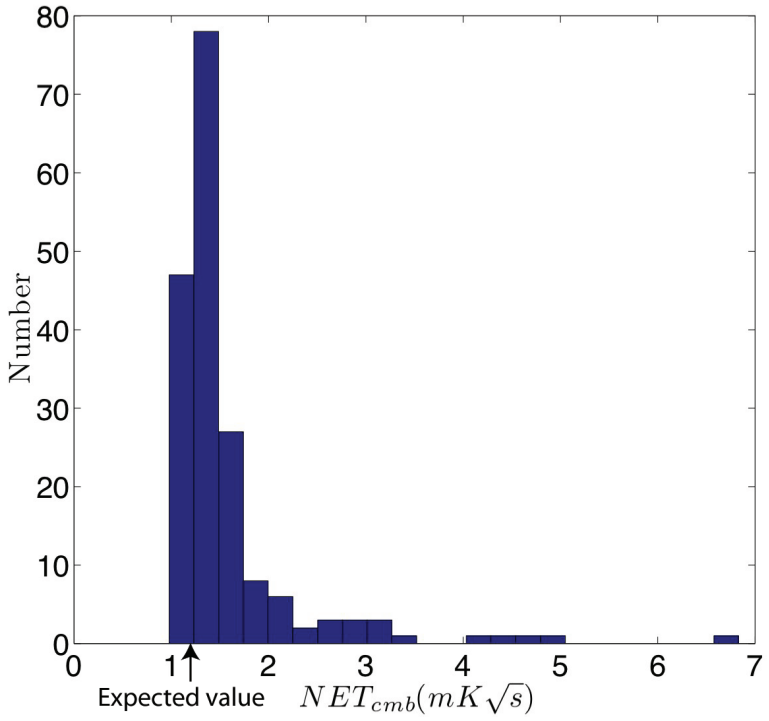

Figure 7.14: Histogram of single-bolometer NET_{cmb} at Cedar Flat for the detectors on two of the sub-arrays.

In Chile, the power from the atmosphere will be lower, and its transmittance higher. New detectors will be fabricated that have the spectral band closer to the design location, so that it is not coincident with the O_2 absorption feature. Given the same bolometer noise properties, these two changes produce the noise predictions shown in table 7.3. This noise is lower than the specifications used to establish the POLARBEAR science goals in figure 1.6. It is higher than the predicted NET_{cmb} from chapter 6 because the optical power from and the attenuation through the instrument are higher than in the model used there.

Noise Source	$\mathrm{NET}_{cmb,bolo}$ $(mK \cdot \sqrt{s})$
Readout	0.15
Bolometer	0.25
Photons	0.39
Total	0.49

Table 7.3: Predicted detector noise at the Chilean site, for a single bolometer. This is slightly lower than the noise used to produce the expected sensitivity plot in chapter 1.

7.7 Addressing concerns from the Cedar Flat engineering deployment

The POLARBEAR cryostat has been returned to the laboratory in Berkeley, in preparation for deployment to begin observations of the CMB in early 2011. Sections 7.7.1 and 7.7.2 discuss some of the concerns that will be addressed before deploying the cryostat to Chile, and section 7.7.3 describes the current work in achieving an observation-quality spectral band.

7.7.1 Optical power from the instrument

Figure 7.13 shows the optical power from the instrument as calculated using the data available from Cedar Flat, and the understanding of the bolometer properties at that time. There was large variation in the results of this calculation, and the variation is likely not due to actual variation in the power on the detectors from the instrument. A more precise understanding of the optical power from the instrument can be gained by cooling down the observation cryostat with the same detectors, but with a completely absorbing element at low temperature directly in front of the detectors. This absorbing element will be thermally controlled between 4–8 K, which will allow a greater understanding of the sensitivity of the detectors themselves, and

of the power that the detectors receive when they are exposed to the instrument during observations. This test is currently underway.

Table 7.1 shows that the effective temperature of the instrument at Cedar Flat was estimated at 26 K_{RJ}, as referred to the sky side of the primary mirror. Note that 4 K_{RJ} of this is from the attenuating filter, so the remaining estimated optical power from the instrument is equivalent to 22 K_{RJ}. The band-averaged sky brightness temperature for median conditions at the Chilean site and an observation angle of 30° from zenith is expected to be 16 K_{RJ}. For many past ground-based CMB experiments, the optical power from the instrument has been the dominant source of optical power on the detectors, and thus the dominant source of photon noise [76, 31]. However, modifying the design of the thermal filtering may allow this to not be the case. If the cryostat is found to contribute greater than 16 K_{RJ} to the optical power on the detectors, the architecture of the thermal filtering will be examined for possible alterations that will decrease this power.

7.7.2 Structure in the spatial response

Figure 7.7**(a-b)** shows that there is some unexplained structure in the spatial response of the detectors with maximum below 1% of the peak response. This is most likely not due to the detectors themselves, because its orientation is more correlated with position on the focal plane rather than detector orientation. Beam structure is not evident in the astrophysical observation shown in figure 7.8, but note that this beammap is on a linear scale and would not have the contrast to show such structure below 1% of the peak response. More measurements of spatial sensitivity, both in an optical test cryostat and through the observation cryostat, will be made to investigate this effect.

7.7.3 Spectral band center frequency

Figure 7.12 shows that the spectral band of the detectors was incorrect for the Cedar Flat deployment, causing an increase in the observed atmospheric opacity. The misplacement of the spectral band was due to variability in the wavespeed of the niobium microstrip. The microstrip filters have been redesigned to mitigate this variability. Figure 7.15 shows the new layout of a POLARBEAR filter that has the same network parameters as the filter in figure 5.2. The important difference is that while the old filter required that the vias (purple) be moved to change the length of the filter elements, this filter design does not. The pattern of the microstrip can be changed by moving the trunk-line to change the stub length, and moving the outer stubs apart to increase the distance between stubs (the length of the inverters). With this layout, two wafers can be fabricated together until after deposition of the microstrip layer. Then one of the wafers can be completed and tested, and the results used to tune the filter on the second wafer. In this way, constant adjustments can

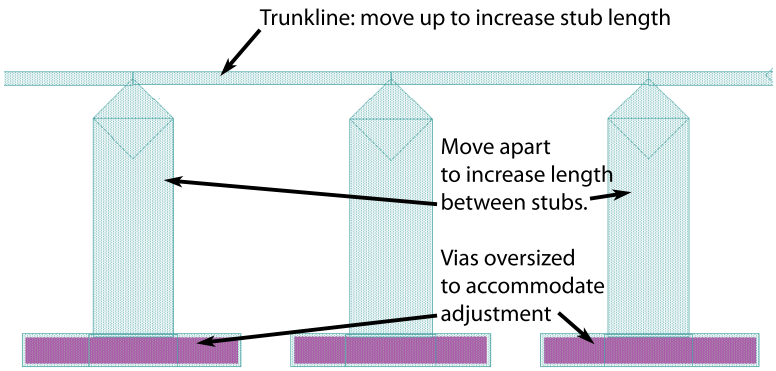

Figure 7.15: Bandpass filter layer to allow center frequency adjustment after deposition of microstrip layer. The center frequency of the filter can be changed by moving the trunk-line to change the stub length and moving the outer stubs to change the distance between stubs (the length of the inverters).

ensure that the band center is never too far away from design, assuming that the microstrip wavespeed is varying slowly with time. This appears to be the case, and recent tests of POLARBEAR detectors have shown a band within the atmospheric window. Fabrication will continue in this way until the seven wafers necessary for the POLARBEAR focal plane are completed.

7.8 Onward to the Chilean deployment

The HTT is currently in transit to the Atacama desert in Northern Chile to be the initial installation of the James Ax Observatory[2]. The focal plane will be upgraded to the full complement of seven sub-arrays, and the experiment will begin CMB observations in 2011. After one year of observation, POLARBEAR will have the integrated sensitivity to measure the predicted B-mode lensing polarization anisotropy and begin the search for inflationary gravitational waves. The POLARBEAR experiment will then expand its frequency coverage over other atmospheric windows to allow a more thorough examination of the data for astrophysical foreground contamination.

[2]The James Ax foundation provided a portion of the funding for the POLARBEAR experiment

Bibliography

[1] S. Dodelson, *Modern Cosmology*. Academic Press, 2003.

[2] J. C. Mather, E. S. Cheng, D. A. Cottingham, R. E. Eplee, Jr., D. J. Fixsen, T. Hewagama, R. B. Isaacman, K. A. Jensen, S. S. Meyer, P. D. Noerdlinger, S. M. Read, L. P. Rosen, R. A. Shafer, E. L. Wright, C. L. Bennett, N. W. Boggess, M. G. Hauser, T. Kelsall, S. H. Moseley, Jr., R. F. Silverberg, G. F. Smoot, R. Weiss, and D. T. Wilkinson, "Measurement of the cosmic microwave background spectrum by the COBE FIRAS instrument," *Astrophyical Journal*, vol. 420, pp. 439–444, Jan. 1994.

[3] X. Fan, C. Carilli, and B. Keating, "Observational constraints on cosmic reionization," *Annual Review of Astronomy and Astrophysics*, vol. 44, no. 1, pp. 415–462, 2006.

[4] D. Baumann and H. V. Peiris, "Cosmological inflation: Theory and observations," *Advanced Science Letters*, vol. 2, pp. 105–120, 2009.

[5] M. R. Nolta, J. Dunkley, R. S. Hill, G. Hinshaw, E. Komatsu, D. Larson, L. Page, D. N. Spergel, C. L. Bennett, B. Gold, N. Jarosik, N. Odegard, J. L. Weiland, E. Wollack, M. Halpern, A. Kogut, M. Limon, S. S. Meyer, G. S. Tucker, and E. L. Wright, "Five-year Wilkinson Microwave Anisotropy Probe observations: Angular power spectra," *The Astrophysical Journal Supplement Series*, vol. 180, no. 2, p. 296, 2009.

[6] S. Prunet, S. K. Sethi, F. R. Bouchet, and M. Miville-Deschenes, "Galactic dust polarized emission at high latitudes and CMB polarization," *Astronomy and Astrophysics*, vol. 339, pp. 187–193, Nov. 1998.

[7] M. Tegmark, D. J. Eisenstein, W. Hu, and A. de Oliveira-Costa, "Foregrounds and forecasts for the cosmic microwave background," *The Astrophysical Journal*, vol. 530, no. 1, p. 133, 2000.

[8] M. Bowden, A. N. Taylor, K. M. Ganga, P. A. R. Ade, J. J. Bock, G. Cahill, J. E. Carlstrom, S. E. Church, W. K. Gear, J. R. Hinderks, W. Hu, B. G. Keating, J. Kovac, A. E. Lange, E. M. Leitch, B. Maffei, O. E. Mallie, S. J. Melhuish,

J. A. Murphy, G. Pisano, L. Piccirillo, C. Pryke, B. A. Rusholme, C. O'Sullivan, and K. Thompson, "Scientific optimization of a ground-based CMB polarization experiment," *Monthly Notices of the Royal Astronomical Society*, vol. 349, pp. 321–335, Mar. 2004.

[9] W. Hu, "CMB temperature and polarization anisotropy fundamentals," *Annals of Physics*, vol. 303, pp. 203–225, Jan. 2003.

[10] B. Reichborn-Kjennerud, A. M. Aboobaker, P. Ade, F. Aubin, C. Baccigalupi, C. Bao, J. Borrill, C. Cantalupo, D. Chapman, J. Didier, M. Dobbs, J. Grain, W. Grainger, S. Hanany, S. Hillbrand, J. Hubmayr, A. Jaffe, B. Johnson, T. Jones, T. Kisner, J. Klein, A. Korotkov, S. Leach, A. Lee, L. Levinson, M. Limon, K. MacDermid, T. Matsumura, X. Meng, A. Miller, M. Milligan, E. Pascale, D. Polsgrove, N. Ponthieu, K. Raach, I. Sagiv, G. Smecher, F. Stivoli, R. Stompor, H. Tran, M. Tristram, G. S. Tucker, Y. Vinokurov, A. Yadav, M. Zaldarriaga, and K. Zilic, "EBEX: a balloon-borne CMB polarization experiment," in *Millimeter, Submillimeter, and Far-Infrared Detectors and Instrumentation for Astronomy V* (W. S. Holland and J. Zmuidzinas, eds.), vol. 7741, p. 77411C, SPIE, 2010.

[11] I. Buder, "Q/U Imaging Experiment (QUIET): A ground-based probe of cosmic microwave background polarization," in *Millimeter, Submillimeter, and Far-Infrared Detectors and Instrumentation for Astronomy V* (W. S. Holland and J. Zmuidzinas, eds.), vol. 7741, p. 77411D, SPIE, 2010.

[12] R. W. Ogburn IV, P. A. R. Ade, R. W. Aikin, M. Amiri, S. J. Benton, J. J. Bock, J. A. Bonetti, J. A. Brevik, B. Burger, C. D. Dowell, L. Duband, J. P. Filippini, S. R. Golwala, M. Halpern, M. Hasselfield, G. Hilton, V. V. Hristov, K. Irwin, J. P. Kaufman, B. G. Keating, J. M. Kovac, C. L. Kuo, A. E. Lange, E. M. Leitch, C. B. Netterfield, H. T. Nguyen, A. Orlando, C. L. Pryke, C. Reintsema, S. Richter, J. E. Ruhl, M. C. Runyan, C. D. Sheehy, Z. K. Staniszewski, S. A. Stokes, R. V. Sudiwala, G. P. Teply, J. E. Tolan, A. D. Turner, P. Wilson, and C. L. Wong, "The BICEP2 CMB polarization experiment," in *Millimeter, Submillimeter, and Far-Infrared Detectors and Instrumentation for Astronomy V* (W. S. Holland and J. Zmuidzinas, eds.), vol. 7741, p. 77411G, SPIE, 2010.

[13] C. D. Sheehy, P. A. R. Ade, R. W. Aikin, M. Amiri, S. Benton, C. Bischoff, J. J. Bock, J. A. Bonetti, J. A. Brevik, B. Burger, C. D. Dowell, L. Duband, J. P. Filippini, S. R. Golwala, M. Halpern, M. Hasselfield, G. Hilton, V. V. Hristov, K. Irwin, J. P. Kaufman, B. G. Keating, J. M. Kovac, C. L. Kuo, A. E. Lange, E. M. Leitch, M. Lueker, C. B. Netterfield, H. T. Nguyen, R. W. O. IV, A. Orlando, C. L. Pryke, C. Reintsema, S. Richter, J. E. Ruhl, M. C. Runyan, Z. Staniszewski, S. Stokes, R. Sudiwala, G. Teply, K. L. Thompson, J. E.

Tolan, A. D. Turner, P. Wilson, and C. L. Wong, "The Keck Array: a pulse tube cooled CMB polarimeter," in *Millimeter, Submillimeter, and Far-Infrared Detectors and Instrumentation for Astronomy V* (W. S. Holland and J. Zmuidzinas, eds.), vol. 7741, p. 77411R, SPIE, 2010.

[14] J. J. McMahon, K. A. Aird, B. A. Benson, L. E. Bleem, J. Britton, J. E. Carlstrom, C. L. Chang, H. S. Cho, T. de Haan, T. M. Crawford, A. T. Crites, A. Datesman, M. A. Dobbs, W. Everett, N. W. Halverson, G. P. Holder, W. L. Holzapfel, D. Hrubes, K. D. Irwin, M. Joy, R. Keisler, T. M. Lanting, A. T. Lee, E. M. Leitch, A. Loehr, M. Lueker, J. Mehl, S. S. Meyer, J. J. Mohr, T. E. Montroy, M. D. Niemack, C. C. Ngeow, V. Novosad, S. Padin, T. Plagge, C. Pryke, C. Reichardt, J. E. Ruhl, K. K. Schaffer, L. Shaw, E. Shirokoff, H. G. Spieler, B. Stadler, A. A. Stark, Z. Staniszewski, K. Vanderlinde, J. D. Vieira, G. Wang, R. Williamson, V. Yefremenko, K. W. Yoon, O. Zhan, and A. Zenteno, "SPTpol: An instrument for CMB polarization," in *American Institute of Physics Conference Proceedings* (B. Young, B. Cabrera, and A. Miller, eds.), vol. 1185, pp. 511–514, AIP, 2009.

[15] M. Zaldarriaga and U. Seljak, "Gravitational lensing effect on cosmic microwave background polarization," *Physics Reviews*, vol. 58, p. 023003, June 1998.

[16] J. M. Kovac, E. M. Leitch, C. Pryke, J. E. Carlstrom, N. W. Halverson, and W. L. Holzapfel, "Detection of polarization in the cosmic microwave background using DASI," *Nature*, vol. 420, pp. 722–787, Dec. 2002.

[17] C. Pryke, P. Ade, J. Bock, M. Bowden, M. L. Brown, G. Cahill, P. G. Castro, S. Church, T. Culverhouse, R. Friedman, K. Ganga, W. K. Gear, S. Gupta, J. Hinderks, J. Kovac, A. E. Lange, E. Leitch, S. J. Melhuish, Y. Memari, J. A. Murphy, A. Orlando, R. Schwarz, C. O. Sullivan, L. Piccirillo, N. Rajguru, B. Rusholme, A. N. Taylor, K. L. Thompson, A. H. Turner, E. Y. S. Wu, M. Zemcov, and null, "Second and third season QUaD cosmic microwave background temperature and polarization power spectra," *The Astrophysical Journal*, vol. 692, no. 2, p. 1247, 2009.

[18] H. C. Chiang, P. A. R. Ade, D. Barkats, J. O. Battle, E. M. Bierman, J. J. Bock, C. D. Dowell, L. Duband, E. F. Hivon, W. L. Holzapfel, V. V. Hristov, W. C. Jones, B. G. Keating, J. M. Kovac, C. L. Kuo, A. E. Lange, E. M. Leitch, P. V. Mason, T. Matsumura, H. T. Nguyen, N. Ponthieu, C. Pryke, S. Richter, G. Rocha, C. Sheehy, Y. D. Takahashi, J. E. Tolan, and K. W. Yoon, "Measurement of cosmic microwave background polarization power spectra from two years of BICEP data," *The Astrophysical Journal*, vol. 711, no. 2, p. 1123, 2010.

[19] D. Larson, J. Dunkley, G. Hinshaw, E. Komatsu, M. R. Nolta, C. L. Bennett, B. Gold, M. Halpern, R. S. Hill, N. Jarosik, A. Kogut, M. Limon, S. S. Meyer, N. Odegard, L. Page, K. M. Smith, D. N. Spergel, G. S. Tucker, J. L. Weiland, E. Wollack, and E. L. Wright, "Seven-year Wilkinson Microwave Anisotropy Probe (WMAP) observations: Power spectra and WMAP-derived parameters," *ArXiv e-prints: 1001.4635*, Jan. 2010.

[20] M. Betoule, E. Pierpaoli, J. Delabrouille, M. Le Jeune, and J. Cardoso, "Measuring the tensor to scalar ratio from CMB b-modes in the presence of foregrounds," *Astronomy and Astrophysics*, vol. 503, pp. 691–706, Sept. 2009.

[21] P. F. Goldsmith, "Radiation patterns of circular apertures with Gaussian illumination," *International Journal of Infrared and Millimeter Waves*, vol. 8, pp. 771–781, 1987. 10.1007/BF01013128.

[22] O. Svelto, *Principles of Lasers, 4th ed.* Plenum Press, 1996.

[23] A. T. Lee, P. Ade, A. Anthony, K. Arnold, D. Boetger, J. Borrill, C. Cantalupo, M. A. Dobbs, J. Errard, N. Halverson, M. Hazumi, W. L. Holzapfel, J. Howard, P. Hyland, A. Jaffe, B. Keating, T. Kisner, Z. Kermish, E. Linder, N. Miller, M. Myers, H. Paar, C. Reichardt, I. Schanning, M. Shimon, H. Spieler, B. Steinbach, R. Stompor, T. Tomaru, H. T. Tran, C. Tucker, E. Quealy, P. L. Richards, and O. Zahn, "Mitigation of systematic errors in the POLARBEAR CMB polarization experiment," in *American Institute of Physics Conference Series*, 2009.

[24] H. Tran, A. Lee, S. Hanany, M. Milligan, and T. Renbarger, "Comparison of the crossed and the Gregorian Mizuguchi-Dragone for wide-field millimeter-wave astronomy," *Applied Optics*, vol. 47, no. 2, pp. 103–109, 2008.

[25] S. Hanany and D. P. Marrone, "Comparison of designs of off-axis Gregorian telescopes for millimeter-wave large focal-plane arrays," *Applied Optics*, vol. 41, no. 22, pp. 4666–4670, 2002.

[26] S. Radford, "Site characterization for mm/submm astronomy (invited speaker)," in *Astronomical Site Evaluation in the Visible and Radio Range* (J. Vernin, Z. Benkhaldoun, and C. Muñoz-Tuñón, eds.), vol. 266 of *Astronomical Society of the Pacific Conference Series*, p. 148, 2002.

[27] M. Shimon, B. Keating, N. Ponthieu, and E. Hivon, "CMB polarization systematics due to beam asymmetry: Impact on inflationary science," *Physics Reviews D*, vol. 77, p. 083003, Apr. 2008.

[28] D. S. Swetz, P. A. R. Ade, C. Allen, M. Amiri, J. W. Appel, E. S. Battistelli, B. Burger, J. A. Chervenak, A. J. Dahlen, S. Das, S. Denny, M. J. Devlin, S. R. Dicker, W. B. Doriese, R. Dünner, T. Essinger-Hileman, R. P. Fisher, J. W.

Fowler, X. Gao, A. Hajian, M. Halpern, P. C. Hargrave, M. Hasselfield, G. C. Hilton, A. D. Hincks, K. D. Irwin, N. Jarosik, M. Kaul, J. Klein, S. Knotek, J. M. Lau, M. Limon, R. H. Lupton, T. A. Marriage, K. L. Martocci, P. Mauskopf, S. H. Moseley, C. B. Netterfield, M. D. Niemack, M. R. Nolta, L. Page, L. P. Parker, B. A. Reid, C. D. Reintsema, A. J. Sederberg, N. Sehgal, J. L. Sievers, D. N. Spergel, S. T. Staggs, O. R. Stryzak, E. R. Switzer, R. J. Thornton, C. Tucker, E. J. Wollack, and Y. Zhao, "Instrument design and characterization of the millimeter bolometer array camera on the atacama cosmology telescope," in *Millimeter and Submillimeter Detectors and Instrumentation for Astronomy IV* (W. D. Duncan, W. S. Holland, S. Withington, and J. Zmuidzinas, eds.), vol. 7020, p. 702008, SPIE, 2008.

[29] M. Tarenghi, "The Atacama Large Millimeter/submillimeter Array: overview & status," *Astrophysics and Space Science*, vol. 313, pp. 1–7, 2008. 10.1007/s10509-007-9602-9.

[30] P. D. Mauskopf, J. J. Bock, H. D. Castillo, W. L. Holzapfel, and A. E. Lange, "Composite infrared bolometers with Si_3N_4 micromesh absorbers," *Applied Optics*, vol. 36, no. 4, pp. 765–771, 1997.

[31] M. C. Runyan, P. A. R. Ade, R. S. Bhatia, J. J. Bock, M. D. Daub, J. H. Goldstein, C. V. Haynes, W. L. Holzapfel, C. L. Kuo, A. E. Lange, J. Leong, M. Lueker, M. Newcomb, J. B. Peterson, C. Reichardt, J. Ruhl, G. Sirbi, E. Torbet, C. Tucker, A. D. Turner, and D. Woolsey, "ACBAR: The Arcminute Cosmology Bolometer Array Receiver," *The Astrophysical Journal Supplement Series*, vol. 149, no. 2, p. 265, 2003.

[32] K. W. Yoon, P. A. R. Ade, D. Barkats, J. O. Battle, E. M. Bierman, J. J. Bock, J. A. Brevik, H. C. Chiang, A. Crites, C. D. Dowell, L. Duband, G. S. Griffin, E. F. Hivon, W. L. Holzapfel, V. V. Hristov, B. G. Keating, J. M. Kovac, C. L. Kuo, A. E. Lange, E. M. Leitch, P. V. Mason, H. T. Nguyen, N. Ponthieu, Y. D. Takahashi, T. Renbarger, L. C. Weintraub, and D. Woolsey, "The Robinson Gravitational Wave Background Telescope (BICEP): A bolometric large angular scale CMB polarimeter," in *Millimeter and Submillimeter Detectors and Instrumentation for Astronomy III* (J. Zmuidzinas, W. S. Holland, S. Withington, and W. D. Duncan, eds.), vol. 6275, p. 62751K, SPIE, 2006.

[33] P. A. R. Ade, G. Pisano, C. Tucker, and S. Weaver, "A review of metal mesh filters," in *Millimeter and Submillimeter Detectors and Instrumentation for Astronomy III* (J. Zmuidzinas, W. S. Holland, S. Withington, and W. D. Duncan, eds.), vol. 6275, p. 62750U, SPIE, 2006.

[34] J. W. Lamb, "Miscellaneous data on materials for millimetre and submillimetre optics," *International Journal of Infrared and Millimeter Waves*, vol. 17, no. 12, pp. 1997–2034, 1996.

[35] E. Hecht, *Optics, 3rd ed.* Addison Wesley, 1998.

[36] H. G. Spieler, M. Dobbs, and E. Bissonnette, "Digital frequency domain multiplexer for mm-wavelength telescopes," *Nuclear Science, IEEE Transactions on*, vol. 55, 2007.

[37] J. M. Gildemeister, *Voltage-Biased Superconducting Bolometers for Infrared and mm-Waves*. PhD thesis, University of California, Berkeley, 2000.

[38] J. C. Mather, "Bolometer noise: Nonequilibrium theory," *Applied Optics*, vol. 21, no. 6, pp. 1125–1129, 1982.

[39] W. H. Press, B. P. Flannery, S. A. Teukolsky, and W. T. Vetterling, *Numerical Recipies: The Art of Scientific Computing*. Cambridge University Press, 1986.

[40] S.-F. Lee, J. M. Gildemeister, W. Holmes, A. T. Lee, and P. L. Richards, "Voltage-biased superconducting transition-edge bolometer with strong electrothermal feedback operated at 370 mK," *Applied Optics*, vol. 37, no. 16, pp. 3391–3397, 1998.

[41] R. K. Pathria, *Statistical Mechanics 2nd Ed.* Oxford: Butterworth-Heinemann, 1996.

[42] P. L. Richards, "Bolometers for infrared and millimeter waves," *Journal of Applied Physics*, vol. 76, no. 1, pp. 1–24, 1994.

[43] W. Holmes, J. M. Gildemeister, P. L. Richards, and V. Kotsubo, "Thermal transport measurements of low stress silicon nitride membranes," *APS Meeting Abstracts*, p. G2601, Mar. 1998.

[44] W. Holmes, J. M. Gildemeister, P. L. Richards, and V. Kotsubo, "Measurements of thermal transport in low stress silicon nitride films," *Applied Physics Letters*, vol. 72, pp. 2250–2252, May 1998.

[45] J. Zmuidzinas, "Thermal noise and correlations in photon detection," *Applied Optics*, vol. 42, no. 25, pp. 4989–5008, 2003.

[46] C. L. Reichardt, P. A. R. Ade, J. J. Bock, J. R. Bond, J. A. Brevik, C. R. Contaldi, M. D. Daub, J. T. Dempsey, J. H. Goldstein, W. L. Holzapfel, C. L. Kuo, A. E. Lange, M. Lueker, M. Newcomb, J. B. Peterson, J. Ruhl, M. C. Runyan, and Z. Staniszewski, "High-resolution CMB power spectrum from the complete ACBAR data set," *The Astrophysical Journal*, vol. 694, no. 2, p. 1200, 2009.

[47] R. S. Elliott, *Antenna Theory and Design: Revised Edition.* John Wiley and Sons, Inc., 2003.

[48] M. J. Griffin, J. J. Bock, and W. K. Gear, "Relative performance of filled and feedhorn-coupled focal-plane architectures," *Applied Optics*, vol. 41, no. 31, pp. 6543–6554, 2002.

[49] J. F. Johansson, "A comparison of some feed types," in *Multi-Feed Systems for Radio Telescopes* (D. T. E. . J. M. Payne, ed.), vol. 75 of *Astronomical Society of the Pacific Conference Series*, p. 82, 1995.

[50] D. F. Filipovic, S. S. Gearhart, and G. M. Rebeiz, "Double-slot antennas on extended hemispherical and elliptical silicon dielectric lenses," *IEEE Trans. Microwave Theory and Techniques*, vol. 41, no. 10, pp. 1738–1749, 1993.

[51] R. C. O'Brient, *A Log-Periodic Focal-Plane Architecture for Cosmic Microwave Background Polarimetry.* PhD thesis, University of California, Berkeley, 2010.

[52] D. B. Rutledge and M. S. Muha, "Imaging antenna arrays," *IEEE Transactions on Antennas and Propagation*, vol. 30, pp. 535–540, July 1982.

[53] J. Zmuidzinas and H. LeDuc, "Quasi-optical slot antenna SIS mixers," *Microwave Theory and Techniques, IEEE Transactions on*, vol. 40, pp. 1797–1804, Sept. 1992.

[54] D. Filipovic, S. Gearhart, and G. Rebeiz, "Double-slot antennas on extended hemispherical and elliptical silicon dielectric lenses," *Microwave Theory and Techniques, IEEE Transactions on*, vol. 41, pp. 1738–1749, oct 1993.

[55] G. Godi, R. Sauleau, and D. Thouroude, "Performance of reduced size substrate lens antennas for millimeter-wave communications," *Antennas and Propagation, IEEE Transactions on*, vol. 53, pp. 1278–1286, April 2005.

[56] R. O'Brient, J. Edwards, K. Arnold, G. Engargiola, W. Holzapfel, A. T. Lee, M. Myers, E. Quealy, G. Rebeiz, P. Richards, H. Spieler, and H. Tran, "Sinuous antennas for cosmic microwave background polarimetry," in *Millimeter and Submillimeter Detectors and Instrumentation for Astronomy IV*, vol. 7020, SPIE, Aug. 2008.

[57] G. Chattopadhyay and J. Zmuidzinas, "A dual-polarized slot antenna for millimeter waves," *Antennas and Propagation, IEEE Transactions on*, vol. 46, no. 5, pp. 736–737, 1998.

[58] G. Chattopadhyay, D. Miller, H. G. LeDuc, and J. Zmuidzinas, "A dual-polarized quasi-optical SIS mixer at 550 GHz," *Microwave Theory and Techniques, IEEE Transactions on*, vol. 48, no. 10, pp. 1680–1686, 2000.

[59] D. P. McGinnis and J. B. Beyer, "A broad-band microwave superconducting thin-film transformer," *Microwave Theory and Techniques, IEEE Transactions on*, vol. 36, no. 11, pp. 1521–1525, 1988.

[60] E. Cristal, "New design equations for a class of microwave filters (correspondence)," *Microwave Theory and Techniques, IEEE Transactions on*, vol. 19, pp. 486 – 490, May 1971.

[61] A. R. Kerr, "Surface impedance of superconductors and normal conductors in EM simulators." MMA Memo 245, 1999.

[62] K. D. Irwin, G. C. Hilton, D. A. Wollman, and J. M. Martinis, "Thermal-response time of superconducting transition-edge microcalorimeters," *Journal of Applied Physics*, vol. 83, no. 8, pp. 3978–3985, 1998.

[63] J. J. Mehl, *Cosmological studies of the Sunzaev-Zel'dovich effect with the APEX-SZ instrument*. PhD thesis, University of California, Berkeley, 2009.

[64] J. Bonetti, P. Day, M. Kenyon, A. Turner, H. LeDuc, C. L. Kuo, and J. Bock, "Electrical and thermal characterization of membrane-isolated, antenna-coupled, TES bolometers for the SPIDER experiment," *Journal of Low Temperature Physics*, vol. 151, no. 1-2, pp. 138–143, 2008.

[65] F. Laermer and A. Schilp, "Method of anisotropically etching silicon," Mar. 1993. US Patent 5501893.

[66] M. Myers, *Antenna-coupled Superconducting Bolometers for Observations of the Cosmic Microwave Background Polarization*. PhD thesis, University of California, Berkeley, 2010.

[67] R. Broom, S. Raider, A. Oosenbrug, R. Drake, and W. Walter, "Niobium oxide-barrier tunnel junction," *Electron Devices, IEEE Transactions on*, vol. 27, pp. 1998–2008, oct. 1980.

[68] B. W. Maxfield and W. L. McLean, "Superconducting penetration depth of niobium," *Physics Reviews*, vol. 139, pp. A1515–A1522, Aug. 1965.

[69] G. Yassin and S. Withington, "Electromagnetic models for superconducting millimetre-wave and sub-millimetre-wave microstrip transmission lines," *Journal of Physics D: Applied Physics*, vol. 28, no. 9, p. 1983, 1995.

[70] S. Paine, "The AM atmospheric model." SMA Technical Memo 152.

[71] *US Standard Atmosphere, 1976*. National Aeronautics and Space Administration, U.S. Government Printing Office, 1976.

[72] Y.-S. Shiao, L. W. Looney, D. P. Woody, R. L. Plambeck, and A. D. Bolatto, "Water vapor in the atmosphere: An examination for CARMA phase correction," in *Millimeter and Submillimeter Detectors and Instrumentation for Astronomy III* (J. Zmuidzinas, W. S. Holland, S. Withington, and W. D. Duncan, eds.), vol. 6275, p. 62750Y, SPIE, 2006.

[73] M. Lueker, B. Benson, C. Chang, H.-M. Cho, M. Dobbs, W. Holzapfel, T. Lanting, A. Lee, J. Mehl, T. Plagge, E. Shirokoff, H. Spieler, and J. Vieira, "Thermal design and characterization of transition-edge sensor (TES) bolometers for frequency-domain multiplexing," *Applied Superconductivity, IEEE Transactions on*, vol. 19, pp. 496–500, June 2009.

[74] J. Aumont, L. Conversi, C. Thum, H. Wiesemeyer, E. Falgarone, F. Piacentini, E. Pointecouteau, N. Ponthieu, J. L. Puget, C. Rosset, J. A. Tauber, and M. Tristram, "Measurement of the Crab nebula polarization at 90 GHz as a calibrator for CMB experiments," *Astronomy and Astrophysics*, vol. 514, p. A70, 2010.

[75] M. J. Myers, K. Arnold, P. Ade, G. Engargiola, W. Holzapfel, A. T. Lee, X. Meng, R. O'Brient, P. L. Richards, H. Spieler, and H. T. Tran, "Antenna-coupled bolometer arrays for measurement of the cosmic microwave background polarization," *Journal of Low Temperature Physics*, vol. 151, pp. 464–470, Apr. 2008.

[76] J. R. Hinderks, P. Ade, J. Bock, M. Bowden, M. L. Brown, G. Cahill, J. E. Carlstrom, P. G. Castro, S. Church, T. Culverhouse, R. Friedman, K. Ganga, W. K. Gear, S. Gupta, J. Harris, V. Haynes, B. G. Keating, J. Kovac, E. Kirby, A. E. Lange, E. Leitch, O. E. Mallie, S. Melhuish, Y. Memari, A. Murphy, A. Orlando, R. Schwarz, C. O. Sullivan, L. Piccirillo, C. Pryke, N. Rajguru, B. Rusholme, A. N. Taylor, K. L. Thompson, C. Tucker, A. H. Turner, E. Y. S. Wu, and M. Zemcov, "QUaD: A high-resolution cosmic microwave background polarimeter," *The Astrophysical Journal*, vol. 692, no. 2, p. 1221, 2009.